**The Dissertation Committee for Yong-Mao Lin Certifies that this is the approved version of the following dissertation:**

# Nanostructured Anode Materials for Li-ion and Na-ion Batteries

**Committee:**

C. Buddie Mullins, Supervisor

Adam Heller, Co-Supervisor

Arumugam Manthiram

Brian A. Korgel

Keith J. Stevenson

# Nanostructured Anode Materials for Li-ion and Na-ion Batteries

**by**

**Yong-Mao Lin, B.S.E.; M.S.**

**Dissertation**

Presented to the Faculty of the Graduate School of

The University of Texas at Austin

in Partial Fulfillment

of the Requirements

for the Degree of

**Doctor of Philosophy**

**The University of Texas at Austin**

**August 2013**

# Dedication

To my family and friends for their love and support

# Acknowledgements

First, I would like to express my gratitude to my parents for raising me up with their endless love, encouragement, and understanding. Without their support, I would have not been able to pursue my doctorate in the U.S., a nation which is on the other side of the earth from my hometown.

I would like to express my sincere appreciation to my supervisor, Professor C. Buddie Mullins, and to my co-supervisor, Professor Adam Heller, for their continuous guidance, support, and encouragement throughout all these years. I learned a great deal from both of them and enjoyed working with them. They taught me not only the technical knowledge of science and engineering, but also how to become a better person. I would also like to express my appreciation to Prof. Arumugam Manthiram, Prof. Brian Korgel, and Prof. Keith Stevenson for their valued time and commitment in serving as my committee members. In addition, Prof. John Goodenough provided valuable comments to my graduate research.

It is my privilege to work with talented individuals in Buddie's group. Dr. Dave Flaherty, whose technical expertise and enthusiasm toward research have always impressed me, provided many help and suggestions for my first project. I would like to thank Dr. Nathan Hahn and Dr. Son Hoang for their assistance in materials synthesis. I thank Paul Abel and Kyle Klavetter for always being friendly, helpful, and informative,

provided many help and creative sparks for my research. I appreciate the friendship with Wen-Yueh Yu, Sean Berglund, Alex Rettie and Hoang Dan, who are always willing to talk and provide help whenever I'm having questions. I also enjoyed working with all of the other past and present members in Buddie's group.

I am also very lucky to have great friends outside of the lab. I would like to thank my best friend, Dr. Wen-Shiue Young, and his wife, Dr. Pei-Yu Liao, for all of their support. I thank Yu-Sheng Su, Hank Huang, Nikki Wen, Dr. Yen-Ting Chen, Dr. Jiun-Yih Chen, Dr. Cheng-Chun Peng, Dr. Kai-Wei Wang, Dr. Sharon Soong, Dr. Yi-Chun Yang for their friendship. I also like to thank all of the members of Austin Taiwanese Presbyterian Church, especially Pastor Ming-Yuan Hsu, Pastor Fred Lee, Chloe Yeh, and Yi-Chen Lai, for their caring support and prayers.

I want to express my deepest appreciation to my wife, Ying-Chieh Weng, for her caring, understanding, thoughtfulness and love throughout the time of my graduate study. To my lovely daughter, Alicia, thank you for enriching my life. I want to thank my little brother, Yung-Sheng Lin, who never fails to cheer me up whenever I am down. I reserve my gratitude for my parents-in-law for caring and thinking about me and my family all the time.

# Nanostructured Materials for Li-ion and Na-ion Battery Anodes

Yong-Mao Lin, Ph.D.

The University of Texas at Austin, 2013

Supervisor: Charles Buddie Mullins

Co-Supervisor: Adam Heller

The demand for electrical energy storage has increased tremendously in recent years, especially in the applications of portable electronic devices, transportation and renewable energy. The performances of lithium-ion and sodium-ion batteries depend on their electrode materials. In commercial Li-ion batteries with graphite anodes the intercalation potential of lithium in graphite is close to the reversible $Li/Li^+$ half-cell potential. The proximity of the potentials can result in unintended electroplating of metallic instead of intercalation of lithium in the graphite anode and frequently leads to internal shorting and overheating, which constitute unacceptable hazards, especially when the batteries are large, as they are in cars and airplanes. Moreover, graphite cannot be readily used as the anode material of Na-ion batteries, because electroplating of metallic sodium on graphite is kinetically favored over sodium intercalation in graphite. This dissertation examines safer Li-ion and Na-ion battery anode materials.

# Table of Contents

# List of Tables

# List of Figures

# List of Illustrations

# Chapter 1: Introduction

## INTRODUCTION TO LITHIUM-ION BATTERIES

Electrical energy storage is of growing importance for both stationary and mobile applications. Batteries constitute energy storage devices, interconverting electrical and chemical potential energies. Two types of batteries are in use: Primary batteries, designed to be used once and disposed; and rechargeable batteries, which can be recharged because their chemical and electrochemical reactions are reversible. The latter include lead-acid (Pb-acid), nickel cadmium (Ni-Cd), nickel metal hydride (Ni-MH), and lithium ion batteries. Among these systems, rechargeable lithium-ion batteries have been studied intensively during the recent decades, because lithium has the most negative reduction potential (-3.04 V vs. standard hydrogen electrode, SHE) and the lowest density (0.53 g $cm^{-3}$) of all metals.[1] It is believed that interest in ambient temperature lithium batteries followed the 1958 thesis of W. S. Harris.[2] It was then discovered that some organic solvents could be used as the electrolyte which did not rapidly react with lithium at room temperature.[2, 3] In the 1970's, intercalation compounds, reversibly incorporating lithium atoms in their lattices were introduced. Much of the early work focused on lithium intercalating cathodes and metallic Li anodes. Although several cathode materials (e.g., $MnO_2$, $MoS_2$, $TiS_2$, and $V_2O_5$) were identified,[4-6] batteries comprised of these cathodes and with a lithium anode did not commercialize due to safety problems. This is because upon recharging, dendrites were frequently formed on the metallic lithium anode when

lithium is electroplated, which causes the internal shorting of the cell and leads to explosive hazards. Consequently, the studies shifted to the so-called Li-ion batteries, which did not have metallic lithium anodes. Current commercial Li-ion batteries use a lithium metal oxide, e.g. $LiCoO_2$ or $LiFePO_4$,[7, 8] as their cathode material and graphite as the lithium host anode material, as shown in Illustration 1.1.

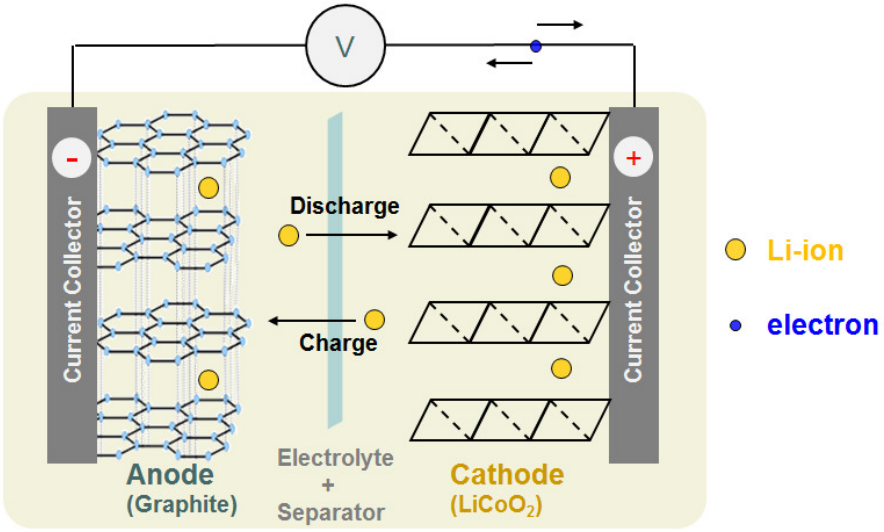


Illustration 1.1. Schematic illustration of a commercial Li-ion battery containing a $LiCoO_2$ cathode and a graphite anode.

The chemical reactions of a lithium-ion battery, with a $LiCoO_2$ cathode and a graphite anode, are as shown below:

$$\text{Cathode: } LiCoO_2 \underset{\text{Discharge}}{\overset{\text{Charge}}{\rightleftharpoons}} Li_{1-x}CoO_2 + x\,Li^+ + x\,e^- \qquad (1.1)$$

$$\text{Anode:}\quad C + x\,Li^+ + x\,e^- \underset{\text{Discharge}}{\overset{\text{Charge}}{\rightleftharpoons}} CLi_x \qquad (1.2)$$

$$\text{Overall reaction:}\quad LiCoO_2 + C \underset{\text{Discharge}}{\overset{\text{Charge}}{\rightleftharpoons}} Li_{1-x}CoO_2 + CLi_x \qquad (1.3)$$

Upon charging, lithium ions are extracted from the $LiCoO_2$ cathode (Reaction (1.1)), and intercalated into the graphite anode (Reaction (1.2)). During discharging, lithium ions de-intercalate from the graphite anode and return to the cathode; while electrons travel through the resistive external circuit, doing work, before returning to the cathode (Illustration 1.1).

Illustration 1.2 shows a schematic energy diagram of a lithium-ion cell at open circuit.[9] In a Li-ion battery, the electrical energy is stored via the chemical potential difference for lithium between the cathode ($\mu_c$) and the anode ($\mu_a$). $E_g$ represents the energy gap or energy separation of the lowest unoccupied molecular orbital (LUMO) and the highest occupied molecular orbital (HOMO) of the electrolyte. An anode with a $\mu_a$ above the LUMO will reduce the electrolyte. On the cathode side, the electrolyte will be oxidized if $\mu_c$ is lower than the HOMO. In theory, a stable electrochemical system requires that both $\mu_c$ and $\mu_a$ lie in the HOMO-LUMO gap of the electrolyte.

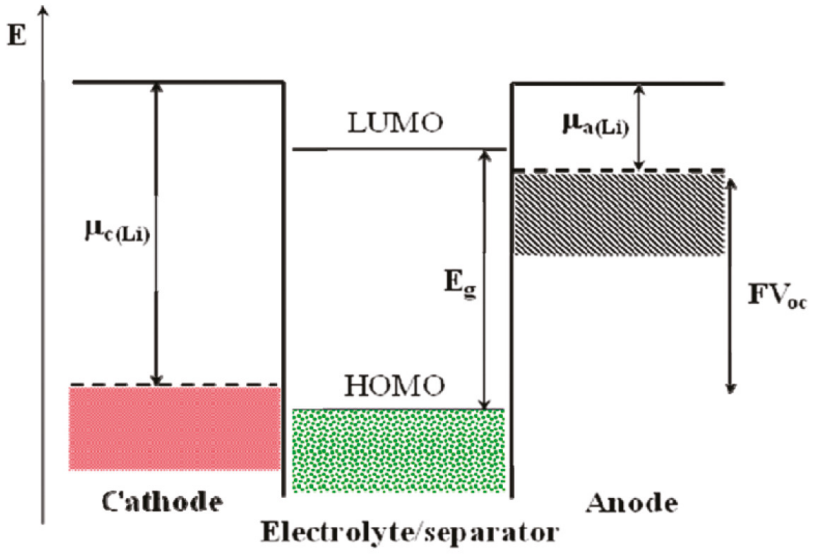


Illustration 1.2. Schematic energy diagram of a lithium-ion cell at open circuit.[9]

Figure 1.1 shows that the stability window of a typical electrolyte for Li-ion batteries ($LiPF_6$ in ethylene carbonate-dimethyl carbonate, EC-DMC) extends from about 0.8 V vs. $Li/Li^+$ up to 4.5 V vs. $Li/Li^+$.[10] The redox process for the $LiCoO_2$ cathode evolves at about 4.0 V vs. $Li/Li^+$, which is located in the electrolyte stability window. However, the redox reaction for the graphite electrode (mesocarbon microbeads, MCMB in this case) takes place at about a couple of hundred mV, outside the stable region of the electrolyte. Because the graphite anode is thermodynamically unstable during lithium intercalation/de-intercalation, electrons will transfer from the graphite anode to the LUMO of the electrolyte, reducing the electrolyte on the graphite surface. In the conventional language of corrosion, lithium intercalated in graphite corrodes by reacting with the electrolytic solution. The initial reduction of the electrolyte leads to the

formation of a solid electrolyte interface (SEI), a passivating film in the language of corrosion, on the surface of graphite, which passivates the surface of the graphite and prevents the electrolyte from further reduction. The energy barrier of lithium ion diffusion through the SEI layer results in an overpotential, which may lead to electroplating of lithium dendrites particularly at a high charge rate. This is because the redox potential of lithium in the graphite anode is only ~0.1 V more oxidizing versus the redox potential of $Li/Li^+$. The formation of lithium dendrites can short the battery and create a thermal runaway hazard and damage, especially for large batteries.[9]

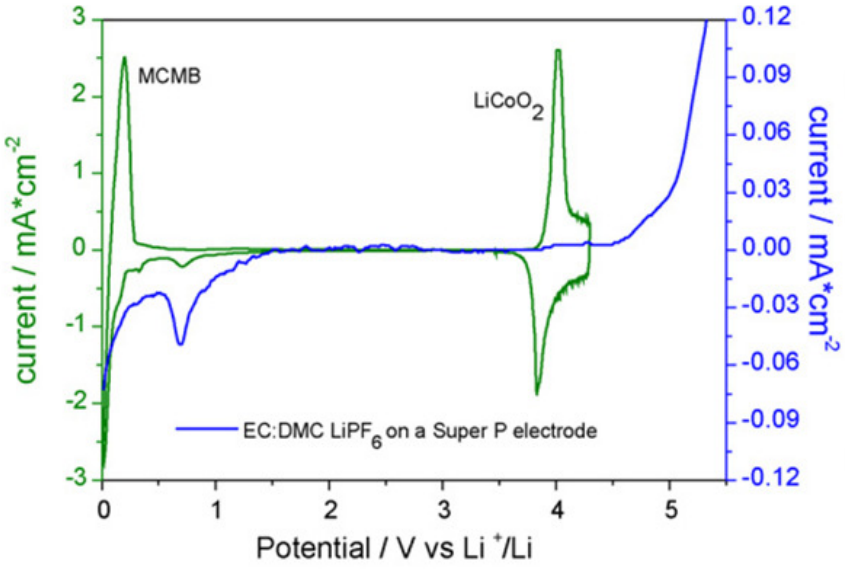


Figure. 1.1. Cyclic voltammetric profiles of lithium ion battery components: $LiCoO_2$ cathode and MCMB graphite anode (green), and electrolyte (blue). Counter electrodes: Super P electrode. Electrolyte: EC:DMC, $LiPF_6$. [10]

Beyond their thermal runaway hazard, graphite anodes are also slower than desired for high rate applications, such as the battery for Plug-in Hybrid Electric Vehicles (PHEVs) and Electric Vehicles (EVs). Because of the slow lithium diffusion in its graphite-containing anodes, the battery pack of current EVs typically needs more than four hours to fully charge. The US Advanced Battery Consortium (USABC) suggests a goal for charging the EV battery from 40% to 80% state of charge (SOC) in 15 minutes. The discharge rate of commercial Li-ion batteries was also found to be limited by the graphite anode. Popov et al. investigated the high rate performance of the commercially available Sony US 18650 (1.4Ah) batteries, with graphite as the anode material.[11] They reported that when the battery operates at a 1C (1.4A) discharge rate, the initial capacity is close to the design value. But initial capacities drop dramatically under high discharge rates, 2C (2.8A) and 3C (4.2A). Also, after 50 cycles, the battery cycling at a 1C discharge rate loses only 5% of its initial capacity while batteries cycling at 2C and 3C lose 38% and 45% of their initial capacity (Figure 1.2). The decrease in capacity of lithium ion batteries at high discharge/charge rates can be attributed to overpotentials associated with three transport processes that are involved: (1) transport of lithium ions in the electrolyte to the electrode materials surface; (2) migration of lithium ions through the surface film; (3) solid state diffusion of lithium ions within the host materials. Considering the relatively fast transport of lithium in liquids, it was suggested that the diffusion of lithium ion in solid host compounds, especially within carbonaceous materials, is the rate-limiting step determining how fast of a battery can be charged and

discharged.[12-14] For these reasons, a safer, lower cost anode material, with sufficiently high capacity, high rate capability and stability is needed.

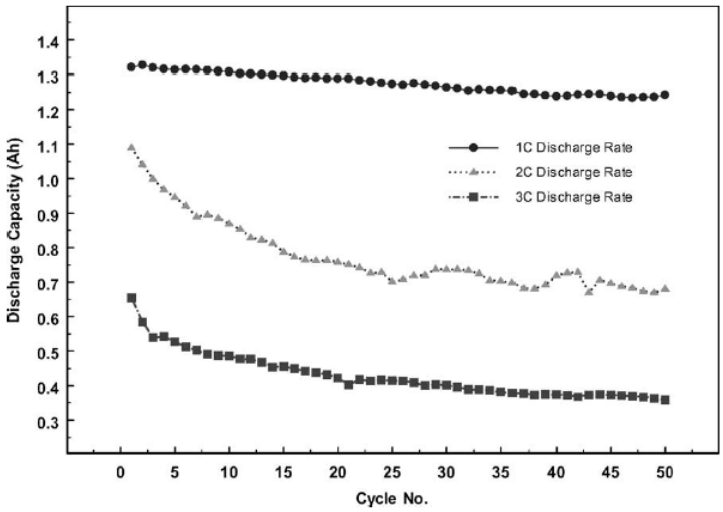


Figure 1.2. Discharge capacity of a Sony US 18650 battery at different discharge rates.[11]

Figure 1.3 shows the choice of active materials for the cathode and the anode.[1] Other than graphite, anode materials considered for Li-ion batteries, included lithium-alloys,[15-23] transition-metal oxides[23-28] and nitrides.[29-32] The more oxidizing half-cell potential of lithium in these materials relative to lithium in graphite, for example in iron oxide with a half cell potential of 1.63 V vs. $Li/Li^+$,[33] assure that no metallic lithium dendrites will grow upon lithium insertion. The inherent safety was achieved at the cost of a lower cell voltage, i.e. lesser potential difference between the cathode and the anode. The lesser cell voltage did not necessarily lead to a lower energy density because many of these candidate materials had a much higher capacity than graphite. For example, one of

the promising alternatives for the conventional graphite anode is silicon because of its high capacity for lithium storage: its maximum theoretical capacity of 3579 mAh $g^{-1}$, corresponding to the formation of a $Li_{15}Si_4$ alloy upon full lithiation at room temperature,[34] is nearly tenfold higher than that of graphite. However, the high capacity of lithium storage is associated with a large volume change that typically results in unacceptable rapid capacity fade within a few cycles.[20] It is well recognized that nanostructured materials not only better accommodate large strains, but also provide short diffusion paths for $Li^+$ insertion/de-insertion.[35, 36] Therefore, in this dissertation, the author investigated nanostructured anode materials for Li-ion batteries.

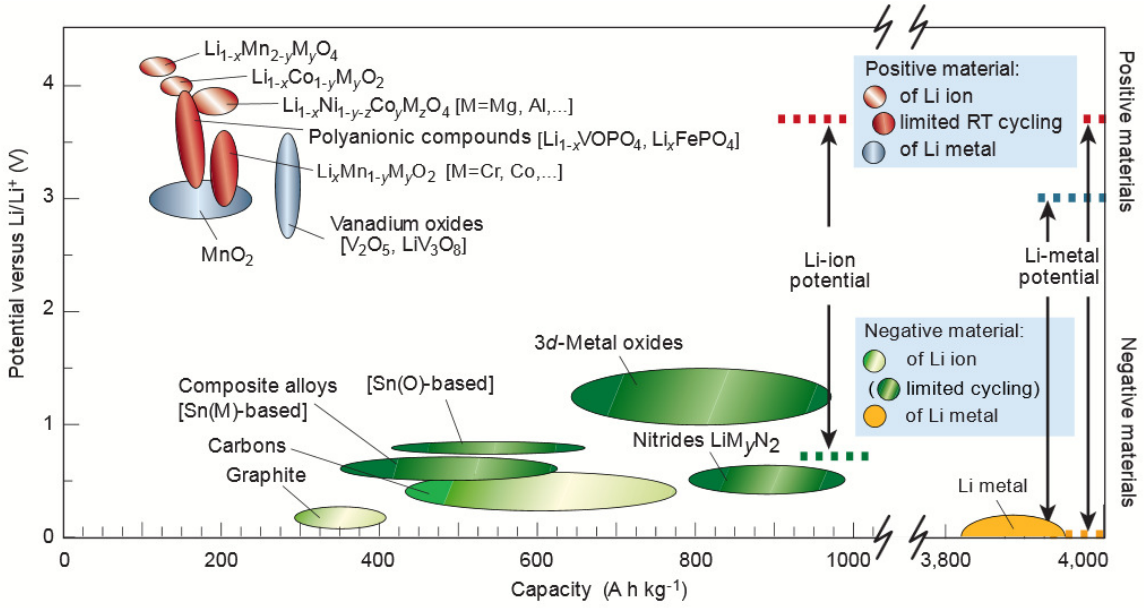


Figure 1.3. Potential versus capacity for electrode materials presently used or under considerations for the next generation Li-ion batteries.[1]

## INTRODUCTION TO SODIUM-ION BATTERIES

Other than Li-ion batteries, sodium-ion batteries are now receiving considerable attention.[37-40] Sodium, is much more abundant than lithium: the sodium concentration is estimated to be 10,320 ppm in seawater and 28,300 ppm in the lithosphere.[41] The concentration of lithium in the upper continental crust is estimated to be only 35 ppm.[42] Consequently, in those applications where the amount of electrode material is large enough to substantially affect the cost, the use of sodium is advantageous. Just like Li-ion batteries, a similar mechanism can be used to store electrical energy in the form of chemical energy in between the cathode and the anode of Na-ion batteries. Recently, Prussian blue and a few other materials have been identified as promising candidates as cathode materials.[37, 43] However, graphite cannot be readily used as the anode material for Na-ion batteries because electroplating of sodium on graphite is kinetically favored over its intercalation in the basal planes of graphite.[44] Several sodium-alloying elements have been found to be of use; these include Sb, Si, Ge, Sn and Pb.[45-47] However, their capacity was not well retained upon sodium insertion/de-insertion because of the large volume change,[48] just as has been earlier observed in Li-alloys. In this dissertation, the author also explored the cyclability of the Sn-based anode for Na-ion batteries, taking advantage of the unique mechanical properties of nanostructured materials.

## DISSERTATION OVERVIEW

This dissertation consists of eight chapters. Chapter one provides general background information about this research. Of the following five chapters, each chapter represents an independent study on the anode of Li-ion batteries which has been published in a peer reviewed archival journal. Chapter 7 includes our most recent results on the anode of a Na-ion battery. Finally, Chapter 8 covers some concluding remarks and recommendations for future studies.

Chapter 2 details the preparation and the electrochemical properties of amorphous $TiO_2$ film electrodes of controllable and reproducible nano-structure and porosity which were grown via evaporation of titanium in an oxygen ambient (i.e., reactive ballistic deposition (RBD)). The cyclability, rate capability and capacity of the electrodes for Li storage depended on their morphology and porosity, which varied with the angle of incidence of the evaporated titanium. When films are deposited via evaporation at a glancing angle of $80^o$ with respect to surface normal, nano-columnar arrays with high internal porosity, high surface area, and optimal pore size and connectivity can be prepared. The optimized films deposited at $80^o$ exhibit a reversible lithium capacity of ~ 285 $mAhg^{-1}$ at a low cycling rate (0.2 C), and maintain a reversible capacity near 200 $mAhg^{-1}$ at rates as high as 5 C. About 70% of the theoretical capacity (235 $mAhg^{-1}$) was retained with indiscernible capacity decay after 100 cycles at 1 C. The total charge stored in the $TiO_2$ RBD films involves both surface capacitive and diffusional processes. The work in this chapter has been previously published in the *Journal of Physical Chemistry*

*C* authored by Y.-M. Lin, P. R. Abel, D. W. Flaherty, J. Wu, K. J. Stevenson, A. Heller and C. B. Mullins.[49]

In Chapter 3, hydrothermally-synthesized single-crystalline hematite ($\alpha$-$Fe_2O_3$) nanorods were investigated as an anode material for Li-ion batteries. Electrodes prepared with this material exhibited initial reversible capacities of 908 mAh $g^{-1}$ at 0.2 C rate and 837 mAh $g^{-1}$ at 0.5 C rate, and these capacities were completely retained after numerous cycles. The $\alpha$-$Fe_2O_3$ nanorods average ~40 nm in diameter and ~400 nm in length providing a short path for lithium-ion diffusion and effective accommodation of the strain generated from volume expansion during the lithiation/de-lithiation process. This chapter has been published in the *Journal of Physical Chemistry Letters* authored by Y.-M. Lin, P. R. Abel, A. Heller and C. B. Mullins.[50]

Chapter 4 describes the electrochemical properties of Li-ion battery anodes made of $SnO_2$ nanoparticles and a $TiO_2$-supported $SnO_2$ nanocomposite formed of equimolar amounts of the Sn and Ti oxides, respectively. By limiting the voltage window of the charge/discharge cycles to the range 50 mV - 1.0 V, both the $SnO_2$-based anode and the $SnO_2$/$TiO_2$-based anode show improved cycling stability. Compared to the $SnO_2$ nanoparticle based anodes, the $TiO_2$-support-$SnO_2$ nanocomposite anodes exhibit better cyclability and higher Coulombic efficiency. During the first lithiation process, $Li^+$ conducting $Li_xTiO_2$ is formed in the $SnO_2$/$TiO_2$ composite, which structurally and mechanically supports the electrode. The anode made of amorphous $TiO_2$-cassiterite $SnO_2$ retained a reversible capacity of ~500 mAh $g^{-1}$ (based on the weight of $SnO_2$) or

~320 mAh $g^{-1}$ (based on the weight of $SnO_2/TiO_2$) at 0.2 C after 100 cycles and at a rate as fast as 5 C retained a stable reversible capacity of ~340 mAh $g^{-1}$ (based on the weight of $SnO_2$) or ~220 mAh $g^{-1}$ (based on the weight of $SnO_2/TiO_2$). This chapter has been published in the *Journal of Materials Chemistry* authored by Y.-M. Lin, R. K. Nagarale, K. C. Klavetter, A. Heller and C. B. Mullins.[51]

In Chapter 5, the effect of electrolyte solvent on the performance of Si-based anode has been investigated. Electrodes composed of silicon nanoparticles (SiNP) were prepared by slurry casting and then electrochemically tested in a fluoroethylene carbonate (FEC)-based electrolyte. The capacity retention after cycling was significantly improved compared to electrodes cycled in a traditional ethylene carbonate (EC)-based electrolyte. The work in this chapter has been published in *Chemical Communications* authored by Y.-M. Lin, K. C. Klavetter, P. R. Abel, N. C. Davy, J. L. Snider, A. Heller and C. B. Mullins.[52]

In Chapter 6, amorphous $GeO_2$ nanoparticles were prepared via a surfactant-assisted hydrothermal process. The effect of the reaction temperature and the surfactant concentration on the morphology of $GeO_2$ particles was investigated. Particles of less than 300 nm were obtained when using 1,2-diaminopropane surfactant in a synthesis carried out at 180°C. The synthesized germanium oxide nanoparticles were evaluated for their utility as the active anode material in Li-ion batteries. The electrode prepared with this material exhibited a stable capacity of ~600 mAh $g^{-1}$ at 0.2 C rate for up to 150 cycles in a conventional electrolyte containing ethylene carbonate (EC). The cyclability of the

$GeO_2$ nanoparticle electrode was further improved by using a fluorinated ethylene carbonate (FEC) based electrolyte, which showed capacities greater than 600 mAh $g^{-1}$ and retained more than 96% of their capacity after 500 cycles at 0.2 C rate. The effect of different electrolyte systems was studied by using electrochemical impedance spectroscopy and electron microscopy. This chapter has been published in the *Journal of Physical Chemistry Letters* authored by Y.-M. Lin, K. C. Klavetter, A. Heller and C. B. Mullins.[53]

Chapter 7 describes our recent results on Sn-based anodes for Na-ion batteries. $Sn_{0.9}Cu_{0.1}$ nanoparticles were synthesized via a surfactant-assisted wet chemistry method, which were then investigated as an anode material for ambient temperature rechargeable sodium ion batteries. The $Sn_{0.9}Cu_{0.1}$ nanoparticle based electrodes exhibited a stable capacity of greater than 420 mAh $g^{-1}$ at 0.2 C rate, retaining 97% of their capacity after 100 cycles of sodium insertion/de-insertion. Their performance is considerably superior to electrodes made with either Sn nanoparticles or Sn microparticles. The work in this chapter has been submitted for publication authored by Y.-M. Lin, P. R. Abel, A. Gupta, J. B. Goodenough, A. Heller, and C. B. Mullins.

Finally, Chapter 8 summarizes our work in the area of Li-ion and Na-ion batteries. In addition, recommendations for future work are included in this chapter.

## REFERENCES


1. Tarascon, J. M.; Armand, M., *Nature* **2001,** *414* (6861), 359-367.

2. van Schalkwijk, W.; Scrosati, B., *Advances in Lithium-Ion Batteries*. Springer: 2002.

3. Auborn, J. J.; French, K. W.; Lieberma.Si; Shah, V. K.; Heller, A., *J. Electrochem. Soc.* **1973,** *120* (12), 1613-1619.

4. Whittingham, M. S., *Science* **1976,** *192* (4244), 1126-1127.

5. Parida, K. M.; Kanungo, S. B.; Sant, B. R., *Electrochim. Acta* **1981,** *26* (3), 435-443.

6. Whittingham, M. S.; Dines, M. B., *J. Electrochem. Soc.* **1977,** *124* (9), 1387-1388.

7. Mizushima, K.; Jones, P. C.; Wiseman, P. J.; Goodenough, J. B., *Mater. Res. Bull.* **1980,** *15* (6), 783-789.

8. Padhi, A. K.; Nanjundaswamy, K. S.; Goodenough, J. B., *J. Electrochem. Soc.* **1997,** *144* (4), 1188-1194.

9. Manthiram, A., *J. Phys. Chem. Lett.* **2011,** *2* (3), 176-184.

10. Scrosati, B.; Garche, J., *J. Power Sources* **2010,** *195* (9), 2419-2430.

11. Ning, G.; Haran, B.; Popov, B. N., *J. Power Sources* **2003,** *117* (1-2), 160-169.

12. Scrosati, B., *J. Electrochem. Soc.* **1992,** *139* (10), 2776-2781.

13. Zaghib, K.; Brochu, F.; Guerfi, A.; Kinoshita, K., *J. Power Sources* **2001,** *103* (1), 140-146.

14. Disma, F.; Aymard, L.; Dupont, L.; Tarascon, J. M., *J. Electrochem. Soc.* **1996,** *143* (12), 3959-3972.

15. Besenhard, J. O.; Yang, J.; Winter, M., *J. Power Sources* **1997,** *68* (1), 87-90.

16. Winter, M.; Besenhard, J. O., *Electrochim. Acta* **1999,** *45* (1-2), 31-50.

17. Wachtler, M.; Besenhard, J. O.; Winter, M., *J. Power Sources* **2001,** *94* (2), 189-193.

18. Yang, J.; Winter, M.; Besenhard, J. O., *Solid State Ionics* **1996,** *90* (1-4), 281-287.

19. Liu, W. R.; Wu, N. L.; Shieh, D. T.; Wu, H. C.; Yang, M. H.; Korepp, C.; Besenhard, J. O.; Winter, M., *J. Electrochem. Soc.* **2007,** *154* (2), A97-A102.

20. Kasavajjula, U.; Wang, C. S.; Appleby, A. J., *J. Power Sources* **2007,** *163* (2), 1003-1039.

21. Obrovac, M. N.; Krause, L. J., *J. Electrochem. Soc.* **2007,** *154* (2), A103-A108.

22. Graetz, J.; Ahn, C. C.; Yazami, R.; Fultz, B., *J. Electrochem. Soc.* **2004,** *151* (5), A698-A702.

23. Tirado, J. L., *Materials Science & Engineering R-Reports* **2003,** *40* (3), 103-136.

24. Poizot, P.; Laruelle, S.; Grugeon, S.; Dupont, L.; Tarascon, J. M., *Nature* **2000,** *407* (6803), 496-499.

25. Grugeon, S.; Laruelle, S.; Herrera-Urbina, R.; Dupont, L.; Poizot, P.; Tarascon, J. M., *J. Electrochem. Soc.* **2001,** *148* (4), A285-A292.

26. Hariharan, S.; Saravanan, K.; Balaya, P., *Electrochemical and Solid State Letters* **2010,** *13* (9), A132-A134.

27. Cabana, J.; Monconduit, L.; Larcher, D.; Palacin, M. R., *Adv. Mater. (Weinheim, Ger.)* **2010,** *22* (35), E170-E192.

28. Prosini, P. P.; Mancini, R.; Petrucci, L.; Contini, V.; Villano, P., *Solid State Ionics* **2001,** *144* (1-2), 185-192.

29. Nishijima, M.; Kagohashi, T.; Takeda, Y.; Imanishi, M.; Yamamoto, O., *J. Power Sources* **1997,** *68* (2), 510-514.

30. Nishijima, M.; Kagohashi, T.; Imanishi, M.; Takeda, Y.; Yamamoto, O.; Kondo, S., *Solid State Ionics* **1996,** *83* (1-2), 107-111.

31. Pereira, N.; Klein, L. C.; Amatucci, G. G., *J. Electrochem. Soc.* **2002,** *149* (3), A262-A271.

32. Takeda, Y.; Nishijima, M.; Yamahata, M.; Takeda, K.; Imanishi, N.; Yamamoto, O., *Solid State Ionics* **2000,** *130* (1-2), 61-69.

33. Li, H.; Balaya, P.; Maier, J., *J. Electrochem. Soc.* **2004,** *151* (11), A1878-A1885.

34. Obrovac, M. N.; Christensen, L., *Electrochemical and Solid State Letters* **2004,** *7* (5), A93-A96.

35. Arico, A. S.; Bruce, P.; Scrosati, B.; Tarascon, J. M.; Van Schalkwijk, W., *Nat. Mater.* **2005,** *4* (5), 366-377.

36. Wang, Y.; Cao, G. Z., *Adv. Mater. (Weinheim, Ger.)* **2008,** *20* (12), 2251-2269.

37. Lu, Y. H.; Wang, L.; Cheng, J. G.; Goodenough, J. B., *Chem. Commun. (Cambridge, U. K.)* **2012,** *48* (52), 6544-6546.

38. Slater, M. D.; Kim, D.; Lee, E.; Johnson, C. S., *Adv. Funct. Mater.* **2013,** *23* (8), 947-958.

39. Kim, S. W.; Seo, D. H.; Ma, X. H.; Ceder, G.; Kang, K., *Adv. Energy Mater.* **2012,** *2* (7), 710-721.

40. Palomares, V.; Serras, P.; Villaluenga, I.; Hueso, K. B.; Carretero-Gonzalez, J.; Rojo, T., *Energy & Environmental Science* **2012,** *5* (3), 5884-5901.

41. Seyfried, W. E.; Janecky, D. R.; Mottl, M. J., *Geochim. Cosmochim. Acta* **1984,** *48* (3), 557-569.

42. Teng, F. Z.; McDonough, W. F.; Rudnick, R. L.; Dalpe, C.; Tomascak, P. B.; Chappell, B. W.; Gao, S., *Geochim. Cosmochim. Acta* **2004,** *68* (20), 4167-4178.

43. Wang, L.; Lu, Y. H.; Liu, J.; Xu, M. W.; Cheng, J. G.; Zhang, D. W.; Goodenough, J. B., *Angew. Chem. Int. Edit.* **2013,** *52* (7), 1964-1967.

44. Stevens, D. A.; Dahn, J. R., *J. Electrochem. Soc.* **2001,** *148* (8), A803-A811.

45. Qian, J. F.; Chen, Y.; Wu, L.; Cao, Y. L.; Ai, X. P.; Yang, H. X., *Chem. Commun. (Cambridge, U. K.)* **2012,** *48* (56), 7070-7072.

46. Darwiche, A.; Marino, C.; Sougrati, M. T.; Fraisse, B.; Stievano, L.; Monconduit, L., *J. Am. Chem. Soc.* **2012,** *134* (51), 20805-20811.

47. Chevrier, V. L.; Ceder, G., *J. Electrochem. Soc.* **2011,** *158* (9), A1011-A1014.

48. Yamamoto, T.; Nohira, T.; Hagiwara, R.; Fukunaga, A.; Sakai, S.; Nitta, K.; Inazawa, S., *J. Power Sources* **2012,** *217*, 479-484.

49. Lin, Y. M.; Abel, P. R.; Flaherty, D. W.; Wu, J.; Stevenson, K. J.; Heller, A.; Mullins, C. B., *J. Phys. Chem. C* **2011,** *115* (5), 2585-2591.

50. Lin, Y. M.; Abel, P. R.; Heller, A.; Mullins, C. B., *J. Phys. Chem. Lett.* **2011,** *2* (22), 2885-2891.

51. Lin, Y. M.; Nagarale, R. K.; Klavetter, K. C.; Heller, A.; Mullins, C. B., *J. Mater. Chem.* **2012,** *22* (22), 11134-11139.

52. Lin, Y. M.; Klavetter, K. C.; Abel, P. R.; Davy, N. C.; Snider, J. L.; Heller, A.; Mullins, C. B., *Chem. Commun. (Cambridge, U. K.)* **2012,** *48* (58), 7268-7270.

53. Lin, Y. M.; Klavetter, K. C.; Heller, A.; Mullins, C. B., *J. Phys. Chem. Lett.* **2013,** *4* (6), 999-1004.

# Chapter 2: Morphology Dependence of the Lithium Storage Capability and Rate Performance of Amorphous $TiO_2$ Electrodes

## INTRODUCTION

Li-ion battery performance depends upon the nanoscale morphology of the cathode and anode electrode materials. Nanostructuring of electrode materials offers enticing new prospects for discovering breakthrough materials and transforming energy conversion and storage concepts.[1, 2] In particular, the use of nano-sized, porous materials of various morphologies (rods, belts, wires) provide more access to both bulk and surface properties;[3, 4] and the kinetics for ion-coupled electron transfer are enhanced due shorter ion diffusion lengths, and to the formation of thinner ion and electron conducting interfacial regions,[5] as well as to increased electrode/electrolyte contact areas. Furthermore, nano-sized and more disordered materials can also more easily accommodate volumetric changes and lattice stresses caused by structural and phase transformations upon lithiation and de-lithiation because these materials deform plastically.[6] While the benefits and detriments of nanoscale morphology on the performance of electrode materials has been well summarized,[7] understanding how changes in materials properties due to nanostructuring has been significantly hindered both by the lack of suitable synthetic techniques for preparing well-defined electrode materials in structure and composition, and by the limited number of appropriate analytical tools for directly characterizing their properties. In this chapter we describe the preparation and characterization of high surface area titanium dioxide electrodes via

evaporative vapor deposition of titanium metal at variable angles in an oxygen ambient, i.e. the reactive ballistic deposition of the metal at glancing angles. This deposition route allows for the systematic control of several material properties including crystallinity, stoichiometry, composition, surface area and porosity. While such a preparation route is impractical for large scale synthesis of pragmatic electrode materials, it is of value for evaluating candidate electrode materials.

In this chapter we specifically study amorphous titania in an effort to understand how surface area and porosity influence lithium ion transfer kinetics relative to more coarse grained and crystalline $TiO_2$ analogues (anatase, rutile, and $TiO_2$(B)).

Lithiated titania, $Li_xTiO_2$, is formed in Reaction (2.1), upon lithium insertion in the initial half-cycle.[8]

$$xLi^+ + TiO_2 + xe^- \rightarrow Li_xTiO_2 \quad (2.1)$$

In subsequent cycles $Li_xTiO_2$ is reversibly lithiated/delithiated at around 1.4 V vs. lithium.[9]

$$Li_xTiO_2 \rightleftarrows Li_{x-y}TiO_2 + yLi^+ + ye^- \quad (2.2)$$

The kinetics of lithium insertion/de-insertion in $Li_xTiO_2$ electrodes has been studied by Cantao et al. using chronopotentiometry who concluded that slow bulk-diffusion of $Li^+$ limits the rate,[10] i.e., it is the size of the $Li_xTiO_2$ particles that determines the rate capability. Lithium insertion in rutile and anatase, the two crystalline phases of $TiO_2$ has

been investigated.[11-18] The insertion of lithium into bulk rutile $TiO_2$ is negligible at room temperature,[19] but anatase $TiO_2$ is lithiated, forming two phases, a lithium poor phase, $Li_{0.01}TiO_2$, and a lithium rich phase, $Li_{0.6}TiO_2$,[20] with the rate of $Li^+$ diffusion at their boundary limiting the rate of its insertion.[21] The five orders of magnitude difference reported for the $Li^+$ diffusion coefficient in anatase-derived $Li_xTiO_2$, ranging from $1\times10^{-18}$ $cm^2\ s^{-1}$ to $1.12\times10^{-13}$ $cm^2s^{-1}$ [8, 22-25] is attributed to the variability of the synthesis parameters and by differences in the micro-/nano-morphology of the materials.[23, 26]

Amorphous $TiO_2$-derived $Li_xTiO_2$ has a higher rate capacity than anatase $TiO_2$ even with similar morphology, implying that $Li^+$ diffuses more rapidly in amorphous $Li_xTiO_2$.[27] The reported diffusion coefficients of $Li^+$ in amorphous $Li_xTiO_2$ range between $1.0\times10^{-14}$ $cm^2s^{-1}$ and $3.5\times10^{-12}$ $cm^2s^{-1}$.[26, 28, 29] Because it is the rate of $Li^+$ diffusion that limits the $Li^+$-insertion process in the lithiated titania, the rate-characteristics of $Li_xTiO_2$ electrodes are highly dependent on its morphology and porosity.[30] In this chapter we describe the synthesis and physical/electrochemical characterization of amorphous titania electrodes with controllable and reproducible morphology and porosity.

Freshly deposited adatoms may diffuse on the surface rapidly, depending upon temperature, a process by which the surface is made conformal and smooth, i.e., the development of a nanoporous and nanostructured film is prevented. For titania films grown by evaporative depostion at or below room temperature surface the diffusion is, however, restrained and structured non-equilibrium surfaces are generated. The process

in which surface-migration of adatoms is avoided is termed "*hit-and-stick*", or ballistic deposition (BD).[31] In BD, vapor phase atoms or molecules travel from their source along straight-line trajectories to the deposition surface, where each is incorporated in close proximity to its original landing site.[31] Initial surface 'roughening' occurs randomly, and subsequent development of the film is highly dependent on the deposition angle. At oblique deposition angles topographically elevated points, created stochastically, preferentially intercept the incoming atoms while shadowing lower regions.[32] This *self-shadowing* growth process can result in the formation of three dimensional high surface area nanocolumnar structures of high internal micro- and meso-porosity. Brett *et al.* have grown highly sculptured films using ballistic deposition at glancing angles to create arrays of micrometer-length nano-columns, -zig-zags, and -helices.[33] This growth technique, sometimes referred to as glancing angle deposition (GLAD), has been the subject of recent reviews by Abelmann and Lodder[32] and by Hawkeye and Brett.[34] Relevant to the present study, Brett and co-workers have used GLAD films of Si to study Li-anode's of high capacity and good capacity retention.[35]

Dohnálek and Kay extended the capabilities of BD by directionally depositing the metal in a reactive ambient ($O_2$, $C_2H_4$, etc.), growing thin films through surface reaction of the metal adatoms with the ambient gas, a process termed reactive ballistic deposition (RBD).[36] Using ballistic deposition or reactive ballistic deposition, highly structured films have been grown from a wide variety of materials including Pd,[37] Cr,[38] Cu,[38] Fe,[39] Ti,[40] $TiO_2$,[41, 42] Mn,[43] MgO,[36] $Ta_2O_5$,[44] $WO_3$,[44] $SiO_x$,[45-47] $MgF_2$,[43] $CaF_2$,[43] TiC,[48-50] $Fe_2O_3$,[51] and

amorphous solid water (ASW).[52-54] The optical, electronic, magnetic, and chemi-physical surface properties often differ from those of their dense, non-structured counterparts. Detailed surface characterization studies have been conducted for porous films of TiC,[48-50] $TiO_2$,[42] Pd,[37] MgO,[36] $SiO_x$[47] and ASW.[52] RBD grown titania films were characterized by Flaherty and co-workers[42] who found that amorphous titania films have the greatest porosity and the highest surface area when deposited at glancing angles (60°-85° vs. normal) on substrates at cryogenic temperatures.

Herein we show that angle dependent reactive ballistic deposition of amorphous nanostructured $TiO_2$ films prepared directly on a Cu current collector, without additional binder and conductive agents, constitute an exceptional model system that allows for the controlled and reproducible deposition and systematic study of the influence of several material properties including morphology, surface area and porosity on energy density and rate capability for dimensionally stable $TiO_2$ anodes utilized in lithium ion batteries.

## EXPERIMENTAL METHODS

*Film Preparation.* The films were grown in a high vacuum apparatus by evaporating titanium metal in a controlled oxygen ambient. After reducing the pressure to below $5\times10^{-8}$ Torr the chamber was backfilled with $O_2$ (99.98%, Matheson) to ~ $1.2\times10^{-6}$ Torr using a leak valve. Quartz crystal microbalance (QCM) measurements and Auger electron microscopy (AES)[42] showed that at this $O_2$ pressure the evaporated titanium was

fully oxidized to $TiO_2$ . The titanium was evaporated from a 0.25 in. diameter rod with an electron-beam evaporator (EMF 3s, Omicron). The substrate holder was rotatable under vacuum using a manipulator. The temperature was monitored with a type K (chromel-alumel) thermocouple spot-welded onto the edge of the substrate holder. For the electrochemical measurements, the films were deposited onto a copper foil current collector. The deposition rate was controlled by the electron beam power and tracked by QCM. Before depositing $TiO_2$, the copper foil sample substrate of 9 μm thickness was cut into 1.5" ×1" rectangular coupons that were spot-welded to a stainless steel sheet which was then attached to the substrate holder by alligator clips. $TiO_2$ films were also grown on a silicon wafer for cross-sectional scanning electron micrographs (SEM).

*Film Characterization.* The morphologies of the $TiO_2$ films were investigated by a field-emission scanning electron microscope (FESEM, LEO-1530, LEO) using a 10 kV acceleration voltage and a scanning transmission electron microscope (STEM, S-5500, Hitachi) using a 30 kV focus voltage. For transmission electron microscopy a JEOL 2010F TEM was used. Selected area electron diffraction (SAED) patterns were obtained at an accelerating voltage of 200 kV. The LEO-1530 and the JEOL 2010F were also used for energy dispersive x-ray spectroscopy (EDX). The crystallinity was determined by X-ray diffraction (XRD, Philips).

*Electrochemical Measurements.* All electrochemical measurements were performed using 2032 type coin cells. The $TiO_2$ film-coated copper foil was punched into

1.1 cm diameter disk electrodes, and pure lithium foil was used as the counter/reference electrode. No binder or conductive carbon was added. The electrolyte was battery grade 1 M $LiPF_6$ (Aldrich) in propylene carbonate (PC, anhydrous, Aldrich) and dimethyl carbonate (DMC, anhydrous, Aldrich) at a 1:1 v/v ratio. A polypropylene membrane (Celgard 2400, Celgard) was used as a separator. The cells were assembled in an argon-filled glove box (Unilab 2000, MBraun) its atmosphere containing less than 5 ppmv $O_2$ or $H_2O$. These assembled coin cells were cycled with a multichannel battery test system (BT 2000, Arbin). Discharge/charge tests were performed in the 1 to 3 V range at constant currents ranging from 0.2 C to 5 C (1 C corresponding to 335 mA/g). Cyclic voltammograms were recorded by an electrochemical workstation (CHI 660D, CH Instruments) between 1 to 3 V at 0.5, 1, 2, and 5 $mV^{-1}$ scan rates. The double layer capacity was measured by cyclic voltammetry in cells with a platinum gauze quasi-reference and counter electrodes in 0.5 M tetrabutylammonium hexafluorophosphate ($TBAPF_6$, Aldrich) in PC/DMC. The $TBAPF_6$ was purified by recrystallization three times from ethyl acetate (Fisher Chemical) and dried in a vacuum oven at 80 ºC for 48 hours.

## RESULTS AND DISCUSSION

### Characterization of the $TiO_2$ Films Grown by Reactive Ballistic Deposition.

Energy dispersive x-ray spectroscopy (EDX) results reveal that the Ti:O ratio of the

RBD-grown films is about 1:2.1. X-ray diffraction (XRD) shows that the $TiO_2$ RBD films, both deposited at normal incidence ($0^o$) and at glancing angles ($60^o$, $70^o$, $80^o$), are amorphous. Selected area electron diffraction (SAED) confirms the amorphous nature of the as-deposited RBD films (Figure 2.1). Cross-sectional SEM views of $TiO_2$ RBD films grown on a silicon wafer are shown in Figure 2.2. The film deposited at normal incidence ($0^o$) is dense and smooth (Figure 2.2(a)), while the films deposited at $60^o$, $70^o$ and $80^o$ vs. normal are increasingly nanoporous (Figure 2.2(b)-(d)), consistent with the results of Flaherty et al.[42]

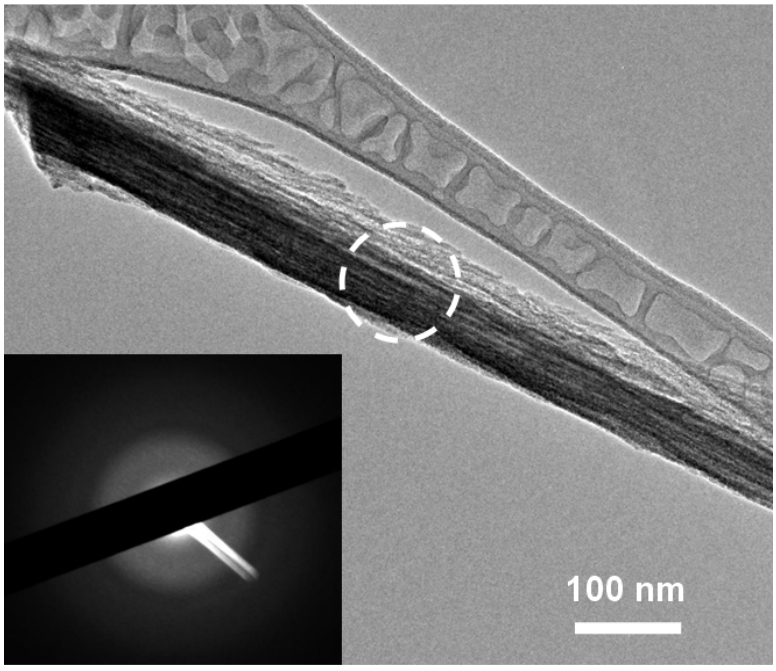


Figure 2.1. Transmission electron microscopic image and selected area electron diffraction (SAED) of a single column $TiO_2$ deposited at $80^o$ incidence angle (white dashed circle: selected area for SAED).

Figure 2.2(a) shows that the dense film, deposited at normal (0°) incidence, is ~220 nm thick. Assuming that the density of this film is 3.84 g/cm$^3$,[55] the calculated mass per unit area is 84.5 μg/cm$^2$,[55] consistent with the 84 μg/cm$^2$ mass measured by quartz crystal microbalance (QCM) measurements, at a resolution of less than 1 ng/cm$^2$. The films of Figs. 2.2(a)-(d) have an identical 84 μg/cm$^2$ mass per unit area measured by QCM. The measured density (84 μg/cm$^2$, 220 nm thickness) is approximately 98% of the density of anatase $TiO_2$ (3.84 g/cm$^3$). The respective calculated pore volume fractions of the films deposited at 60°, 70° and 80 ° (Figures 2.2(b), (c) and (d)) were 39%, 49%, and 73%, consistent with the expected increase in porosity due to increased ballistic shadowing as the deposition angles increase.

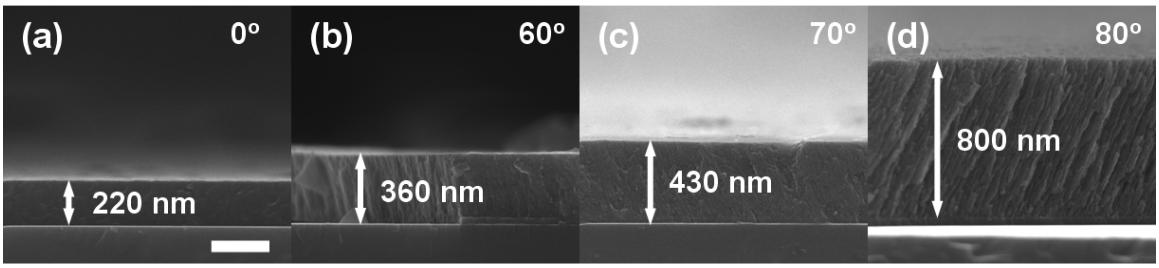


Figure 2.2. Cross-sectional SEM images of $TiO_2$ RBD films on a silicon wafer, deposited at the indicated angels of incidence vs. normal. The 300 nm scale bar applies to all four images.

Films for the electrochemical measurements were deposited onto a copper foil current collector. Top-view SEM images of the normal incidence (0°) film and the

glancing angle (80°) RBD films (Figure 2.3) show that the film deposited at normal incidence (0°) lacks discernable features, while the film deposited at a glancing angle is porous and nanostructured. At higher magnification the film deposited at 80° shows (see Figure 2.4) that the film is composed of an array of feather-like columns. The characteristic diameter of each column is less than 100 nm.

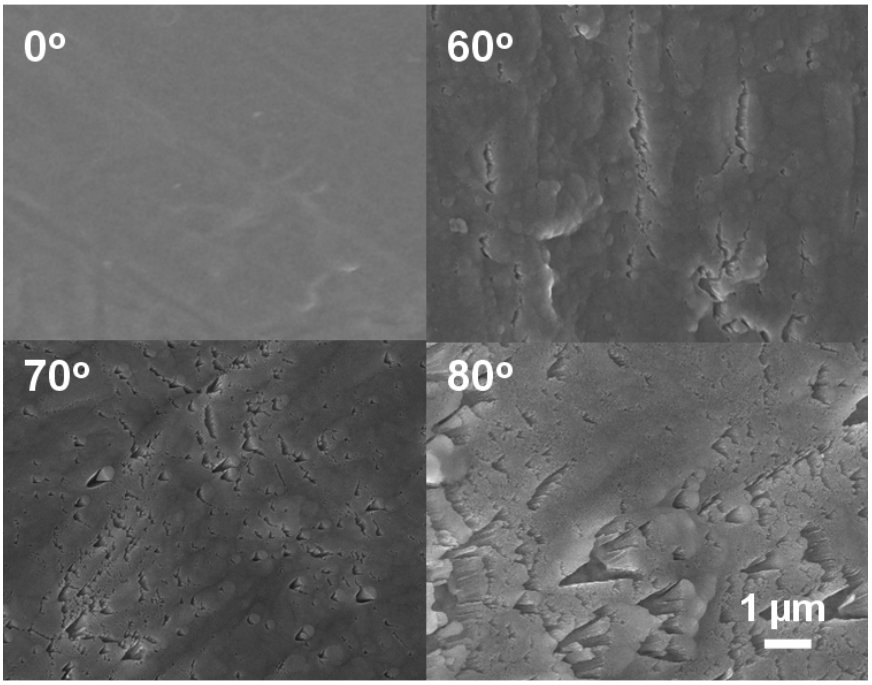


Figure 2.3. Top-view of scanning electron micrographs of $TiO_2$ RBD films on copper foil.

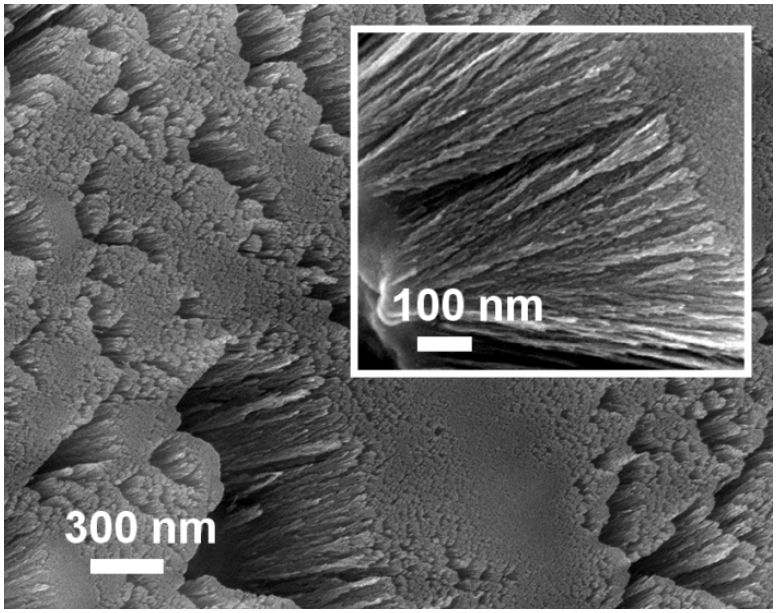


Figure 2.4. Top-view SEM images of $TiO_2$ RBD film deposited at 80° incidence angle on copper foil.

Portions of the $TiO_2$ films were scraped off from the copper substrate, sonicated in ethanol, and drop cast onto lacey carbon-coated copper grids for scanning transmission electron microscopy (STEM). Figure 2.5 shows a bright-field STEM image of a nanocolumn grown at 80° via RBD. Fine nano-structural features, consistent with a very high surface area that should facilitate Li insertion/desertion are evident from the feather-like filaments.

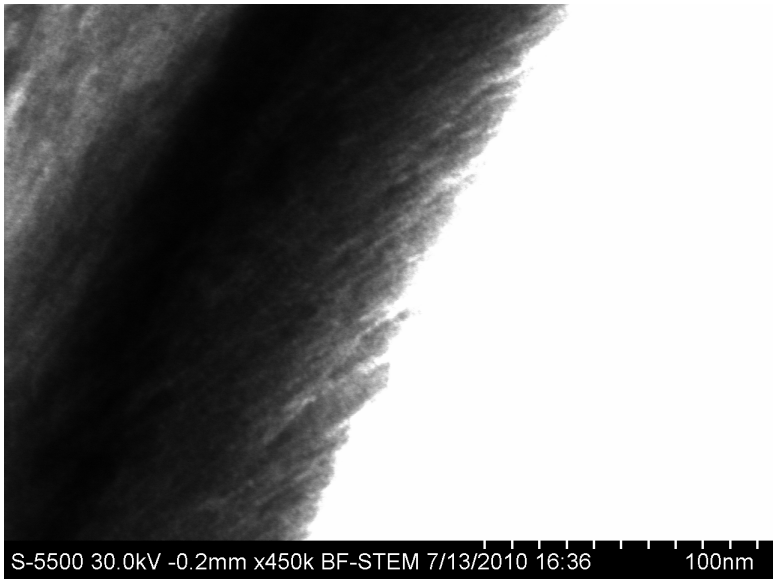


Figure 2.5. STEM image of $TiO_2$ deposited at a glancing incidence angle of 80° on copper foil.

**Electrochemical Tests in Coin Cells.** To evaluate their electrochemical performance, electrodes made with the RBD deposited amorphous titania films on Cu-substrates were incorporated in coin cells, having metallic Li counter/reference electrodes. The cells were initially cycled between 1 V and 3 V versus $Li/Li^+$ at an applied current density of 67 mA/g (0.2 C-rate). Figure 2.6 shows the dependence of the potential on the cycle number for electrodes made with dense titania deposited at 0° and nanoporous $TiO_2$ deposited at 80°.

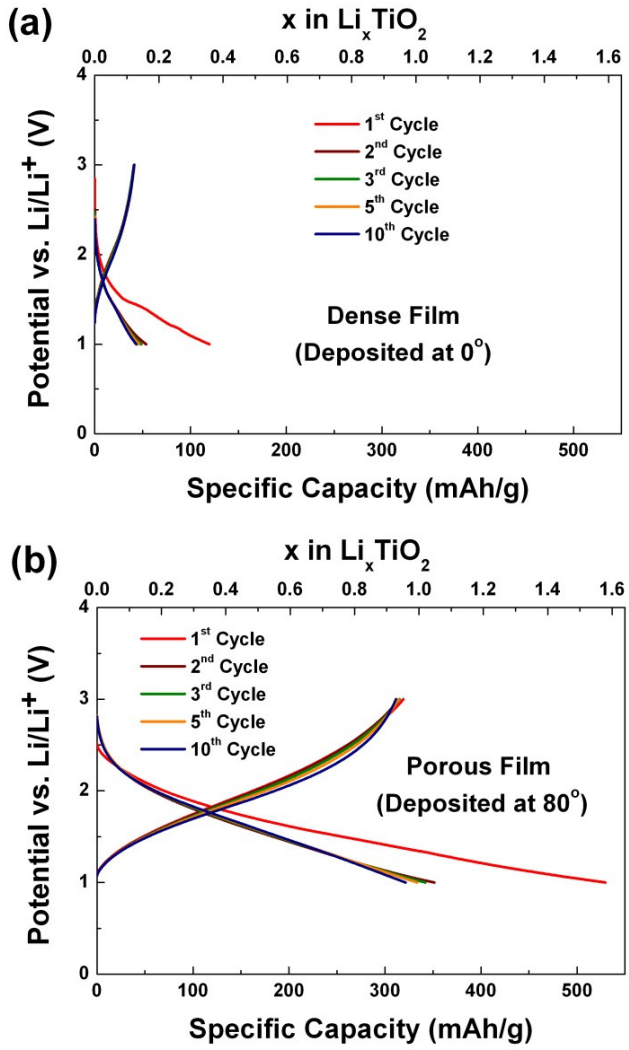


Figure 2.6. Charge/discharge curves of electrodes made with amorphous $TiO_2$ films deposited at 0° (a) and at 80° (b) at a 0.2 C-rate.

With dense crystalline anatase $TiO_2$, a potential plateau associated with the establishment of an equilibrium between lithium-rich and lithium-poor domains appears upon cycling.[15, 20] No such plateau is evident for either the dense 0° or the porous 80° RBD

$TiO_2$ electrodes, indicating the absence of crystalline unlithiated and lithiated phases,[27] the amorphous nature of the films being evident also from their structure-less XRD patterns. During the first cycle, the dense ($0^o$) $TiO_2$ film exhibits an irreversible capacity loss (ICL) of 78 mAh/g, which is associated with Reaction (2.1) and/or the copper oxide on the copper current collector. To test whether the irreversible capacity loss is associated with $TiO_2$ or the copper oxide a cell with an uncoated (i.e., $TiO_2$ free) copper foil was prepared. About 80% of the 78 mAh/g capacity loss is attributable to the reduction of the copper oxide to copper with the additional 20% due to the electrochemically irreversible formation of $Li_xTiO_2$ (Reaction (2.1)) (Figure 2.7).

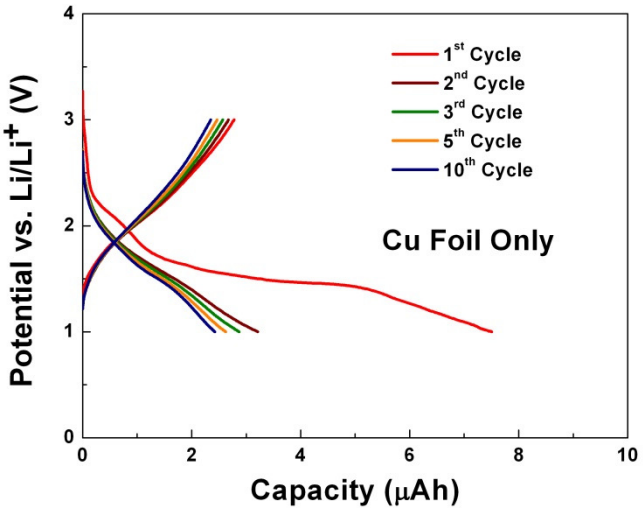


Figure 2.7. Charge/discharge curves of the Cu current collector at 5.7 μA/cm$^2$ (which corresponds to a 0.2 C-rate for $TiO_2$ electrodes).

In the cell comprising the copper foil electrode coated with the porous $TiO_2$ film grown at 80° incidence angle, the ICL associated with reduction of copper oxide accounted for 40% the charge passed in the initial cycle, and 60% is attributed either to the irreversible formation of $Li_xTiO_2$ (Reaction (2.1)) or to reaction with water on the $TiO_2$ films present after exposure to ambient air after their removal from the deposition chamber and incorporation into the coin cells. A rough estimate indicates that the total amount of water adsorbed on $TiO_2$ would be proportional to the surface area, explaining why the porous $TiO_2$ (80°) has a higher ICL than that of the dense $TiO_2$ (0°). A similar result and explanation were provided for amorphous titania nanoparticles.[28]

After the first cycle, the capacity of the dense $Li_xTiO_2$ (0°) electrodes stabilized at a specific capacity of ~ 40 mAh/g (Figure 2.6(a)), but only 10 mAh/g of this capacity resulted from the titania when taking account of the lithiation of the Cu current collector itself (Figure 2.7). The poor energy density (capacity) of lithium in the dense film is attributed to the slow kinetics for lithium diffusion in bulk $Li_xTiO_2$.[10] The reversible capacity of films deposited at 80° was far higher, as high as 315 mAh/g. This high capacity was observed in the second cycle and later cycles (Figure 2.6(b)). About 90%, or 285 mAh/g, is attributed to Reaction (2.2), and only 10% to the reversible lithiation of copper. The approximate stoichiometries for lithium insertion/deinsertion are those of Reaction (2.3):

$$Li_xTiO_2 \rightleftarrows Li_{x-0.85}TiO_2 + 0.85\ Li^+ + 0.85\ e^- \qquad (2.3)$$

Overall, the difference between the 0º dense and the 80º porous and nanostructured films shows that for films of similar mass its is overwhelmingly the nano-morphology that defines the useful coulombic capacity.

The rate capabilities of the electrodes made with films deposited at $0^o$, $60^o$, $70^o$ and $80^o$ were evaluated stepwise from 0.2 C to 5 C (0.2 C, 0.5 C, 1 C, 2 C, 3 C, 5 C) (Figure 2.8), with each electrode cycled at every rate for 10 times. The capacity contributed by the Cu current collector was subtracted from the values shown in Figure 2.8. For the dense film grown at $0^o$, the specific capacity was small, only 10 mAh/g at a 0.2 C-rate, and it decreased to near zero at and above 0.5 C, showing that there was little or no bulk lithiation, i.e. the restriction of the lithiation to the surface of the dense film. As the deposition angle increased from $0^o$ to $60^o$ to $70^o$ and then to $80^o$ the surface area increased along with the coulombic capacity at the increasing rates. At a rate of 5 C, the film deposited at $80^o$ still exhibits a capacity of about 200 mAh/g. The loss of coulombic capacity of the electrodes made with $0^o$, $60^o$, $70^o$, and $80^o$ RBD films was determined, after their use in the tests shown in Figure 2.8, in 100 cycle tests at a 1 C-rate. The results are shown in Figure 2.9. Again, the cyclability improved with the porosity, increasing in the order $0^o < 60^o < 70^o < 80^o$. After 100 cycles at 1 C-rate the most porous ($80^o$) film retained 96.5% of its capacity. The materials deposited at $60^o$ and $70^o$ had lower capacities than those prepared at $80^o$ but their initial capacities did not diminish after 100 cycles at a 1 C-rate (Figure 2.9).

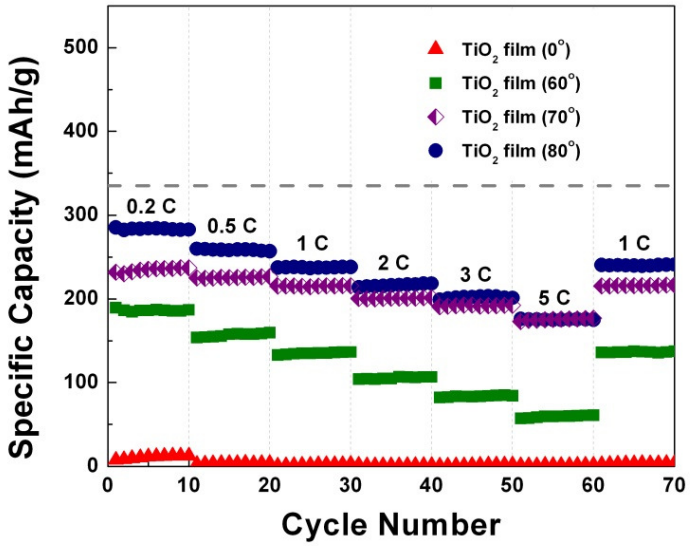


Figure 2.8. Specific capacity of lithium de-insertion in $TiO_2$ RBD films vs. cycle number.

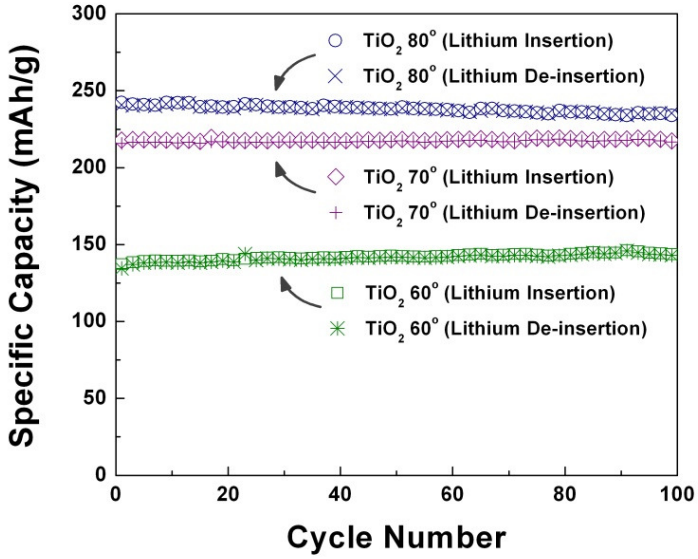


Figure 2.9. Specific capacity vs. cycle number for electrodes made with $TiO_2$ RBD films at a 1 C-rate.

**Capacitive Components of the Measured Coulombic Capacities.** The non-faradaic current of the double layer charging/discharging can contribute to the measured coulombic capacity when the surface area is very large, as it is in the films deposited at high angles. The faradaic contributions also have two components, one originating in the insertion/de-insertion of $Li^+$ into the film material, usually a diffusion-controlled process,[56] the second originating in surface confined electron transfer at the electrode/electrolyte interface[57] better known as a pseudocapacitive response.[58] Contributions to the charge storage mechanisms from these three processes can be determined by performing a scan rate dependence using cyclic voltammetry. The current scaling obeys a power law[23]

$$i = av^b \tag{2.4}$$

where b is determined by plotting log (i) vs. log (v). For lithium insertion limited by the rate of bulk diffusion b would be 0.5 while for purely capacitive charging/discharging b would be 1.0. In the cyclic voltammograms at 0.5 scan rate shown in Figure 2.10 the cathodic peaks represent lithium insertion in the RBD films at 1.5 ~ 1.7 V vs. $Li/Li^+$ and the anodic peaks represent lithium de-insertion at 1.9 ~ 2.1 V vs. $Li/Li^+$. For determining the double layer capacity by cyclic voltammetry (Figure 2.11) the potential of the Pt gauze quasi-reference electrode of 2.49 V versus $Li/Li^+$ was determined by measuring its formal potential in 2 mM ferrocene/$TBAPF_6$/PC/DMC,[59] showing that the capacitive

stored charge of the double layer is negligible relative to the contribution of faradaic and pseudocapacitive processes.

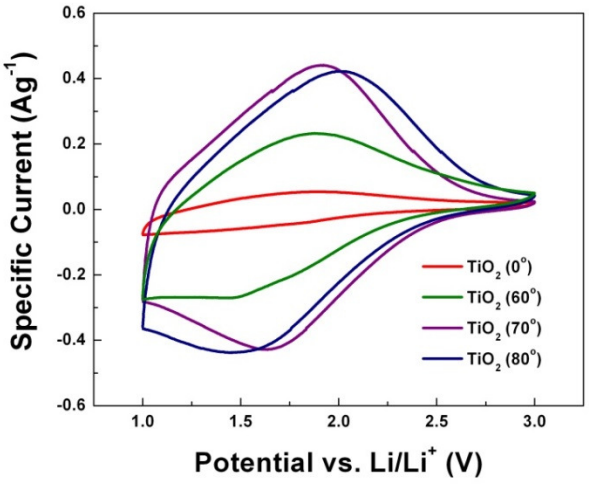


Figure 2.10. Cyclic voltammograms of $TiO_2$ RBD electrodes at a constant scan rate of 0.5 $mVs^{-1}$.

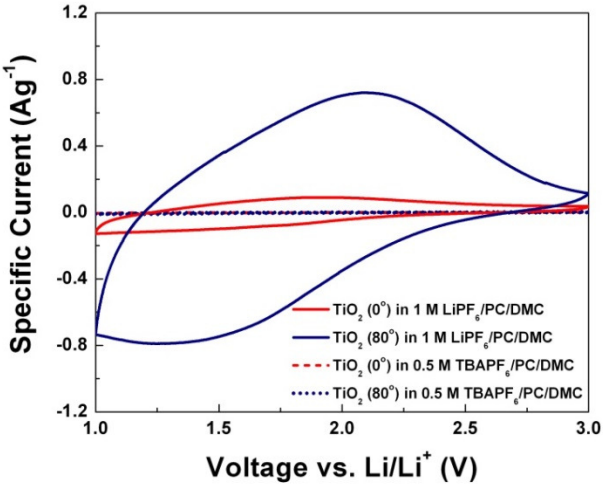


Figure 2.11. Cyclic voltammograms of $TiO_2$ RBD films (deposited at 0° and 80°) scanned at 1 $mVs^{-1}$ in 1 M $LiPF_6$/PC/DMC and 0.5 M $TBAPF_6$/PC/DMC, separately.

The b-value for each film was extracted directly from the log-scale plot of anodic peak current versus scan rate (Figure 2.12). All b-values fall between 0.5 and 1, revealing that both lithium diffusion into the bulk and its surface reaction contribute to the coulombic capacity. Films deposited at 70° had a b-value of 0.84, implying predominantly surface pseudocapacitive contributions to the charge storage mechanism. In a previous study, in which the surface area of $TiO_2$ RBD films was determined by temperature programmed desorption (TPD) of nitrogen, it was found that a 70° film grown at cryogenic temperature had a higher specific area than films deposited at either higher (85°) or lower (48°) angles,[42] explaining the dominance of surface reaction of Li in this particular film. The b-value of the film grown at 80° was 0.63, showing that the charge storage mechanism involves both pseudocapacitive and diffusional processes. The dependence of the voltammetric charge Q on scan rate v as a function of $v^{-1/2}$ was also plotted for $TiO_2$ prepared at various incidence angles from their cyclic voltammograms (Figure 2.13). The linear relationship only holds for dense (0°) film within the full range of scan rate (v = 0.5 to 5 $mVs^{-1}$), which shows the behavior of semi-infinite linear diffusion.[60] Apparently, there is no linear relationship between Q and $v^{-1/2}$ for porous films that deposited at higher incidence angles. Again, which are attributed to the more complicated mechanism includes not only diffusional process but also surface capacitive effect.

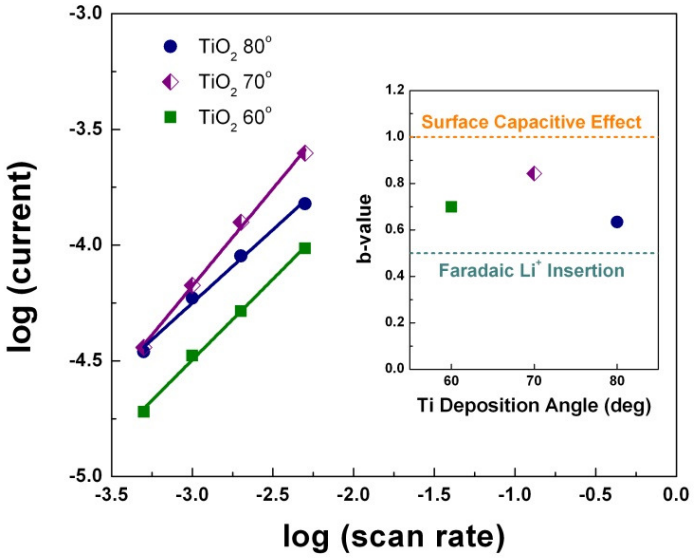


Figure 2.12. Dependence of peak current on sweep rate for $TiO_2$ RBD films.

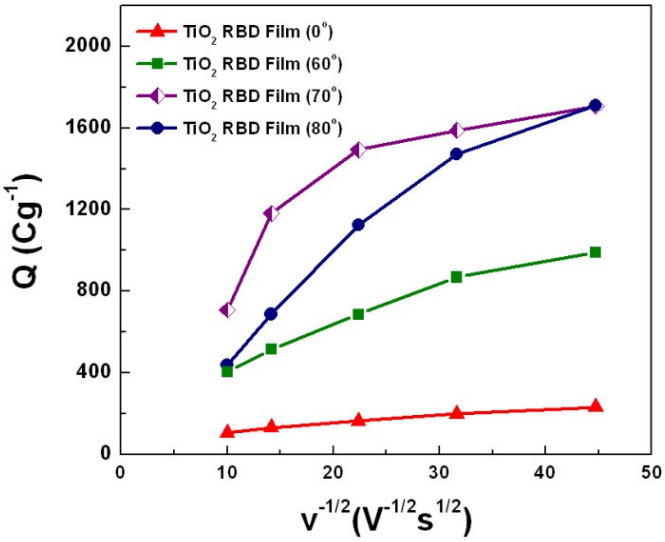


Figure 2.13. Voltammetric charge (Q) at various scan rates (v) of $TiO_2$ RBD Films. Q is Plotted vs. $v^{-1/2}$.

## CONCLUSIONS

Evaporative vapor deposition of titanium at variable angles in an oxygen ambient (i.e. reactive ballistic deposition of Ti) at room temperature allows the preparation of amorphous $TiO_2$ films with controllable and reproducible structural morphology. The films deposited at an incidence angle of 80º by reactive ballistic deposition were the most porous and nanostructured and vastly outperformed dense (0º) bulk films in their charge/discharge rates and reversible capacities for films of equal masses of $TiO_2$. Films deposited at 80º also exhibit a high reversible capacity (285 $mAhg^{-1}$ at 0.2 C), an excellent rate capability (near 200 $mAhg^{-1}$ at 5 C), as well as a good cycling stability. The enhanced electrochemical properties of the RBD electrodes are mainly attributed to their highly porous structure and large surface area.

## REFERENCES


1. Aurbach, D., *J. Power Sources* **2005,** *146* (1-2), 71-78.

2. Sides, C. R.; Li, N. C.; Patrissi, C. J.; Scrosati, B.; Martin, C. R., *Mrs Bulletin* **2002,** *27* (8), 604-607.

3. Kim, S. W.; Han, T. H.; Kim, J.; Gwon, H.; Moon, H. S.; Kang, S. W.; Kim, S. O.; Kang, K., *ACS Nano* **2009,** *3* (5), 1085-1090.

4. Cheng, F. Y.; Chen, J., *J. Mater. Res.* **2006,** *21* (11), 2744-2757.

5. Maier, J., *Nat. Mater.* **2005,** *4* (11), 805-815.

6. Sayle, T. X. T.; Ngoepe, P. E.; Sayle, D. C., *ACS Nano* **2009,** *3* (10), 3308-3314.

7. Scrosati, B.; Garche, J., *J. Power Sources* **2010,** *195* (9), 2419-2430.

8. Fu, Z. W.; Qin, Q. Z., *J. Phys. Chem. B* **2000,** *104* (23), 5505-5510.

9. Wagemaker, M.; Van Der Ven, A.; Morgan, D.; Ceder, G.; Mulder, F. M.; Kearley, G. J., *Chem. Phys.* **2005,** *317* (2-3), 130-136.

10. Cantao, M. P.; Cisneros, J. I.; Torresi, R. M., *J. Phys. Chem.* **1994,** *98* (18), 4865-4869.

11. Hu, Y. S.; Kienle, L.; Guo, Y. G.; Maier, J., *Adv. Mater. (Weinheim, Ger.)* **2006,** *18* (11), 1421-1426.

12. Kubiak, P.; Pfanzelt, M.; Geserick, J.; Hormann, U.; Husing, N.; Kaiser, U.; Wohlfahrt-Mehrens, M., *J. Power Sources* **2009,** *194* (2), 1099-1104.

13. Exnar, I.; Kavan, L.; Huang, S. Y.; Gratzel, M., *J. Power Sources* **1997,** *68* (2), 720-722.

14. Jiang, C. H.; Wei, M. D.; Qi, Z. M.; Kudo, T.; Honma, I.; Zhou, H. S., *J. Power Sources* **2007,** *166* (1), 239-243.

15. Borghols, W. J. H.; Wagemaker, M.; Lafont, U.; Kelder, E. M.; Mulder, F. M., *Chem. Mater.* **2008,** *20* (9), 2949-2955.

16. Chen, J. S.; Lou, X. W., *Electrochem. Commun.* **2009,** *11* (12), 2332-2335.

17. Wagemaker, M.; Borghols, W. J. H.; Mulder, F. M., *J. Am. Chem. Soc.* **2007,** *129* (14), 4323-4327.

18. Wu, M. S.; Wang, M. J.; Jow, J. J.; Yang, W. D.; Hsieh, C. Y.; Tsai, H. M., *J. Power Sources* **2008,** *185* (2), 1420-1424.

19. Koudriachova, M. V.; Harrison, N. M.; de Leeuw, S. W., *Phys. Rev. Lett.* **2001,** *86* (7), 1275-1278.

20. Wagemaker, M.; Kentgens, A. P. M.; Mulder, F. M., *Nature* **2002,** *418* (6896), 397-399.

21. Wagemaker, M.; van de Krol, R.; Kentgens, A. P. M.; van Well, A. A.; Mulder, F. M., *J. Am. Chem. Soc.* **2001,** *123* (46), 11454-11461.

22. Fattakhova, D.; Kavan, L.; Krtil, P., *J. Solid State Electrochem.* **2001,** *5* (3), 196-204.

23. Lindstrom, H.; Sodergren, S.; Solbrand, A.; Rensmo, H.; Hjelm, J.; Hagfeldt, A.; Lindquist, S. E., *J. Phys. Chem. B* **1997,** *101* (39), 7717-7722.

24. Liu, Z. L.; Hong, L.; Guo, B., *J. Power Sources* **2005,** *143* (1-2), 231-235.

25. Lindsay, M. J.; Blackford, M. G.; Attard, D. J.; Luca, V.; Skyllas-Kazacos, M.; Griffith, C. S., *Electrochim. Acta* **2007,** *52* (23), 6401-6411.

26. Furukawa, H.; Hibino, M.; Honma, I., *J. Electrochem. Soc.* **2004,** *151* (4), A527-A531.

27. Fang, H. T.; Liu, M.; Wang, D. W.; Sun, T.; Guan, D. S.; Li, F.; Zhou, J. G.; Sham, T. K.; Cheng, H. M., *Nanotechnology* **2009,** *20* (22), 225701.

28. Borghols, W. J. H.; Lutzenkirchen-Hecht, D.; Haake, U.; Chan, W.; Lafont, U.; Kelder, E. M.; van Eck, E. R. H.; Kentgens, A. P. M.; Mulder, F. M.; Wagemaker, M., *J. Electrochem. Soc.* **2010,** *157* (5), A582-A588.

29. Dziewonski, P. M.; Grzeszczuk, M., *J. Power Sources* **2009,** *190* (2), 545-552.

30. Ortiz, G. F.; Hanzu, I.; Djenizian, T.; Lavela, P.; Tirado, J. L.; Knauth, P., *Chem. Mater.* **2009,** *21* (1), 63-67.

31. Barabási, A.-L.; Stanley, H. E., *Fractal Concepts in Surface Growth*. Cambridge University Press: Cambridge, 1995.

32. Abelmann, L.; Lodder, C., *Thin Solid Films* **1997,** *305*, 1-21.

33. Robbie, K.; Sit, J. C.; Brett, M. J., *J. Vac. Sci. Technol., B* **1998,** *16* (3), 1115-1122.

34. Hawkeye, M. M.; Brett, M. J., *Journal of Vacuum Science & Technology A* **2007,** *25* (5), 1317-1335.

35. Fleischauer, M. D.; Li, J.; Brett, M. J., *J. Electrochem. Soc.* **2009,** *156* (1), A33-A36.

36. Dohnalek, Z.; Kimmel, G. A.; McCready, D. E.; Young, J. S.; Dohnalkova, A.; Smith, R. S.; Kay, B. D., *J. Phys. Chem. B* **2002,** *106* (14), 3526-3529.

37. Kim, J.; Dohnalek, Z.; Kay, B. D., *Surf. Sci.* **2005,** *586* (1-3), 137-145.

38. Robbie, K.; Friedrich, L. J.; Dew, S. K.; Smy, T.; Brett, M. J., *Journal of Vacuum Science & Technology a-Vacuum Surfaces and Films* **1995,** *13* (3), 1032-1035.

39. Liu, F.; Umlor, M. T.; Shen, L.; Weston, J.; Eads, W.; Barnard, J. A.; Mankey, G. J., *J. Appl. Phys.* **1999,** *85* (8), 5486-5488.

40. Sit, J. C.; Vick, D.; Robbie, K.; Brett, M. J., *J. Mater. Res.* **1999,** *14* (4), 1197-1199.

41. Colgan, M. J.; Djurfors, B.; Ivey, D. G.; Brett, M. J., *Thin Solid Films* **2004,** *466* (1-2), 92-96.

42. Flaherty, D. W.; Dohnalek, Z.; Dohnalkova, A.; Arey, B. W.; McCready, D. E.; Ponnusamy, N.; Mullins, C. B.; Kay, B. D., *J. Phys. Chem. C* **2007,** *111* (12), 4765-4773.

43. Robbie, K.; Brett, M. J.; Lakhtakia, A., *Nature* **1996,** *384* (6610), 616-616.

44. Motohiro, T.; Taga, Y., *Appl. Opt.* **1989,** *28* (13), 2466-2482.

45. Messier, R.; Venugopal, V. C.; Sunal, P. D., *Journal of Vacuum Science & Technology A* **2000,** *18* (4), 1538-1545.

46. Seto, M. W.; Robbie, K.; Vick, D.; Brett, M. J.; Kuhn, L., *Journal of Vacuum Science & Technology B* **1999,** *17* (5), 2172-2177.

47. Krause, K. M.; Taschuk, M. T.; Harris, K. D.; Rider, D. A.; Wakefield, N. G.; Sit, J. C.; Buriak, J. M.; Thommes, M.; Brett, M. J., *Langmuir* **2010,** *26* (6), 4368-4376.

48. Flaherty, D. W.; Hahn, N. T.; Ferrer, D.; Engstrom, T. R.; Tanaka, P. L.; Mullins, C. B., *J. Phys. Chem. C* **2009,** *113* (29), 12742-12752.

49. Flaherty, D. W.; May, R. A.; Berglund, S. P.; Stevenson, K. J.; Mullins, C. B., *Chem. Mater.* **2010,** *22* (2), 319-329.

50. May, R. A.; Flaherty, D. W.; Mullins, C. B.; Stevenson, K. J., *The Journal of Physical Chemistry Letters* **2010,** *1* (8), 1264-1268.

51. Hahn, N. T.; Ye, H. C.; Flaherty, D. W.; Bard, A. J.; Mullins, C. B., *ACS Nano* **2010,** *4* (4), 1977-1986.

52. Stevenson, K. P.; Kimmel, G. A.; Dohnalek, Z.; Smith, R. S.; Kay, B. D., *Science* **1999,** *283* (5407), 1505-1507.

53. Kimmel, G. A.; Stevenson, K. P.; Dohnalek, Z.; Smith, R. S.; Kay, B. D., *J. Chem. Phys.* **2001,** *114* (12), 5284-5294.

54. Dohnalek, Z.; Kimmel, G. A.; Ayotte, P.; Smith, R. S.; Kay, B. D., *J. Chem. Phys.* **2003,** *118* (1), 364-372.

55. Bendavid, A.; Martin, P. J.; Takikawa, H., *Thin Solid Films* **2000,** *360* (1-2), 241-249.

56. Wang, J.; Polleux, J.; Lim, J.; Dunn, B., *J. Phys. Chem. C* **2007,** *111*, 14925-14931.

57. Balaya, P.; Bhattacharyya, A. J.; Jamnik, J.; Zhukovskii, Y. F.; Kotomin, E. A.; Maier, J., *J. Power Sources* **2006,** *159* (1), 171-178.

58. Conway, B. E.; Birss, V.; Wojtowicz, J., *J. Power Sources* **1997,** *66* (1-2), 1-14.

59. Lytle, J. C.; Rhodes, C. P.; Long, J. W.; Pettigrew, K. A.; Stroud, R. M.; Rolison, D. R., *J. Mater. Chem.* **2007,** *17* (13), 1292-1299.

60. Ardizzone, S.; Fregonara, G.; Trasatti, S., *Electrochim. Acta* **1990,** *35* (1), 263-267.

# Chapter 3: α-$Fe_2O_3$ Nanorods as Anode Material for Lithium Ion Batteries

## INTRODUCTION

Hematite iron oxide (α-$Fe_2O_3$) has been studied as a water-splitting photoelectrode,[1-3] as a gas sensor,[4] and as the active anode material in lithium ion batteries.[5] In the latter it is potentially superior to the presently used graphite.[5] Because the intercalation potential of lithium in graphite is near the reversible potential of the $Li/Li^+$ half-cell, unintentional electrodeposition of lithium dendrites could short the cell and poses an unacceptable safety hazard in large vehicular power systems.[6, 7] The higher electromotive force (emf) of lithium in iron oxide, 1.63 V vs. $Li/Li^+$,[8] assures that no metallic lithium dendrites will grow. Although this inherent safety is achieved at the cost of a lower cell voltage, the lower cell voltage need not translate to a lesser energy density: with 6 moles of lithium being consumed in the stoichiometric reduction of α-$Fe_2O_3$ to Fe,[9] the theoretical gravimetric and volumetric lithium storage capacities for hematite are 1006 mAh/g and 5331 Ah/L, exceeding the 372 mAh/g and 837 Ah/L capacities of graphite. The capacity of α-$Fe_2O_3$ is, however, not well retained upon cycling. Unlike graphite, which only experiences a ~10% volume change when it is fully lithated,[10] the volume change of α-$Fe_2O_3$ is much larger, approximately 96% during lithium insertion/de-insertion, leading to the disintegration of the anode within a small number of cycles.[11] Reducing the inserted lithium to less than 1 Li atom per α-$Fe_2O_3$

molecule improves the cyclability because of the limited cell volume change, but it also reduces the capacity to one sixth of the theoretical value.[12, 13] In order to approach the high intrinsic theoretical capacity of α-$Fe_2O_3$, it is necessary to design the anode such that it will better accommodate the strain associated with lithium insertion/de-insertion.

It is well recognized that nanostructured materials not only better accommodate large strains, but also provide short diffusion paths for $Li^+$ insertion/de-insertion.[14, 15] Consequently, nanostructured α-$Fe_2O_3$ particle anodes have been engineered from nanoparticles,[16-18] nanosheets,[16] nanodiscs,[19] nanotubes,[4, 20] nanowires,[11] nanocapsules,[21] nanoflakes[22, 23] nanoflowers[24, 25] and nanorods.[26-29] Among these studies, α-$Fe_2O_3$ with a nanorod structure as an anode material for lithium-ion batteries was first reported by Wu et al. in 2006 who also found that the first charge/discharge capacities are highly dependent on the morphology of the hematite nanorods.[26] Although long-term cyclability results were not reported in the study by Wu and coworkers, they demonstrated that α-$Fe_2O_3$ nanorods could be a promising material for lithium storage. Liu and coworkers also synthesized and tested single crystalline α-$Fe_2O_3$ nanorods with diameters in the range of 60-80 nm.[27] They measured an initial reversible capacity as high as 955 mAh $g^{-1}$ with electrodes made of their α-$Fe_2O_3$ nanorods and the capacity retention was also promising; 763 mAh $g^{-1}$ after 30 cycles at 0.1 C rate. Recently, Song and coworkers successfully synthesized α-$Fe_2O_3$ nanorods on titanium foil via a facile hydrothermal method.[28] The hematite nanorod array electrode exhibited good electrochemical performance at

relatively high charge/discharge rate, retained reversible capacities of 562 mAh $g^{-1}$ at 0.2 C and 444 mAh $g^{-1}$ at 0.5 C, respectively, after 50 cycles. Based upon these studies, it is apparent that by introducing nanostructured α-$Fe_2O_3$, the electrochemical behavior of the anode can be significantly improved in terms of cyclability and capacity retention. Moreover, Dahn and coworkers reported the choice of binder can have a major impact on the electrochemical performance of α-$Fe_2O_3$ powder electrode.[30] Better cycling performance was achieved, about 800 mAh $g^{-1}$ for 100 cycles at a 0.2 C rate, by using sodium carboxymethyl cellulose (CMC) binder instead of conventional polyvinylidene fluoride (PVDF) binder on electrodes made of submicron sized α-$Fe_2O_3$.

Here we build upon this important previous research in optimizing the performance of iron oxide anodes and describe a promising negative electrode for lithium ion batteries that is composed of potentially easy to manufacture, narrowly dispersed, single crystalline hematite nanorods. The α-$Fe_2O_3$ nanorod electrode not only exhibited high initial reversible capacities of 908 mAh $g^{-1}$ at a 0.2 C rate and 837 mAh $g^{-1}$ at a 0.5 C rate, respectively, but also fully retained these capacities after numerous cycles.

## EXPERIMENTAL METHODS

*Materials and Synthesis:* α-$Fe_2O_3$ nanorods were prepared by adding iron chloride hexahydrate ($FeCl_3 \cdot 6H_2O$, Alfa Aesar) to deionized water to form a 0.5M ferric chloride solution and then stirred for 15 min. After stirring the 1,2-diaminopropane ($C_3H_{10}N_2$, Alfa

Aesar) was added at a 1:1 volume ratio and stirring was continued for another 15 min. The solution was then transferred to a Teflon-lined stainless steel autoclave and heated to 220 °C for 20 hours. After the mixture cooled to room temperature the precipitate was collected by centrifugation, washed twice with deionized water and dried under vacuum at 80 °C.

*Characterization:* The $\alpha$-$Fe_2O_3$ nanorods were characterized by scanning electron microscopy (SEM) using a Zeiss Supra 40 VP scanning electron microscope; by transmission electron microscopy (TEM) using a JEOL 2010F transmission electron microscope and by X-ray diffraction (XRD) using a Bruker-Nonius D8 Advance powder diffractometer.

*Electrochemical Measurements:* To evaluate the electrochemical performance, the iron oxide electrodes were prepared by mixing the $\alpha$-$Fe_2O_3$ (60 wt %) with conductive carbon black (Super P-Li, Timcal) (20 wt %) and with 90 kDa sodium carboxymethyl cellulose (Aldrich) (20 wt %) using water as the dispersion medium. It has been shown that electrodes made with sodium carboxymethyl cellulose (CMC) perform better than electrodes made with the traditional binder- polyvinylidene fluoride (PVDF).[30, 31] The mixture was slurry-cast on 10 μm thick Cu foil using an automatic applicator and a notch bar with 100 μm clearance, then dried under vacuum at 120 C for 12 hrs. After that, the as-prepared $\alpha$-$Fe_2O_3$ slurry-cast film was punched into disk working electrodes. All electrochemical measurements were carried out using 2032 type coin cells with the as-

prepared working electrode. Cells were assembled in an argon-atmosphere glovebox using lithium foil as the counter/reference electrode and 1M $LiPF_6$ in EC/DMC (1:1 wt/wt) (LP30, EMD Chemicals) as the electrolyte. A polypropylene membrane (Celgard 2400, Celgard) was used as a separator. These assembled coin cells were cycled with a multichannel battery test system (BT 2143, Arbin) between 5 mV and 3 V at a 0.2 C rate (201 mA $g^{-1}$) and at a 0.5 C rate (503 mA $g^{-1}$), corresponding to the rates of fully charging or discharging the cell within 5 hours (for 0.2 C) and 2 hours (for 0.5 C), separately.

## RESULTS AND DISCUSSION

The synthesis method used to produce the α-$Fe_2O_3$ nanorods employed in this study was motivated by the work of Wang and coworkers,[32] who used hydrothermal synthesis with 1,2-diaminopropane as a shape controlling agent. The details of our synthetic procedure, which was slightly different than that employed by Wang et al.,[32] is discussed in the experimental methods section. SEM images (Figure 3.1) show that the average diameter of the prepared α-$Fe_2O_3$ nanorods is ~ 40 nm, with an average length of ~400 nm. Figure 3.1(b) shows an end-view of the α-$Fe_2O_3$ nanorods with hexagonal structure, indicating that each nanorod grew along the [001] direction of rhombohedral hematite.[33] In order to investigate the particle size effect of α-$Fe_2O_3$ on the electrochemical performance, micron sized and submicron sized hematite particles were employed as references for comparison with the nanorods. Micron sized α-$Fe_2O_3$ particles

were prepared by the same hydrothermal synthesis, but without the addition of 1,2-diaminopropane. The submicron-size α-$Fe_2O_3$ particles (product number: 310050, Aldrich) were purchased without any further treatment. Submicron-size α-$Fe_2O_3$ particles were purchased from Aldrich, and had a particle size distribution ranging from 50 nm to approximately 1 μm, with the diameters of typical particles being 100-500 nm (Figure 3.2). The micron-sized α-$Fe_2O_3$ particles synthesized in our laboratory by the same hydrothermal process, but without adding the shape controlling agent 1,2-diaminopropane, ranged in diameter from 1 μm to 6 μm (Figure 3.3).

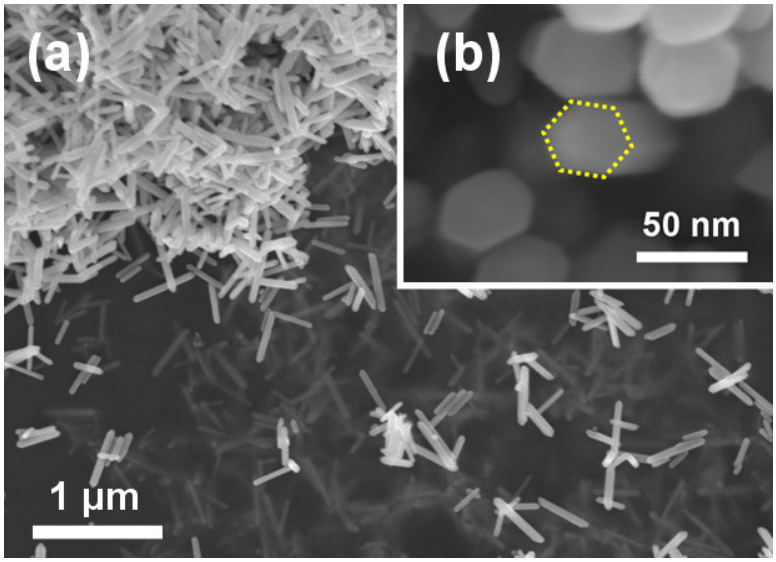


Figure 3.1. SEM images of α-$Fe_2O_3$ nanorods (a) at a low magnification and (b) end-view at a high magnification. The yellow dashed line in (b) outline the hexagonal structure of a single nanorod.

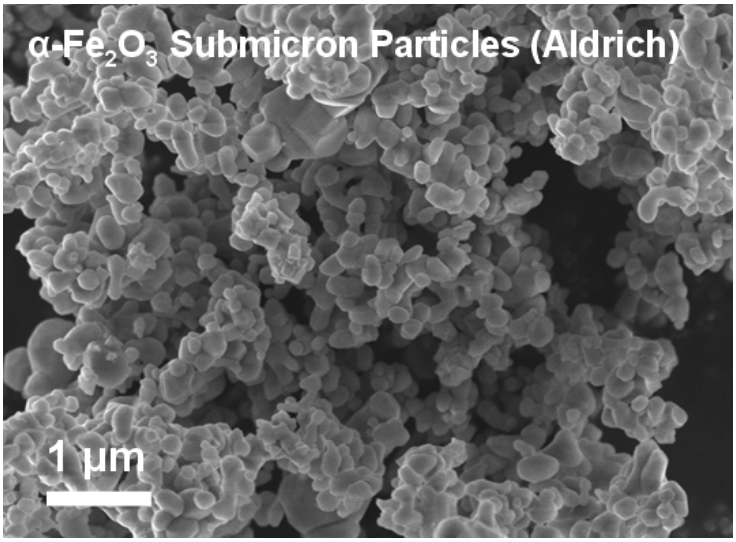


Figure 3.2. SEM image of α-$Fe_2O_3$ submicron particles

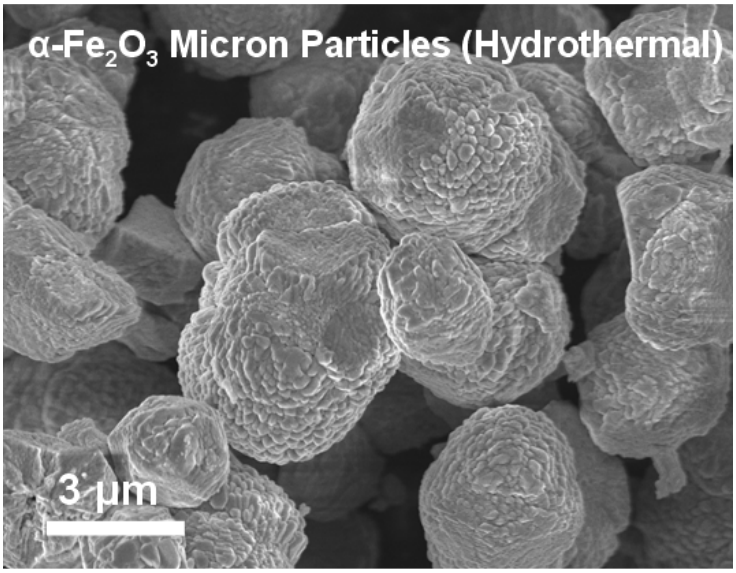


Figure 3.3. SEM image of α-$Fe_2O_3$ micron particles

A TEM image of a typical nanorod synthesized by the hydrothermal method is shown in Figure 3.4(a). As is evident from the periodic lattice fringes across the entire nanorod (Figure 3.4(b)), each of the nanorods is a monocrystal. The measured lattice spacing is 3.65 Å (Figure 3.4(c)), corresponding to the (012) plane of $\alpha$-$Fe_2O_3$. (The d spacing=3.68 Å for the (012) plane according to JCPDS # 00-033-0664). The angle between the parallel fringes and the long axis direction of the nanorod was determined to be 32.4°, which is in good agreement with the theoretical angle between the (012) plane and the [001] direction.[32] The X-ray powder diffraction pattern confirms the hematite structure (Figure 3.5).

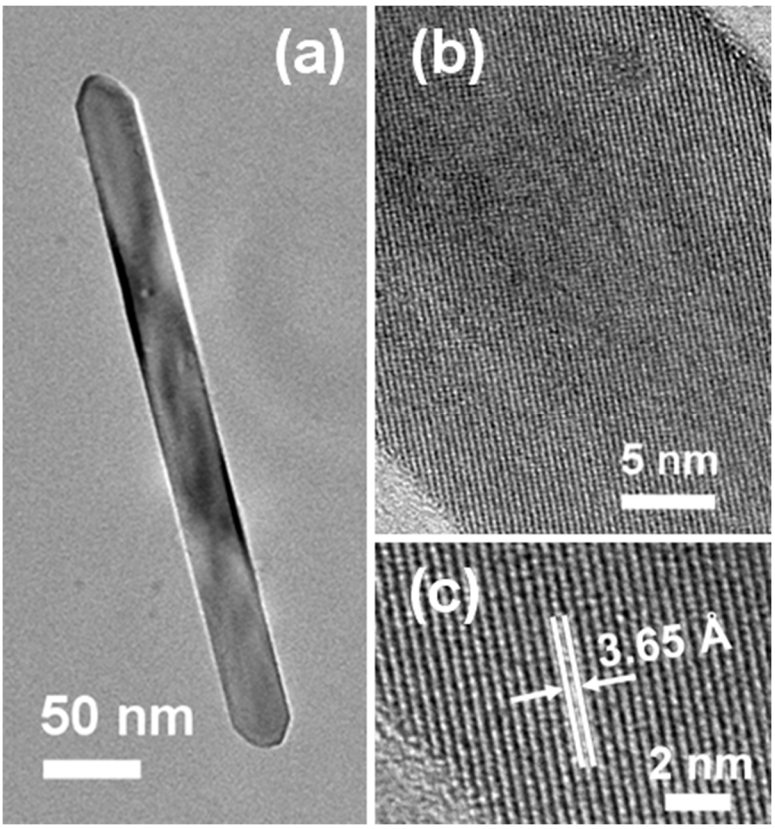


Figure 3.4. TEM images of a single α-$Fe_2O_3$ nanorod (a) at a low magnification (b) at a medium magnification and (c) at a high magnification. The white arrows and solid lines in (c) indicate two consecutive lattice fringes.

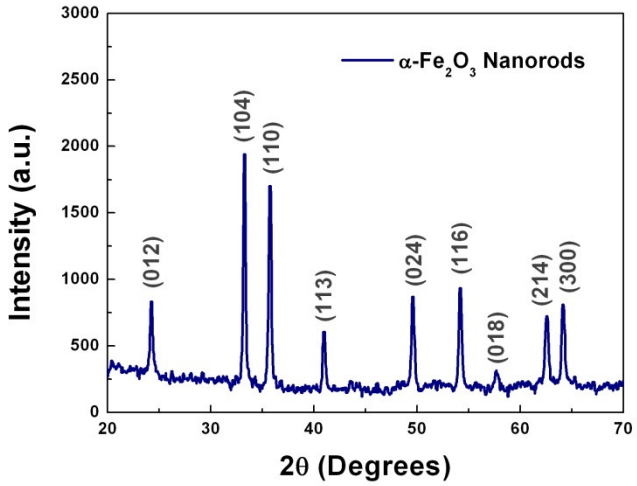


Figure 3.5. X-ray powder diffraction pattern of the α-$Fe_2O_3$ nanorods

Figure 3.6(a) shows the initial discharge and charge curves of the α-$Fe_2O_3$ nanorod based electrode for the first five cycles at 0.2 C rate. During the first discharge, the first plateau appears at 1.6 V vs. $Li/Li^+$, followed by a smooth voltage drop to approximately 1 V. This has been reported as a feature for lithium insertion in nanosized α-$Fe_2O_3$ to form $Li_xFe_2O_3$.[12, 34] The second plateau at ~0.87 V reflects the reduction of $Fe^{3+}$ to $Fe^0$. The first discharge and charge capacities are 1191 and 908 mAh $g^{-1}$, respectively. The initial irreversible capacity loss of the α-$Fe_2O_3$ nanorod electrode is 282 mAh $g^{-1}$, much smaller than that of iron oxide nanoparticles with diameters of ~10 nm, for which Wu et al. reported an irreversible capacity loss greater than 1000 mAh $g^{-1}$.[16] After the first cycle, the capacity of the α-$Fe_2O_3$ nanorod electrode studied here stabilizes at ~ 930 mAh $g^{-1}$, and no capacity fading is seen during the first five cycles. The initial irreversible

capacity loss could result from the formation of a solid electrolyte interface (SEI) on the iron oxide surface during the first lithium insertion process, which is a disadvantage of using nanostructure materials because the high electrode/electrolyte interfacial area may lead to more irreversible side reactions.[35] However, one dimensional nanostructures like nanorods can offer a small diameter to enhance lithium diffusion, and yet still provide a limited surface area to prevent excessive side reactions. Therefore, the α-$Fe_2O_3$ nanorod electrode can achieve both high reversible capacity and a low initial capacity loss.

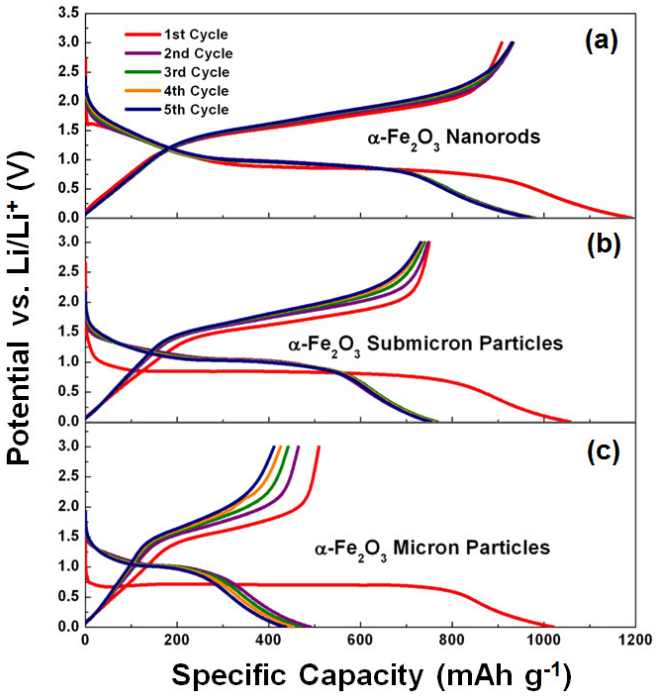


Figure 3.6. Voltage profiles of electrodes made with (a) α-$Fe_2O_3$ nanorods (b) α-$Fe_2O_3$ submicron particles (c) α-$Fe_2O_3$ micron-sized particles. All electrodes cycled at 0.2 C rate (201 mA $g^{-1}$).

The initial voltage profiles of the electrode made with α-$Fe_2O_3$ submicron particles (purchased from Aldrich) are shown in Figure 3.6(b). During the first discharge, only a long voltage plateau appears at 0.8 V, which is lower than that of the α-$Fe_2O_3$ nanorod electrode (0.87 V). The higher overpotential of the electrode made with α-$Fe_2O_3$ submicron particles compared to the electrode composed of nanorods means the smaller sized α-$Fe_2O_3$ nanorod is kinetically more favorable for lithium diffusion. The initial irreversible capacity loss of the electrode made with the α-$Fe_2O_3$ submicron particles was slightly higher than 300 mAh $g^{-1}$, and their capacity declines slowly after the first cycle (Figure 3.6(b)). The electrode made with hydrothermally synthesized micrometer sized α-$Fe_2O_3$ particles without adding a morphology controlling agent shows a voltage plateau at 0.7 V in the initial discharge curve (Figure 3.6(c)). The high overpotential was caused by the large α-$Fe_2O_3$ particle size which hinders lithium diffusion. The electrode made with micrometer sized α-$Fe_2O_3$ particles has a particularly high initial irreversible capacity loss greater than 500 mAh $g^{-1}$ (Figure 3.6(c)). The micrometer sized α-$Fe_2O_3$ particles should have less specific surface area than the hematite nanorods and the submicron-size particles, hence the major capacity loss was likely not only caused by irreversible SEI formation, but also due to the loss of electronic continuity upon disintegration of the α-$Fe_2O_3$ particles due to volume expansion and contraction during lithiation and delithiation steps. The capacity of the electrode with micrometer sized α-$Fe_2O_3$ particles fades much faster than that of the α-$Fe_2O_3$ nanorods and the submicron-size particles.

Reversible capacities of α-$Fe_2O_3$ electrodes made with nanorods, submicron particles and micron-sized particles cycled at 0.2 C rate up to 30 cycles are shown in Figure 3.7. The initial capacity of the electrode made with the submicron particles is near 750 mAh $g^{-1}$, dropping to ~ 700 mAh $g^{-1}$ after 20 cycles. Note that the electrochemical performance of our submicron particles is comparable in performance to electrodes with similar sizes of hematite particles and the same CMC binder as reported by Dahn and coworkers.[30] The initial reversible capacity of the electrode made with micrometer sized α-$Fe_2O_3$ is merely 500 mAh $g^{-1}$ and its reversible capacity drops within 10 cycles to 354 mAh $g^{-1}$, a value below the theoretical capacity of graphite (372 mAh $g^{-1}$), showing that the large volume change upon cycling can be accommodated by small, but not by large α-$Fe_2O_3$ particles. Overall, the electrode made with 40 nm x 400 nm α-$Fe_2O_3$ nanorods outperforms both the electrodes made with micron sized α-$Fe_2O_3$ particles and with submicron α-$Fe_2O_3$ particles, retaining a reversible capacity of ~ 900 mAh $g^{-1}$ after 30 cycles.

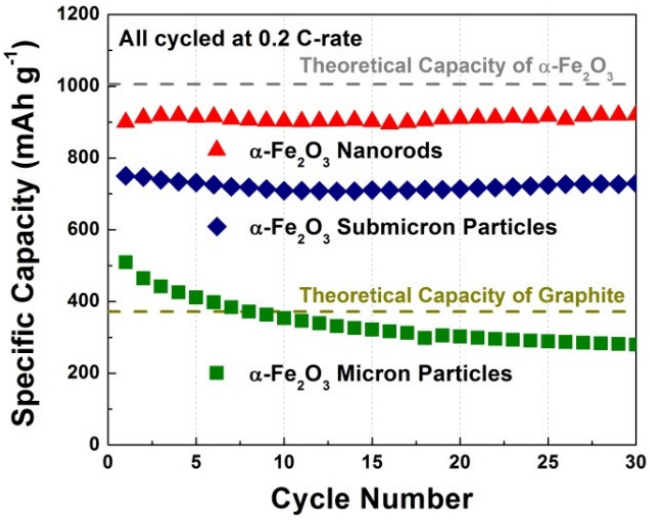


Figure 3.7. Reversible capacities of α-$Fe_2O_3$ electrodes made with nanorods, submicron particles and micron-sized particles. All electrodes cycled at 0.2 C rate (201 mA $g^{-1}$).

Electrodes made of α-$Fe_2O_3$ nanorods, submicron particles and micron-sized particles were also cycled with a higher current density, 0.5 C rate (503 mA $g^{-1}$) for 100 cycles. The initial voltage profiles of the first five cycles of these electrodes are shown in Figure 3.8, and the capacity retention for each electrode is plotted in Figure 3.9. Compared to the result for electrodes cycled at 0.2 C rate, the initial capacity of each electrode was lower when cycled at a 0.5 C rate. This is due to concentration polarization of Li ions in α-$Fe_2O_3$ resulting from a diffusion limited process, which is especially more obvious at the higher C rate. Cycling at higher current density not only results in a lower specific capacity, it can also induce larger localized strain because of the concentration polarization. For these reasons, the capacities of electrodes made of α-$Fe_2O_3$ submicron

particles and micron-sized particles dropped to around 500 mAh $g^{-1}$ and 200 mAh $g^{-1}$, separately, after 30 cycles at a 0.5 C rate (Figure 3.9). However, the electrode made of α-$Fe_2O_3$ nanorods can maintain a capacity as high as 800 mAh $g^{-1}$ within the first 30 cycles, more than twice the theoretical capacity of graphite. The hematite nanorods can provide particularly short $Li^+$ diffusion paths, accommodate the strain and thereby avoid the capacity loss upon cycling. What is interesting is that after 30 cycles the capacity of the α-$Fe_2O_3$ nanorod electrode kept increasing before leveling off at ~ 970 mAh $g^{-1}$ at the 90th cycle. Similar behavior for an α-$Fe_2O_3$ electrode with CMC as the binder has been reported by Dahn and coworkers.[30] Although the root cause of this phenomenon has yet to be determined, the electrochemical performance of α-$Fe_2O_3$ nanorods is obviously higher than α-$Fe_2O_3$ submicron particles and micron particles.

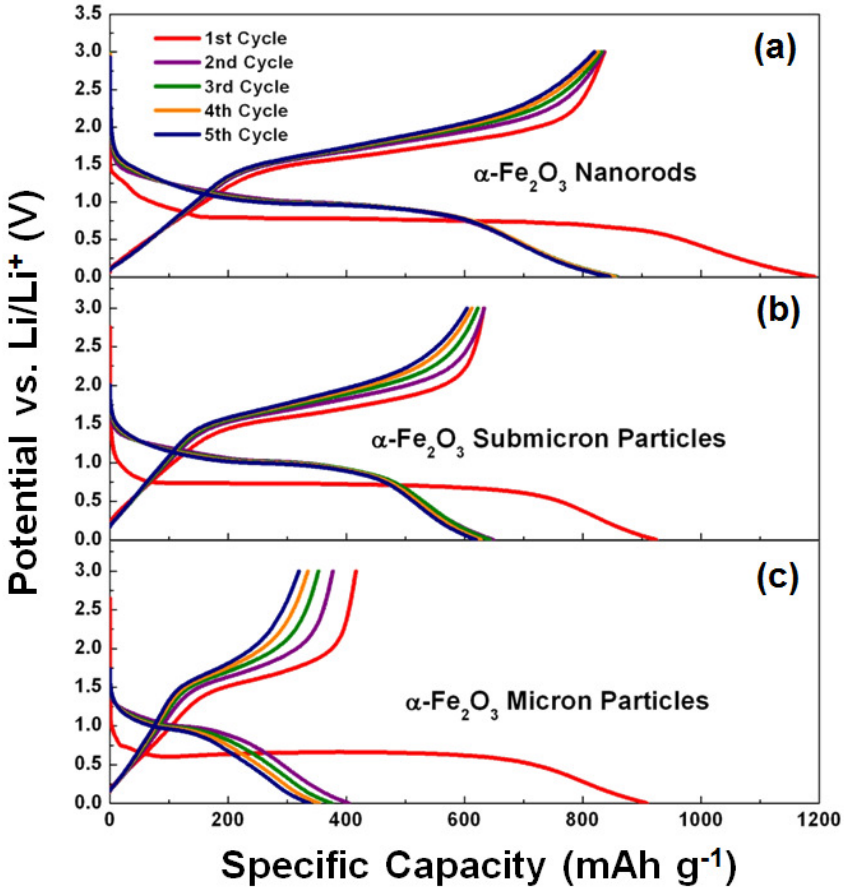


Figure 3.8. Voltage profiles of electrodes with (a) α-$Fe_2O_3$ nanorods (b) α-$Fe_2O_3$ submicron particles (c) α-$Fe_2O_3$ micron particles. All electrodes cycled at 0.5 C rate (503 mA $g^{-1}$).

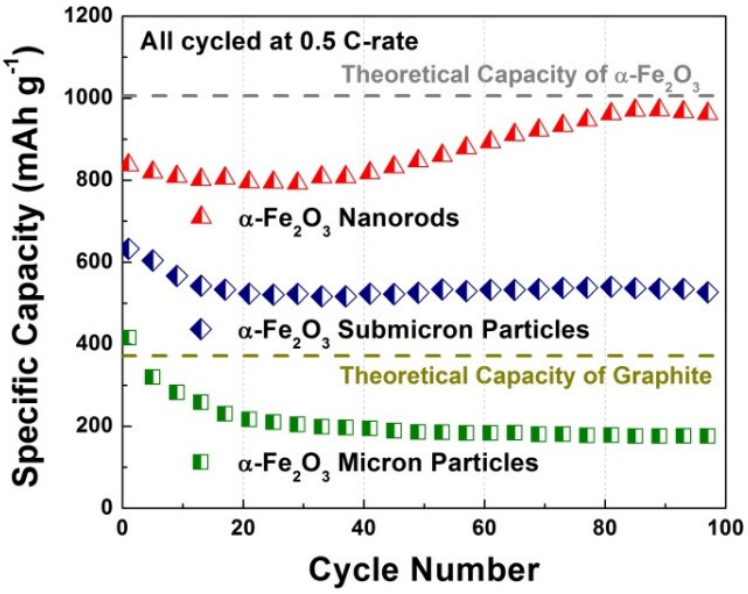


Figure 3.9. Reversible capacities of α-$Fe_2O_3$ electrodes made with nanorods, submicron particles and micron-sized particles. All electrodes cycled at 0.5 C rate (503 mA $g^{-1}$).

In order to better understand the failure mechanism of electrodes with large particle sizes, electrodes made of α-$Fe_2O_3$ micron sized particles have been investigated by SEM before and after cycling. The cycled electrode was disassembled from the coin cell and soaked into acetonitrile for 24 hours, then rinsed with ethanol to remove the residual electrolyte followed by drying under vacuum at 80 °C overnight before SEM imaging. Figure 3.10(a) shows the image of a pristine electrode with micron sized α-$Fe_2O_3$ particles which are well-surrounded by conductive carbon particles. After 100 cycles at 0.5 C rate, the micron sized α-$Fe_2O_3$ particles were pulverized and showed poor electrical continuity on both the interior and exterior of the hematite particle (Figure

3.10(b)). The changes of morphology for micron sized α-$Fe_2O_3$ particles before and after cycling can explain why the electrodes with large α-$Fe_2O_3$ particles performed poorly. Electrodes made of α-$Fe_2O_3$ nanorods with/without cycling were also investigated by the same method. Figure 3.10(c) shows a pristine electrode comprised of α-$Fe_2O_3$ nanorods before performing any electrochemical testing. After cycling, it can be seen that the surface of the α-$Fe_2O_3$ nanorod electrode was covered by a layer of material, which is possibly the SEI formed during the lithiation process (Figure 3.10(d)). Unlike the micron sized α-$Fe_2O_3$ particles which pulverize after cycling, the α-$Fe_2O_3$ nanorods maintain their morphology after 100 cycles at 0.5 C rate. It is clear that the strain generated during the lithiation/de-lithiation process can be accommodated by the α-$Fe_2O_3$ nanorods, but not by the large α-$Fe_2O_3$ particles which disintegrated and resulted in low reversible capacity.

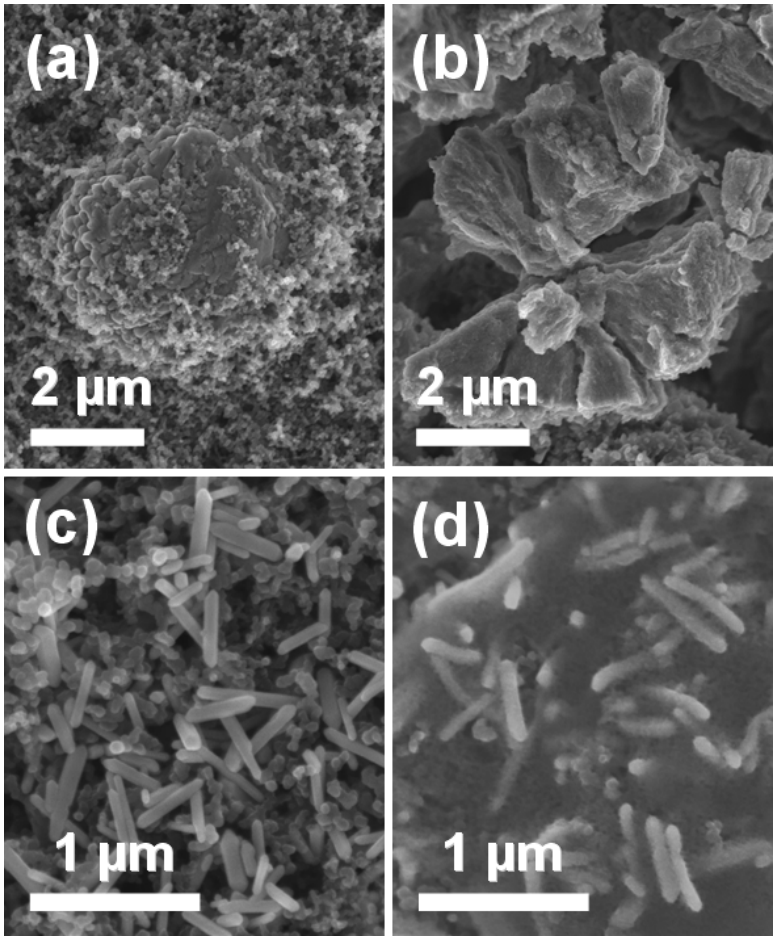


Figure 3.10. SEM images of (a) pristine α-$Fe_2O_3$ micron particles electrode (b) α-$Fe_2O_3$ micron particles electrode after 100 cycles at 0.5 C rate (c) pristine α-$Fe_2O_3$ nanorod electrode (d) α-$Fe_2O_3$ nanorod electrode after 100 cycles at 0.5 C rate.

The electrochemical impedance behavior of the various α-$Fe_2O_3$ electrodes were investigated to examine the kinetics of lithium ion transfer by using an electrochemical analyzer (CHI 604D, CHI). The impedance of the electrochemical system was interpreted in terms of Nyquist plots, which describe the gain and phase of the frequency response in

polar coordinates. Figure 3.11 shows the Nyquist plots for cells containing electrodes with different size α-$Fe_2O_3$ particles which were acquired individually under their open circuit voltage state after 100 cycles at 0.5 C rate. Electrochemical impedance spectroscopy (EIS) was carried out over a wide frequency range from 100 kHz to 0.01 Hz with an ac perturbation voltage of 5 mV. Each plot consists of a semicircle in the high frequency region which was attributed to the charge transfer process, and a sloping line in the low frequency region that related to the mass transfer of lithium ions. The electrochemical system can be simply modeled by a Randles equivalent circuit as shown in the inset of Figure 3.11,[36] where $R_\Omega$ is the ohmic resistance, $C_D$ is the double layer capacitance, $R_{CT}$ is the charge transfer resistance, and $Z_W$ is the Warburg impedance describing the solid state diffusion of $Li^+$ in α-$Fe_2O_3$. The results from fitting the model to performance data are summarized in Table 3.1. At very high frequencies (above 10 kHz), only the ohmic resistance can be observed, which is mainly due to (i) external connections, (ii) contact resistance, and (iii) ionic conduction within the electrolyte.[37] Because the same electrolyte and identical cell configurations were employed, all three electrodes have a similar value of $R_\Omega$ for the ohmic resistance (~ 18 Ω) obtained from the fitting result or which can be easily determined from the high frequency intercept with the real axis (x-axis) in the Nyquist plots. In the medium to high frequency region, from 10 Hz to 10 kHz, a semicircle appears for each cell which is attributed to an interfacial charge transfer coupled with a double layer capacitance. The charge transfer resistance can also be determined by fitting the Randles equivalent circuit or directly measuring the

diameter of the semicircle in the Nyquist plot. The electrode made of micron sized particles has a large charge transfer resistance, 30.2 Ω, significantly higher than that of the electrodes made of submicron particles (13.0 Ω) and nanorods (12.4 Ω). This result suggests that after cycling the electron transfer is more difficult in the electrode made of micron sized particles, which may have resulted from the pulverization of α-$Fe_2O_3$ during the lithiation/de-lithiation process as seen by SEM. At frequencies lower than 10 Hz, an inclined line is displayed for each spectrum which represents the diffusion of $Li^+$ in α-$Fe_2O_3$. The slope of the line for the α-$Fe_2O_3$ nanorod electrode is about 45° for frequencies ranging from 1 Hz to 10 Hz, which can be well described by the Warburg impedance as a semi-infinite linear diffusion process. At very low frequencies (lower than 1 Hz), the slope for the hematite nanorod electrode gets steeper which implies that the transport behavior has shifted from semi-infinite diffusion to finite diffusion.[38] Compared to the electrodes made of α-$Fe_2O_3$ submicron particles and α-$Fe_2O_3$ micron particles, the α-$Fe_2O_3$ nanorod electrode has a steeper slope in the lower frequency regions. This is attributed to the smaller average feature size of the α-$Fe_2O_3$ nanorods, hence both the bulk and surface of the α-$Fe_2O_3$ nanorods is more accessible to lithium-ions.

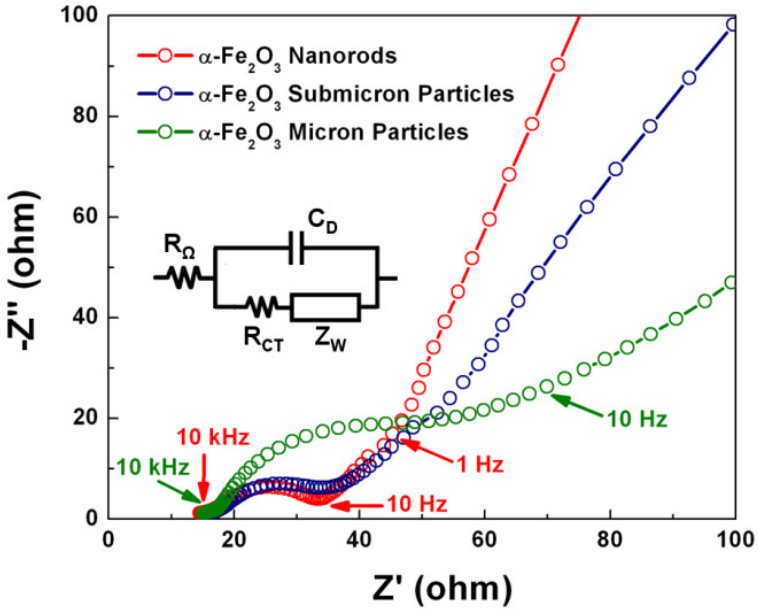


Figure 3.11. Electrochemical impedance spectroscopy of electrodes with α-$Fe_2O_3$ nanorods, submicron particles α-$Fe_2O_3$ and micron-sized particles α-$Fe_2O_3$. All measured after 100 cycles at 0.5 C rate.

Table 3.1. Electrochemical impedance spectroscopic data for electrodes with α-$Fe_2O_3$ nanorods, submicron particles α-$Fe_2O_3$ and micron-sized particles α-$Fe_2O_3$.

| electrode materials | $R_\Omega$ [Ω] | $R_{CT}$ [Ω] |
|---|---|---|
| α-$Fe_2O_3$ microparticles | 18.6 | 30.2 |
| α-$Fe_2O_3$ submicron particles | 19.2 | 13.0 |
| α-$Fe_2O_3$ nanorods | 18.4 | 12.4 |

In order to test the limit of the high rate capability of the α-$Fe_2O_3$ nanorod electrode, an additional cell was assembled and charged/discharged stepwise from 0.2 C to 5 C (0.2 C, 0.5 C, 1 C, 2 C, 5 C) , with each C rate for 10 cycles (Figure 3.12). There was always a capacity drop immediately after switching from a lower C rate to a higher C rate, which can be explained by the concentration polarization of Li ions in the α-$Fe_2O_3$ nanorods resulting from a diffusion limited process. The α-$Fe_2O_3$ nanorod electrode held its capacity for 0.2 C and 0.5 C, but started decaying slightly at 1C. Nevertheless, a reversible capacity as high as ~ 800 mAh $g^{-1}$ can still be held at 1 C for 10 cycles. As the C rate increased from 1 C to 2 C and then to 5 C, the capacity retention of the hematite nanorod electrode became worse, only exhibiting a capacity of ~ 300 mAh $g^{-1}$ at 5 C for 10 cycles. The cell after cycling at various C rates up to 5 C was disassembled to investigate the issue associated with the capacity fading. The SEM image in Figure 3.13 shows that even cycled at a C rate as high as 5 C, corresponding to a current density of 5A $g^{-1}$, the nanorods can still be observed. Although the nanorods were distorted after cycling, which could be from the strain generated by the fast lithium insertion/de-insertion, they didn't shatter and lose their continuity. Hence, there might be other reasons leading to the fast capacity fading at higher C rates rather than the disintegration of the hematite nanorods. The failure of the CMC binder could be one of the reasons because the adhesion between the electrode materials to the current collector was not good after cycling at high C rates when compared to the electrode cycled at lower C rates. Dahn et al. has noted the importance of binder choice for materials with substantial

volume change upon lithiation.[30] Employing elastomeric polymers as the binder could possibly further improve the high rate performance of the α-$Fe_2O_3$ nanorod electrode.

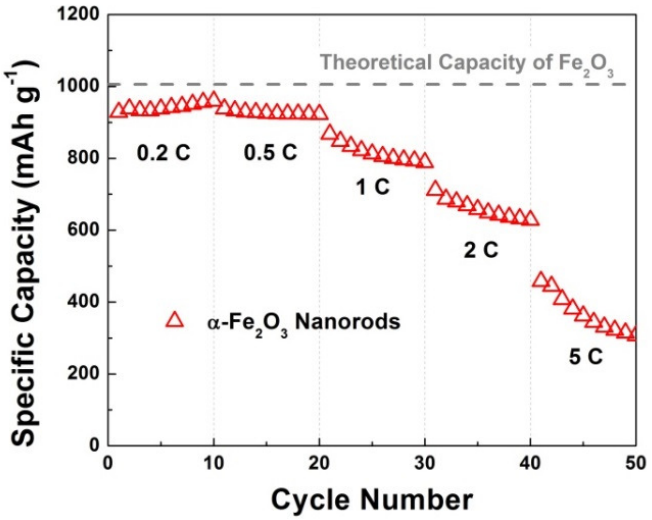


Figure 3.12. Reversible capacities of electrode made with α-$Fe_2O_3$ nanorods cycled at various C rates.

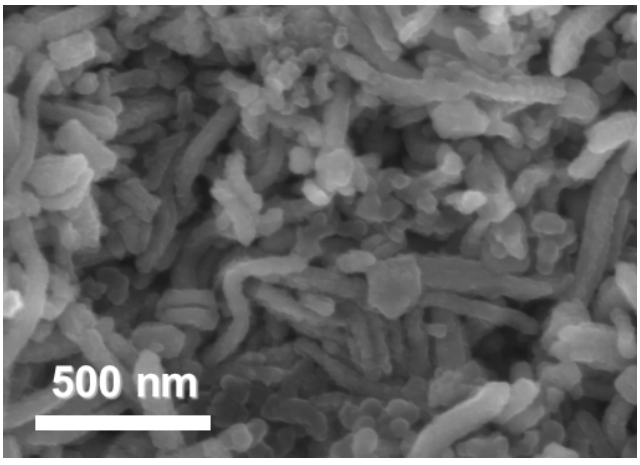


Figure 3.13. SEM image of α-$Fe_2O_3$ nanorod electrode after various C rates test up to 5 C.

## CONCLUSIONS

In summary, hydrothermally synthesized monocrystalline hematite nanorods were investigated as an anode material for lithium ion batteries. Electrodes made of α-$Fe_2O_3$ nanorods outperformed electrodes fabricated from submicron and micron sized particles in terms of reversible capacity, cyclability, and rate capability toward lithium storage. High initial reversible capacities of 908 mAh $g^{-1}$ at 0.2 C rate and 837 mAh $g^{-1}$ at 0.5 C rate were achieved for α-$Fe_2O_3$ nanorod electrode, and these capacities were fully retained after numerous cycles. The excellent performance of the hematite nanorod electrode can be attributed to the small diameter elongated nanostructure that provides a short diffusion path for lithium-ion diffusion, and also accommodates the strain generated during the lithiation/de-lithiation process.

## REFERENCES


1. Kay, A.; Cesar, I.; Gratzel, M., *J. Am. Chem. Soc.* **2006,** *128* (49), 15714-15721.

2. Hahn, N. T.; Ye, H. C.; Flaherty, D. W.; Bard, A. J.; Mullins, C. B., *ACS Nano* **2010,** *4* (4), 1977-1986.

3. Hahn, N. T.; Mullins, C. B., *Chem. Mater.* **2010,** *22* (23), 6474-6482.

4. Chen, J.; Xu, L. N.; Li, W. Y.; Gou, X. L., *Adv. Mater. (Weinheim, Ger.)* **2005,** *17*, 582-586.

5. Hassoun, J.; Croce, F.; Hong, I.; Scrosati, B., *Electrochem. Commun.* **2011,** *13* (3), 228-231.

6. Manthiram, A., *J. Phys. Chem. Lett.* **2011,** *2* (3), 176-184.

7. Goodenough, J. B.; Kim, Y., *Chem. Mater.* **2010,** *22* (3), 587-603.

8. Li, H.; Balaya, P.; Maier, J., *J. Electrochem. Soc.* **2004,** *151* (11), A1878-A1885.

9. Abraham, K. M.; Pasquariello, D. M.; Willstaedt, E. B., *J. Electrochem. Soc.* **1990,** *137* (3), 743-749.

10. Zou, L.; Kang, F. Y.; Li, X. H.; Zheng, Y. P.; Shen, W. C.; Zhang, J., *J. Phys. Chem. Solids* **2008,** *69*, 1265-1271.

11. Nuli, Y. N.; Zhang, P.; Guo, Z. P.; Liu, H. K., *J. Electrochem. Soc.* **2008,** *155* (3), A196-A200.

12. Larcher, D.; Masquelier, C.; Bonnin, D.; Chabre, Y.; Masson, V.; Leriche, J. B.; Tarascon, J. M., *J. Electrochem. Soc.* **2003,** *150* (1), A133-A139.

13. Kitaura, H.; Takahashi, K.; Mizuno, F.; Hayashi, A.; Tadanaga, K.; Tatsumisago, M., *J. Electrochem. Soc.* **2007,** *154* (7), A725-A729.

14. Arico, A. S.; Bruce, P.; Scrosati, B.; Tarascon, J. M.; Van Schalkwijk, W., *Nat. Mater.* **2005,** *4* (5), 366-377.

15. Wang, Y.; Cao, G. Z., *Adv. Mater. (Weinheim, Ger.)* **2008,** *20* (12), 2251-2269.

16. Wu, M. S.; Ou, Y. H.; Lin, P., *J. Electrochem. Soc.* **2011,** *158* (3), A231-A236.

17. Wu, X. L.; Guo, Y. G.; Wan, L. J.; Hu, C. W., *J. Phys. Chem. C* **2008,** *112* (43), 16824-16829.

18. Ma, J. M.; Lian, J. B.; Duan, X. C.; Liu, X. D.; Zheng, W. J., *J. Phys. Chem. C* **2010,** *114* (24), 10671-10676.

19. Chen, J. S.; Zhu, T.; Yang, X. H.; Yang, H. G.; Lou, X. W., *J. Am. Chem. Soc.* **2010,** *132* (38), 13162-13164.

20. Liu, J. P.; Li, Y. Y.; Fan, H. J.; Zhu, Z. H.; Jiang, J.; Ding, R. M.; Hu, Y. Y.; Huang, X. T., *Chem. Mater.* **2010,** *22* (1), 212-217.

21. Kim, H. S.; Piao, Y.; Kang, S. H.; Hyeon, T.; Sung, Y. E., *Electrochem. Commun.* **2010,** *12* (3), 382-385.

22. Reddy, M. V.; Yu, T.; Sow, C. H.; Shen, Z. X.; Lim, C. T.; Rao, G. V. S.; Chowdari, B. V. R., *Adv. Funct. Mater.* **2007,** *17*, 2792-2799.

23. Chun, L.; Wu, X. Z.; Lou, X. M.; Zhang, Y. X., *Electrochim. Acta* **2010,** *55* (9), 3089-3092.

24. Zeng, S. Y.; Tang, K. B.; Li, T. W.; Liang, Z. H.; Wang, D.; Wang, Y. K.; Qi, Y. X.; Zhou, W. W., *J. Phys. Chem. C* **2008,** *112* (13), 4836-4843.

25. Zhou, W.; Lin, L. J.; Wang, W. J.; Zhang, L. L.; Wu, Q. O.; Li, J. H.; Guo, L., *J. Phys. Chem. C* **2011,** *115* (14), 7126-7133.

26. Wu, C. Z.; Yin, P.; Zhu, X.; OuYang, C. Z.; Xie, Y., *J. Phys. Chem. B* **2006,** *110* (36), 17806-17812.

27. Liu, H.; Wang, G. X.; Park, J.; Wang, J.; Zhang, C., *Electrochim. Acta* **2009,** *54* (6), 1733-1736.

28. Song, Y. Q.; Qin, S. S.; Zhang, Y. W.; Gao, W. Q.; Liu, J. P., *J. Phys. Chem. C* **2010,** *114* (49), 21158-21164.

29. Tartaj, P.; Amarilla, J. M., *J. Power Sources* **2011,** *196* (4), 2164-2170.

30. Li, J.; Dahn, H. M.; Krause, L. J.; Le, D. B.; Dahn, J. R., *J. Electrochem. Soc.* **2008,** *155* (11), A812-A816.

31. Beattie, S. D.; Larcher, D.; Morcrette, M.; Simon, B.; Tarascon, J. M., *J. Electrochem. Soc.* **2008,** *155* (2), A158-A163.

32. Li, Z. M.; Lai, X. Y.; Wang, H.; Mao, D.; Xing, C. J.; Wang, D., *Nanotechnology* **2009,** *20* (24), 245603.

33. Eggleston, C. M.; Hochella, M. F., *Am. Mineral.* **1992,** *77* (9-10), 911-922.

34. Larcher, D.; Bonnin, D.; Cortes, R.; Rivals, I.; Personnaz, L.; Tarascon, J. M., *J. Electrochem. Soc.* **2003,** *150* (12), A1643-A1650.

35. Bruce, P. G.; Scrosati, B.; Tarascon, J. M., *Angew. Chem. Int. Edit.* **2008,** *47* (16), 2930-2946.

36. Bard, A. J.; Faulkner, L. R., *Electrochemical Methods: Fundamentals and Applications*. 2nd ed.; Wiley: New York, 2001.

37. Ruffo, R.; Hong, S. S.; Chan, C. K.; Huggins, R. A.; Cui, Y., *J. Phys. Chem. C* **2009,** *113* (26), 11390-11398.

38. Yu, P.; Ritter, J. A.; White, R. E.; Popov, B. N., *J. Electrochem. Soc.* **2000,** *147* (6), 2081-2085.

# Chapter 4: $SnO_2$ and $TiO_2$-Supported-$SnO_2$ Lithium Battery Anodes with Improved Electrochemical Performance

## INTRODUCTION

Higher capacity, higher power density, longer cycle life and safer lithium ion batteries are being developed, particularly for vehicular applications.[1] These properties depend primarily on the electrochemically reactive electrode material. Commercially available Li-ion batteries built with graphite anodes lose capacity when cycled at high rates because of structural/mechanical changes in their lithiated/delithiated graphite,[2] and their safety is a cause of some concern.[3, 4] For these reasons alternative anode materials are sought. One of the most extensively studied alternative anode materials has been $SnO_2$. The reaction of Li with $SnO_2$ initially produces Sn and $Li_2O$, then a series of tin-lithium alloys (Reactions (4.1) and (4.2)):[5]

$$SnO_2 + 4\ Li^+ + 4\ e^- \rightarrow 2\ Li_2O + Sn \qquad (4.1)$$

$$Sn + x\ Li^+ + x\ e^- \leftrightarrow Li_xSn\ (0 \leq x \leq 4.4) \qquad (4.2)$$

Reaction (4.1) is generally irreversible, while the formation of the alloys (Reaction (4.2)) is reversible. A series of Li-Sn alloys ($Li_2Sn_5$, LiSn, $Li_7Sn_3$, $Li_5Sn_2$, $Li_{13}Sn_5$, $Li_7Sn_2$, and $Li_{22}Sn_5$) is formed at potentials between 0 V and 0.6 V versus $Li/Li^+$.[6] Up to 4.4 Li atoms can be stored per atom of Sn ($Li_{22}Sn_5$), providing a maximum theoretical capacity of 782 mAh $g^{-1}$ (or 5400 Ah $L^{-1}$),[7] exceeding the 372 mAh $g^{-1}$ (or 837

Ah $L^{-1}$) theoretical capacity of the graphite anode. The full lithiation/de-lithiation of Sn is associated with a 250 % volume change,[8] resulting in rapid capacity fading.[6, 9] Wu and co-workers, who followed the evolution of the interior structure of Sn-particle based electrodes by in-situ X-ray transmission microscopy,[10] observed cracking of the Sn particles as they expanded upon their first lithiation. It is known that small-grained ("nanostructured") electrode materials accommodate large strains and the short diffusion distance in the small grains provides for rapid $Li^+$ insertion/de-insertion,[11, 12] and the capacity is better retained with nanostructured $SnO_2$ morphologies.[13-17]

$SnO_2$-based nanocomposite materials, like $SnO_2$/carbon composites, have been reported to show improved cycling performance for lithium storage because of the additional support from carbon.[18-20] The cyclability of the $SnO_2$-based lithium anodes has also been improved by metal-oxide buffering of the excessive volume change.[21-26] Partially crystallized $SnO_2/TiO_2$ electrodes with varying concentrations of $TiO_2$ were investigated by Chibirova and coworkers, [27-29] who incorporated up to 20 mol % $TiO_2$, improving the cyclability upon increasing the $TiO_2$ content. Even though the cycling stability improved, the reversible capacity of their highest $TiO_2$-content $Ti_{0.2}Sn_{0.8}O_2$ electrodes still dropped to less than 300 mAh $g^{-1}$ in 40 cycles. Indris and co-workers reported a nanocrystalline $Ti_{2/3}Sn_{1/3}O_2$ anode of cassiterite-$SnO_2$ and rutile-$TiO_2$, with a reversible capacity of 300 mAh $g^{-1}$ for 100 cycles at a 0.05 C rate.[30] Its capacity decreased rapidly upon increasing the rate, dropping below 100 mAh $g^{-1}$ at 1 C.

In the initial half-cycle, lithiated titania is formed (Reaction (4.3)):[31]

$$xLi^+ + TiO_2 + xe^- \rightarrow Li_xTiO_2 \quad (4.3)$$

In subsequent cycles the $Li_xTiO_2$ is reversibly lithiated/delithiated near 1.4 V vs. lithium (Reaction (4.4)).[32]

$$Li_xTiO_2 \leftrightarrow Li_{x-y}TiO_2 + yLi^+ + ye^- \quad (4.4)$$

The kinetics of lithium insertion/de-insertion in $Li_xTiO_2$ electrodes has been investigated by Cantao et al., who concluded that the bulk-diffusion of $Li^+$ is the rate limiting process.[33] This implies that the rate capability of the $Li_xTiO_2$ is determined by the characteristic diffusion length of the material, *i.e.*, by whether or not the diameter of $Li_xTiO_2$ particles is smaller than the diffusion length. Lithium insertion in the two crystalline phases of $TiO_2$, rutile and anatase, has been investigated.[34-41] The insertion of lithium into bulk rutile $TiO_2$ is highly anisotropic, practically one dimensional, hindering the lithium ions from reaching thermodynamically favorable sites.[42, 43] Anatase $TiO_2$ can be lithiated to form two phases, a lithium poor phase, $Li_{0.01}TiO_2$, and a lithium rich phase, $Li_{0.6}TiO_2$,[44] with the rate of $Li^+$ diffusion at the boundary between these two phases limiting the rate of its insertion.[45] Amorphous $TiO_2$-derived $Li_xTiO_2$ has a higher rate capacity than anatase $TiO_2$ even with similar morphology, implying that $Li^+$ diffuses more rapidly in amorphous $Li_xTiO_2$.[46] Hence, use of amorphous $TiO_2$ could possibly improve the rate of $TiO_2/SnO_2$ composite anodes.

In this chapter, we report a $SnO_2$ nanoparticle based electrode and an amorphous $TiO_2$-supported $SnO_2$ nanocomposite formed of equimolar amounts of the Sn and Ti oxides. By decreasing the upper cutoff voltage from 1.5 V to 1.0 V, both the $SnO_2$-based anode and the $TiO_2$-supported-$SnO_2$ anode show improved cyclability. The $TiO_2/SnO_2$ nanocomposite anodes outperform the $SnO_2$ anodes in terms of capacity retention, Coulombic efficiency, and high rate capability toward lithium storage.

## EXPERIMENTAL METHODS

*Synthesis of the $SnO_2/TiO_2$ Nanocomposite:* The $SnO_2/TiO_2$ nanocomposite was synthesized by cetyltrimethylammonium bromide (CTAB) assisted co-precipitation. 0.7 ml of Stannic chloride and 1.6 ml of titanium(IV) butoxide were dissolved in 50 mL anhydrous isopropanol. CTAB (1.3 g) was dissolved in a mixture of 50 mL isopropanol and 10 mL 30-33 % ammonium hydroxide and was stirred at 0 - 5 °C while the $SnCl_4$/Ti-butoxide solution was added drop-wise. The precipitated mixed oxide was collected by filtration and dried at 70°C, then fired for 10h, the temperature ramped up at 2.5°C/min to 350°C so as to completely oxidize the CTAB to gaseous water, $CO_2$, HBr and $N_2$ rather than partially pyrolyzing it to carbon upon rapid heating.

*Characterizations:* The commercial tin oxide nanoparticles ($SnO_2$ NP, <100 nm, Aldrich) and the synthesized $SnO_2/TiO_2$ nanocomposite were characterized by scanning transmission electron microscopy (STEM) using a Hitachi S-5500 electron microscope

equipped with a Bruker EDS Quantax 4010 energy dispersive X-ray spectroscopy (EDS) detector for elemental analysis. For transmission electron microscopy (TEM) a JEOL 2010F TEM was used. X-ray diffraction (XRD) patterns were obtained with a Bruker-Nonius D8 Advance diffractometer. The specific surface area was measured by the Brunauer-Emmett-Teller (BET) method, with nitrogen adsorption monitored by a NOVA 2000 analyzer at 77K.

*Electrochemical Measurements:* The $SnO_2$ NP electrodes and $SnO_2/TiO_2$ electrodes were prepared by forming an aqueous slurry of the $SnO_2$ nanoparticles or the as-prepared $SnO_2/TiO_2$ nanocomposite (60 wt%) with conductive carbon black (Super P-Li, Timcal) (20 wt %) and 90 kDa sodium carboxy-methylcellulose (Aldrich) (20 wt %). Each slurry was cast onto a Cu foil using an automatic applicator and a notch bar with 100 μm clearance, then dried in a vacuum oven at 120°C for 12 hrs. After cooling to room temperature, the cast film was punched into disks, which constituted the working electrodes of 2032 type coin cells. The cells, assembled in an argon-atmosphere glove-box, had lithium foil counter/reference electrodes, polypropylene (Celgard 2400, Celgard) membrane separators and a 1M $LiPF_6$ in EC/DMC (1:1 wt/wt) (LP30, EMD Chemicals) electrolyte. The cells were galvanostatically cycled using a multichannel battery test system (BT 2143, Arbin). An electrochemical workstation (CHI 604D, CH Instruments) was used for cyclic voltammetry, carried out in a potential range between 50 mV to 3 V versus $Li/Li^+$ at a 0.1 mV $s^{-1}$ scan rate. All specific capacities discussed in this chapter, if not otherwise specified, are with respect to the weight of $SnO_2$ in the electrode.

## RESULTS AND DISCUSSION

The STEM image (Figure 4.1(a)) of the prepared $SnO_2/TiO_2$ nanocomposite taken in bright field mode at a relatively low magnification showed that the sizes of the nanocomposite particles were narrowly distributed and their average particle size was ~10 nm (Figure 4.1(b)). In the contrast, the $SnO_2$ nanoparticles that were acquired from Aldrich have a wide particle size distribution, ranging from ~5 nm to ~100 nm, as seen from the STEM image in Figure 4.2.

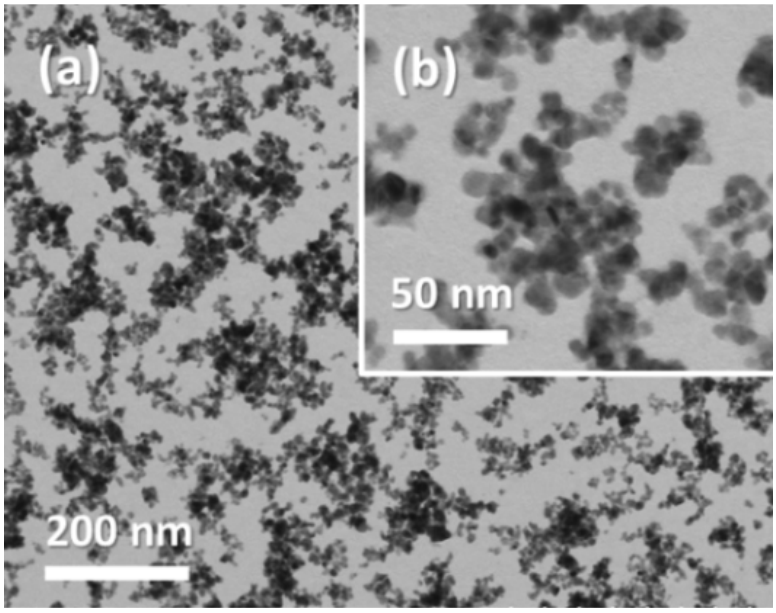


Figure 4.1. STEM images of the $SnO_2/TiO_2$ nanocomposite examined (a) at a low magnification and (b) at a high magnification.

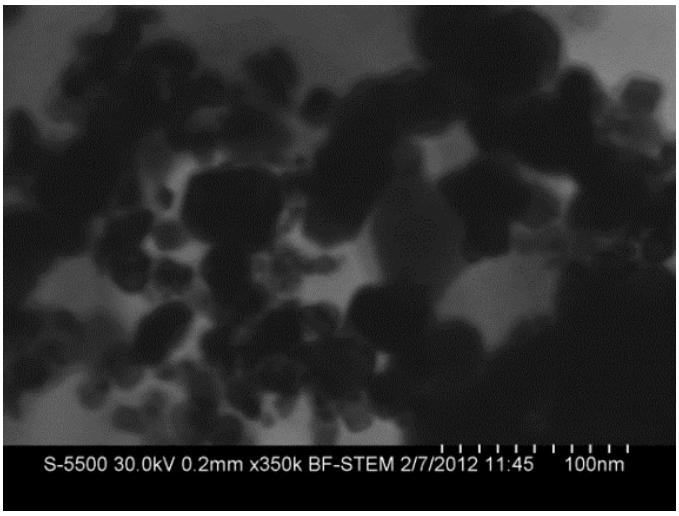


Figure 4.2. STEM image of the $SnO_2$ nanoparticles (Aldrich).

The average Sn/Ti molar ratio of the nanocomposite was 0.99, as determined by performing EDS analysis on five different spots of the nanocomposite under SEM observations. EDS elemental mappings from a selected area of the nanocomposite cluster (Figure 4.3(a)) showed that the Sn and Ti are evenly and uniformly distributed in the nanocomposite (Figure 4.3 (b) and (c)).

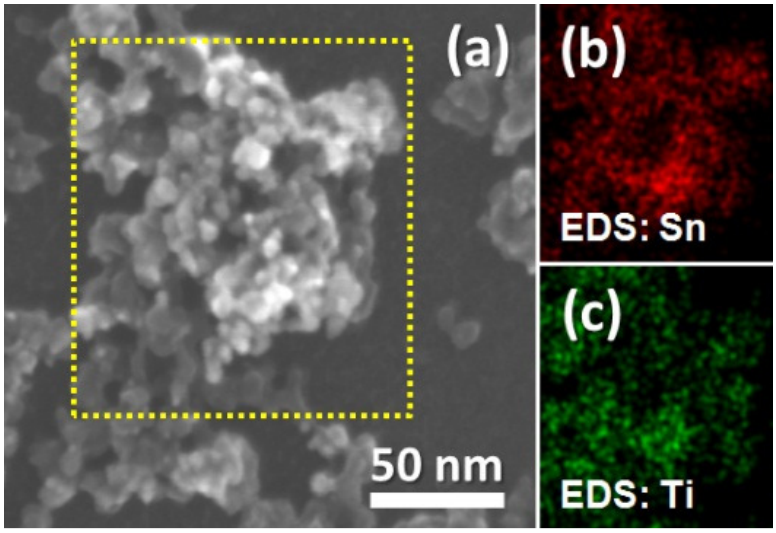


Figure 4.3. (a) SEM image of the $SnO_2/TiO_2$ nanocomposite for which a square region (yellow dashed line) was selected for EDS mapping for element (b) Sn and (c) Ti.

All the peaks in the X-ray powder diffractogram (Figure 4.4) of the $SnO_2/TiO_2$ nanocomposite were directly indexed to the cassiterite phase of $SnO_2$, suggesting that the $TiO_2$ was amorphous. The width of the peaks was consistent with a ~40 Å particle size, estimated from the full-width at half maximum (FWHM) of the $SnO_2$ (110) peak through the Scherrer equation. There was no peak shift or split in the XRD pattern of the $SnO_2/TiO_2$ powder, consistent with a two-phase crystalline $SnO_2$/amorphous $TiO_2$ nanocomposite, not with a $Sn_xTi_{1-x}O_2$ solid solution.[47, 48] At the 350 °C calcination temperature only the $SnO_2$ crystallized.[49] Typically, amorphous $TiO_2$ needs to be heated to 450 °C to change to anatase, and to further transform to the rutile phase requires temperatures above 700 °C.[50, 51] Figure 4.5(a) in the ESI shows a TEM image of the

prepared $SnO_2/TiO_2$ nanocomposite, which reveals the sample is partially-crystallized. The lattice spacing of a crystalline particle was measured as 3.32 Å (Figure 4.5(b), corresponding to the (110) plane of cassiterite $SnO_2$. The results of the TEM observation support the results from XRD measurements for the $SnO_2/TiO_2$ nanocomposite. In addition, the X-ray powder diffraction pattern of the commercial $SnO_2$ nanoparticles is also shown in Figure 4.4, which confirms the cassiterite structure. The narrower FWHM of the XRD peaks indicate that the $SnO_2$ nanoparticles have a larger average crystallite size than the prepared $SnO_2/TiO_2$ nanocomposite.

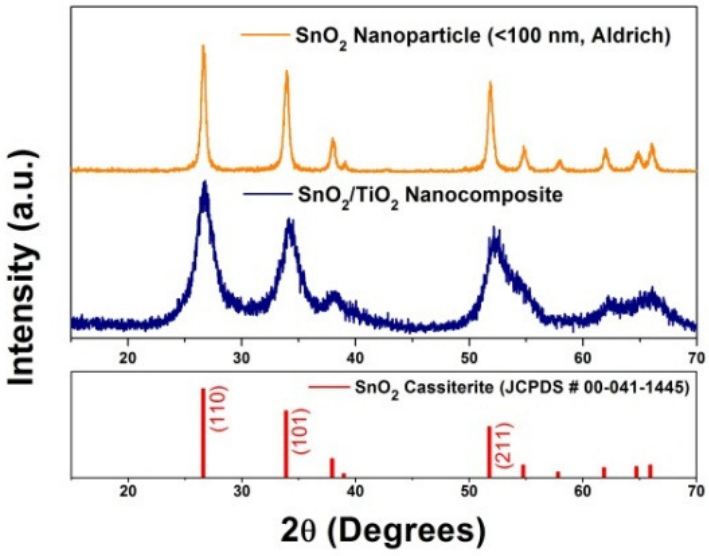


Figure 4.4. X-ray powder diffraction pattern of the $SnO_2$ nanoparticle and the $SnO_2/TiO_2$ nanocomposite.

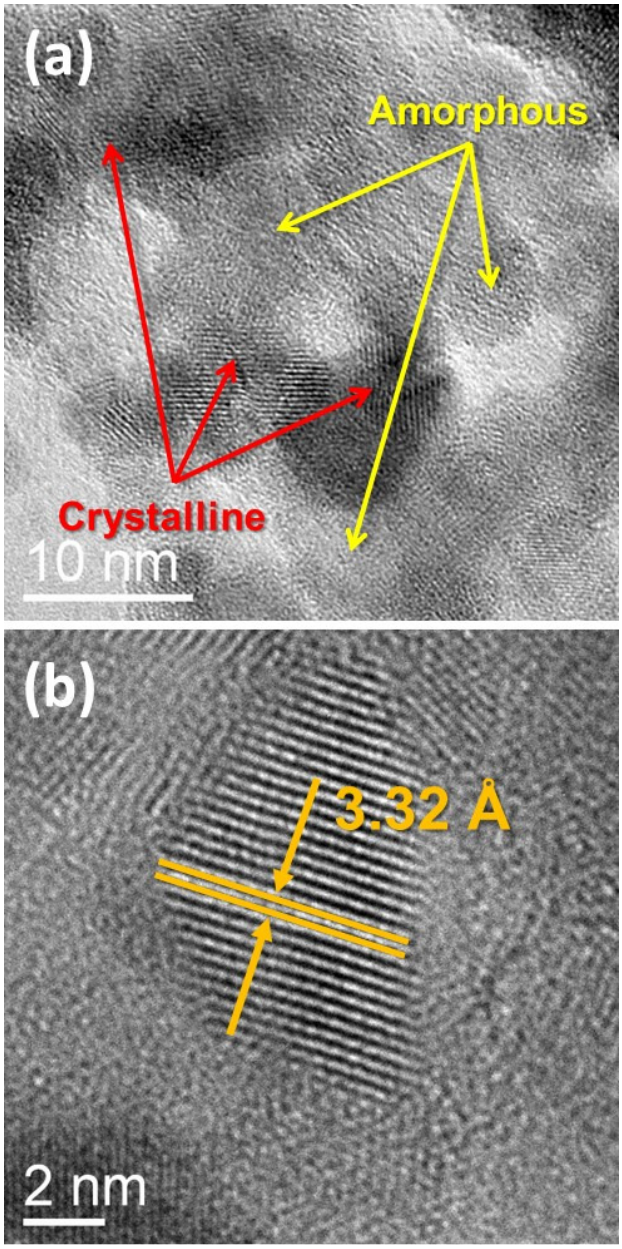


Figure 4.5. TEM images of the $SnO_2/TiO_2$ nanocomposite (a) at a low magnification and (b) at a high magnification. The orange arrows and solid lines in (b) indicate two consecutive fringes.

Figure 4.6 shows the nitrogen adsorption/desorption isotherm for the $SnO_2/TiO_2$ nanocomposite. The isotherm represents typical multi-layer adsorption behavior. A small hysteresis loop was observed between the adsorption and the desorption curves, suggestive of a low porosity structure for the nanocomposite.[52] The BET specific surface area of the $SnO_2/TiO_2$ nanocomposite is high, approximately 100 $m^2/g$. The specific surface area of the commercial $SnO_2$ nanoparticle is ~45 $m^2/g$.[53]

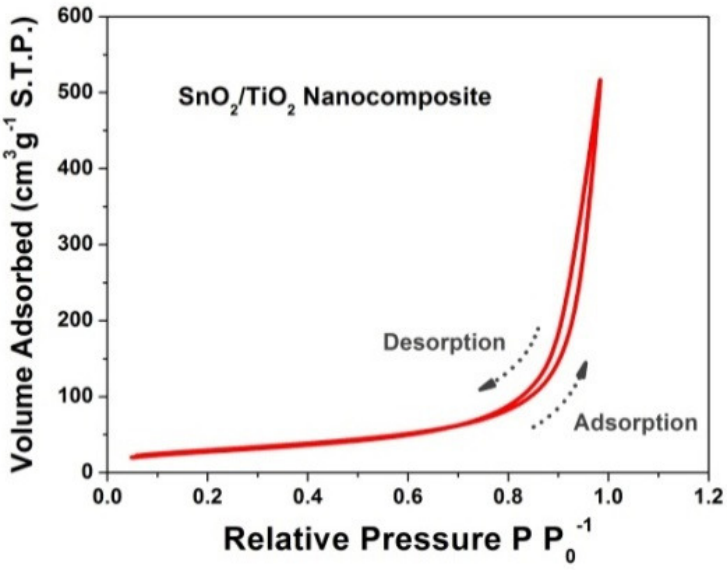


Figure 4.6. BET isotherm of the synthesized $SnO_2/TiO_2$ nanocomposite.

Figure 4.7 shows the first three cycles of cyclic voltammograms of the $SnO_2/TiO_2$ nanocomposite electrode. In the first cycle a small reduction peak at 1.02 V and two major reduction peaks at 0.83 V and 0.10 V are seen, representing respectively the formation of the solid electrolyte interface (SEI), the reduction of $SnO_2$ to metallic Sn and

the formation of the Li-Sn alloy, respectively.[54, 55] The first two reactions are generally irreversible. However, the lithium alloying/de-alloying reactions of the Li-Sn system are reversible, as evidenced by the oxidation peaks which appear at 0.57 V during the positive scans of the first and following cycles. The broad 1 V to 2 V wave is attributed to the partial reduction/oxidation of Sn[56] and to insertion/de-insertion of lithium ions in amorphous $TiO_2$.[57]

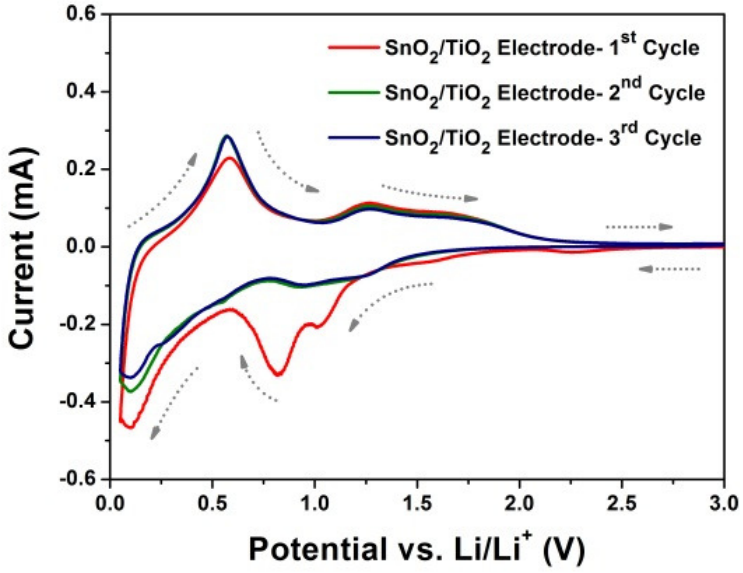


Figure 4.7. Cyclic voltammograms of the $SnO_2/TiO_2$ electrode with a scan rate of 0.1 mV $s^{-1}$ between 50 mV and 3 V. The dashed-arrows represent the sweep direction.

Figure 4.8 shows the dependence of the potential on the cycle number for $SnO_2/TiO_2$ nanocomposite electrodes cycled at a 0.2 C rate between a lower cutoff voltage of 50 mV and upper cutoff voltages of 1.5 V and 1.0 V. In the first half-cycle

starting from the open circuit potential, lithium reduces the tin oxide to form $Li_xSn$ alloys and inserts in the amorphous $TiO_2$ to form lithium titanates ($Li_xTiO_2$) between 1 V to 2 V vs. $Li/Li^+$.[57] The large irreversible capacity observed in the first cycle is associated with the formation of $Li_2O$ and with the reduction of the solid/electrolyte interface. Upon cycling to 1.5 V, the initial reversible capacity of 830 mAh $g^{-1}$ fades to 760 mAh $g^{-1}$ in 5 cycles. The fading is associated with the diminishing shoulder between 1.0 V to 1.5 V (Figure 4.8(a)). Since the Li-Sn alloying reactions take place mainly below 1 V vs. $Li/Li^+$, the initial capacity fading when cycled up to 1.5 V is possibly attributed to the degradation of amorphous titania, which reacts with lithium above 1 V. When the electrode is cycled only to a cutoff voltage of 1.0 V (Figure 4.8(b)), the initial capacity is less, 597 mAh $g^{-1}$, but it is well retained. There are two possible reasons responsible for the capacity fading when the $SnO_2/TiO_2$ electrode is cycled to 1.5 V. First, the nanocomposite is possibly damaged by excessive lithiation/delithiation of the $Li_xTiO_2$. Second, charging the electrode up to 1.5 V, decomposition of the lithium oxide matrix which acts as the buffer to retard the aggregation of tin, could occur resulting in capacity fading.[58] The reversible capacities of the $SnO_2/TiO_2$ nanocomposite electrodes cycled between 50 mV to 1.5 V and between 50 mV to 1.0 V at a 0.2 C rate for 100 cycles are shown in Figure 4.9(a). The 830 mAh $g^{-1}$ initial capacity for cycling to 1.5 V exceeds the 782 mAh $g^{-1}$ theoretical capacity of tin oxide, establishing that not only Sn is lithiated/delithiated, but also $Li_xTiO_2$, consistent with the 1.0 V to 1.5 V shoulder (Figure 4.9(a)). However, the capacity is not well maintained in the initial cycles, dropping to 581

mAh $g^{-1}$ (~380 mAh $g^{-1}$ based on the weight of $SnO_2/TiO_2$) after 25 cycles. In contrast, upon cycling only to 1 V the 597 mAh $g^{-1}$ (~390 mAh $g^{-1}$ based on the weight of $SnO_2/TiO_2$) initial capacity is well maintained, more than 80% of the initial capacity being retained after 100 cycles (Figure 4.9(b)). By deliberately limiting the cycling voltage window to 1 V, the $Li_xTiO_2$ that structurally/mechanically supports the lithium-alloyed/de-alloyed tin is preserved. Although the $SnO_2/TiO_2$ nanocomposite electrode showed low Coulombic efficiency in the first cycle due to the formation of SEI and $Li_2O$, it quickly increased to more than 95% in few cycles, and eventually exceeding 98% (Figure 4.9(c)).

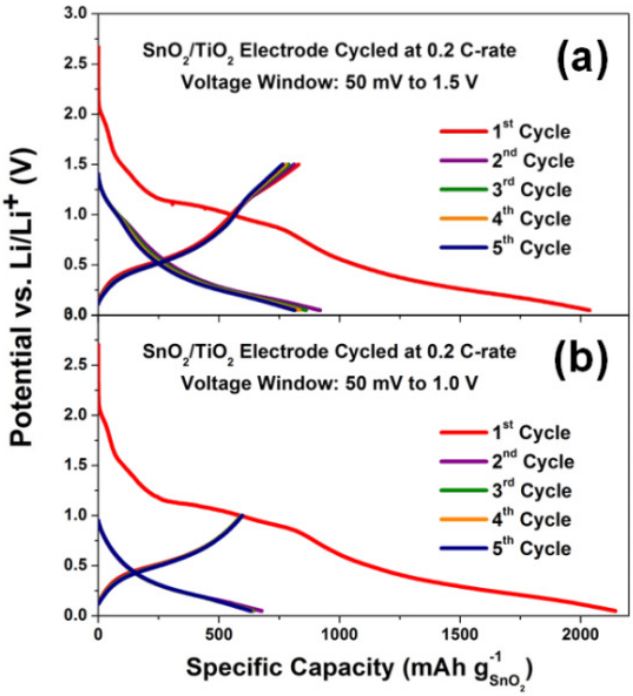


Figure 4.8. Voltage profiles of the $SnO_2/TiO_2$ nanocomposite electrode cycled between (a) 50 mV to 1.5 V and (b) 50 mV to 1.0 V at 0.2 C rate.

The capacity retention of the commercially available $SnO_2$ nanoparticle electrodes were tested under the same conditions as the $SnO_2/TiO_2$ nanocomposite electrodes, the results of which are also shown in Figure 4.9. While the $SnO_2$ NP electrode without $TiO_2$ shows a high initial capacity of 624 mAh $g^{-1}$, it drops to less than 20 mAh $g^{-1}$ within 100 cycles at 0.2 C rate between 50 mV and 1.5 V (Figure 4.9(a)). The reason the $SnO_2$ NP electrode capacity deteriorated rapidly may be attributed to the electrochemical instability of the $Li_2O$ at operating voltages above 1 V, which may correspond to the low Coulombic efficiencies as observed in Figure 4.9(c). We believe the lithium oxide supporting structure deteriorates rapidly when cycled up to 1.5 V and cannot support the tin structure after a few cycles, thus resulting in rapid capacity fading. Compared to the results of the $SnO_2/TiO_2$ electrode cycled up to 1.5 V, the nanocomposite cycling behavior benefits from the support of the titania. By limiting the upper cutoff voltage to 1.0 V instead of 1.5 V with the same 0.2 C rate, the $SnO_2$ NP electrode can maintain a capacity of ~500 mAh $g^{-1}$ up to 50 cycles (Figure 4.9(a)). However, capacity fade was observed for the $SnO_2$ NP electrode after 60 cycles. We believe this implies that even when the upper cutoff voltage is limited to 1.0 V, the decomposition of $Li_2O$ is inhibited but not prevented, which may explain the delayed onset of capacity fading for the $SnO_2$ NP electrode.

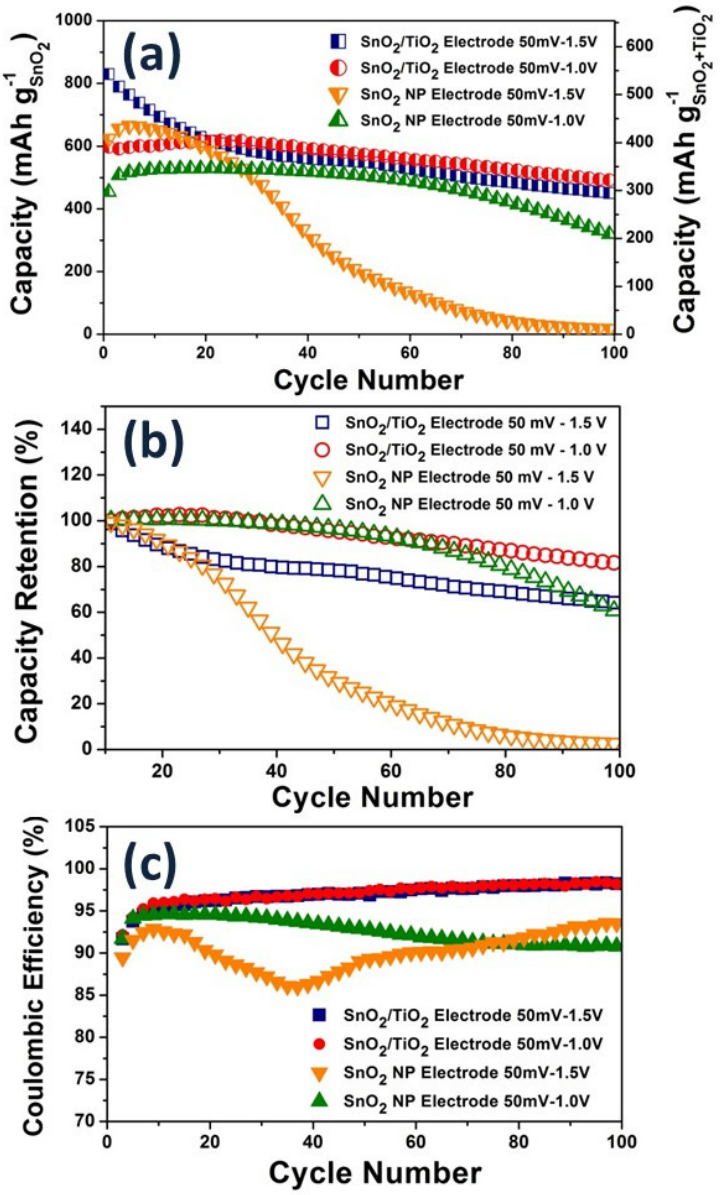


Figure 4.9. (a) Reversible capacities of the $SnO_2/TiO_2$ electrodes and $SnO_2$ NP electrodes cycled at 0.2 C between 50 mV - 1.5 V and 50 mV - 1.0 V. Scales on the left y-axis apply to both the $SnO_2$ NP electrodes and the $SnO_2/TiO_2$ electrodes, while those on the right y-axis apply to the $SnO_2/TiO_2$ electrodes only. (b) Capacity retentions of the $SnO_2/TiO_2$ electrodes and $SnO_2$ NP electrodes. (c) Coulombic efficiencies of the $SnO_2/TiO_2$ electrode and the $SnO_2$ NP electrode cycled at 0.2 C between 50 mV - 1.0 V.

The rate capability of the $SnO_2/TiO_2$ nanocomposite electrode cycled between 50 mV and 1 V was evaluated stepwise by increasing the galvanostatic current from 0.2 C to 5 C (0.2 C, 0.5 C, 1 C, 2 C, 5 C), then returning to 0.2 C. The electrode was cycled at each rate 10 times (Figure 4.10). A reversible capacity of ~600 mAh $g^{-1}$ (~390 mAh $g^{-1}$ based on the weight of $SnO_2/TiO_2$) was obtained at a cycling rate of 0.2 C, and capacities of 570, 540, 470 mAh $g^{-1}$ were observed for rates of 0.5 C, 1C and 2C, respectively. When cycled at a C rate as high as 5 C, the $SnO_2/TiO_2$ electrode showed a stable capacity ~340 mAh $g^{-1}$ based on the mass of tin oxide, or ~220 mAh $g^{-1}$ based on the mass of $SnO_2/TiO_2$. The capacity almost fully returned to the initial ~600 mAh $g^{-1}$ after switching back to a 0.2 C rate. The rate performance of the $SnO_2$ NP electrode (without $TiO_2$) was also measured in the same manner mentioned above, as shown in Figure 4.10. When cycled at low- or medium-C rates, the $SnO_2$ NP electrode exhibited high capacities of 530, 500, 460, 370 mAh $g^{-1}$ for rates of 0.2 C, 0.5 C, 1 C, 2 C, respectively. These specific capacities of the $SnO_2$ NP electrode are higher than that of the $SnO_2/TiO_2$ electrode if the mass of titania is included. Interestingly, when cycled at a rate as high as 5 C, the capacity of the $SnO_2$ NP electrode decreased to 140 mAh $g^{-1}$. This capacity is lower than that of the $SnO_2/TiO_2$ nanocomposite electrode even when the mass of $TiO_2$ is taken into account. Similar to the $SnO_2/TiO_2$ electrode, the capacity of the $SnO_2$ NP electrode is almost fully recovered after switching back to 0.2 C. The capacity recovery of an electrode indicates whether it has been damaged by high current density at high C rates. For the case of our $SnO_2$ and $SnO_2/TiO_2$ nanocomposite electrodes both recover

well after cycling at 5 C as shown in Figure 4.10. While the $SnO_2$ electrode outperforms the $SnO_2/TiO_2$ electrode at lower current densities, the capacity differences for these two electrodes at various C rates are likely due to the rate limitation of the solid state lithium-ion diffusion. The synthesized $SnO_2/TiO_2$ nanocomposite exhibits a smaller average particle size and a larger specific surface area than the commercial $SnO_2$, and these properties can facilitate the Li-ion diffusion process, especially at higher C-rates. Moreover, beyond mechanically supporting the tin matrix, the lithiated $Li_xTiO_2$ is a good lithium ion conductor and the diffusivity of Li-ions increases rapidly in the amorphous $TiO_2$-derived $Li_xTiO_2$ with lithium concentration.[59] The existence of lithiated $Li_xTiO_2$ can also enhance the kinetics of lithium transport in the $TiO_2$ supported $SnO_2$ nanocomposite.

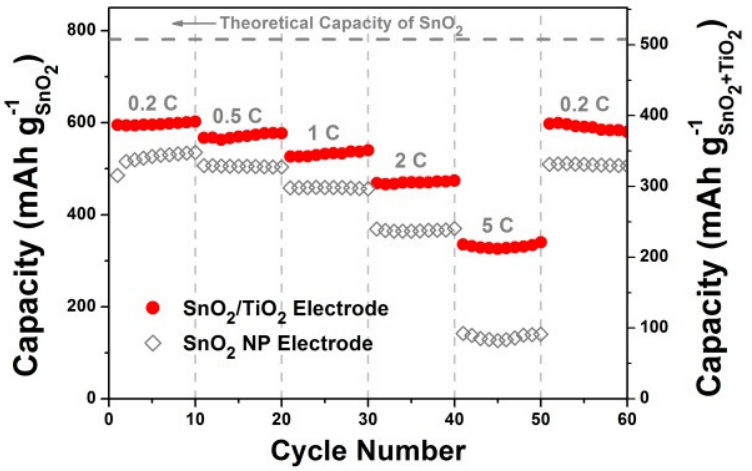


Figure 4.10. Reversible capacities of $SnO_2/TiO_2$ electrode and $SnO_2$ nanoparticle electrode cycled between 50 mV – 1.0 V at various C rates. Scales on the left y-axis apply to both $SnO_2$ NP electrodes and $SnO_2/TiO_2$ electrodes, while those on the right y-axis apply to $SnO_2/TiO_2$ electrodes only.

## CONCLUSIONS

Commercial $SnO_2$ nanoparticles and a $TiO_2$-supported $SnO_2$ nanocomposite formed of equimolar amounts of the Sn and Ti oxides were investigated as anode materials for Li-ion batteries. The electrodes made of the $SnO_2$ nanoparticles show improved cycle stability by limiting the voltage window of the charge/discharge cycles to the range 50 mV - 1.0 V. When cycling within this potential domain, the $SnO_2$ NP electrode can maintain a capacity of ~500 mAh $g^{-1}$ up to 50 cycles at a 0.2 C rate. Although adding $TiO_2$ decreases the overall capacity at low C rates, the $SnO_2/TiO_2$ nanocomposite electrodes exhibit better capacity retention and higher Coulombic efficiency. The $Li_xTiO_2$ formed in the $SnO_2/TiO_2$ composite during the first half-cycle structurally/mechanically supports the electrode and is believed to be the reason for prolonged cyclability. Both the $SnO_2$ NP electrodes and the $TiO_2$-supported-$SnO_2$ electrodes show good cycling stability at various C rates up to 5C. The reversible capacities of the $SnO_2$ NP electrode are higher than that of the $SnO_2/TiO_2$ electrode at C rates from 0.2 C to 2 C when taking into account the additional mass of $TiO_2$. However, the $SnO_2/TiO_2$ electrode shows a higher overall capacity when cycled at 5 C, which is attributed to the small particle size and the $Li^+$ conducting $Li_xTiO_2$ formed in the nanocomposite.

## REFERENCES


1. Armand, M.; Tarascon, J. M., *Nature* **2008,** *451* (7179), 652-657.

2. Ning, G.; Haran, B.; Popov, B. N., *J. Power Sources* **2003,** *117* (1-2), 160-169.

3. Goodenough, J. B.; Kim, Y., *Chem. Mater.* **2010,** *22* (3), 587-603.

4. Manthiram, A., *J. Phys. Chem. Lett.* **2011,** *2* (3), 176-184.

5. Courtney, I. A.; Dahn, J. R., *J. Electrochem. Soc.* **1997,** *144* (9), 2943-2948.

6. Winter, M.; Besenhard, J. O., *Electrochim. Acta* **1999,** *45* (1-2), 31-50.

7. Li, N. C.; Martin, C. R.; Scrosati, B., *Electrochem. Solid-State Lett.* **2000,** *3* (7), 316-318.

8. Besenhard, J. O.; Winter, M., *ChemPhysChem* **2002,** *3* (2), 155-159.

9. Besenhard, J. O.; Yang, J.; Winter, M., *J. Power Sources* **1997,** *68* (1), 87-90.

10. Chao, S. C.; Yen, Y. C.; Song, Y. F.; Chen, Y. M.; Wu, H. C.; Wu, N. L., *Electrochem. Commun.* **2010,** *12* (2), 234-237.

11. Arico, A. S.; Bruce, P.; Scrosati, B.; Tarascon, J. M.; Van Schalkwijk, W., *Nat. Mater.* **2005,** *4* (5), 366-377.

12. Wang, Y.; Cao, G. Z., *Adv. Mater. (Weinheim, Ger.)* **2008,** *20* (12), 2251-2269.

13. Zhu, J. J.; Lu, Z. H.; Aruna, S. T.; Aurbach, D.; Gedanken, A., *Chem. Mater.* **2000,** *12* (9), 2557-2566.

14. Ying, Z.; Wan, Q.; Cao, H.; Song, Z. T.; Feng, S. L., *Appl. Phys. Lett.* **2005,** *87* (11), 113108.

15. Wang, Y.; Lee, J. Y.; Zeng, H. C., *Chem. Mater.* **2005,** *17* (15), 3899-3903.

16. Yuan, L.; Guo, Z. P.; Konstantinov, K.; Liu, H. K.; Dou, S. X., *J. Power Sources* **2006,** *159* (1), 345-348.

17. Liu, J. P.; Li, Y. Y.; Huang, X. T.; Ding, R. M.; Hu, Y. Y.; Jiang, J.; Liao, L., *J. Mater. Chem.* **2009,** *19* (13), 1859-1864.

18. Lou, X. W.; Li, C. M.; Archer, L. A., *Adv. Mater. (Weinheim, Ger.)* **2009,** *21* (24), 2536-+.

19. Liu, J.; Li, W.; Manthiram, A., *Chem. Commun. (Cambridge, U. K.)* **2010,** *46* (9), 1437-1439.

20. Zhao, Y.; Li, J.; Ding, Y.; Guan, L., *RSC Advances* **2011,** *1* (5), 852-856.

21. Chen, F. L.; Shi, Z.; Liu, M. L., *Chem. Commun. (Cambridge, U. K.)* **2000,** (21), 2095-2096.

22. Zhang, J.; Chen, L. B.; Li, C. C.; Wang, T. H., *Appl. Phys. Lett.* **2008,** *93* (26), 264102.

23. Wang, Y. Y.; Hao, Y. J.; Lai, Q. Y.; Lu, J. Z.; Chen, Y. D.; Ji, X. Y., *Ionics* **2008,** *14* (1), 85-88.

24. Li, C.; Wei, W.; Fang, S. M.; Wang, H. X.; Zhang, Y.; Gui, Y. H.; Chen, R. F., *J. Power Sources* **2010,** *195* (9), 2939-2944.

25. Matsumura, T.; Sonoyama, N.; Kanno, R.; Takano, M., *Solid State Ionics* **2003,** *158* (3-4), 253-260.

26. Kim, D. W.; Hwang, I. S.; Kwon, S. J.; Kang, H. Y.; Park, K. S.; Choi, Y. J.; Choi, K. J.; Park, J. G., *Nano Lett.* **2007,** *7* (10), 3041-3045.

27. Kulova, T. L.; Skundin, A. M.; Roginskaya, Y. E.; Chibirova, F. K., *Russ. J. Electrochem.* **2004,** *40* (4), 432-439.

28. Vassiliev, S. Y.; Yusipovich, A. I.; Rogynskaya, Y. E.; Chibirova, F. K.; Skundin, A. M.; Kulova, T. L., *J. Solid State Electrochem.* **2005,** *9* (10), 698-705.

29. Roginskaya, Y. E.; Chibirova, F. K.; Kulova, T. L.; Skundin, A. M., *Russ. J. Electrochem.* **2006,** *42* (4), 355-362.

30. Issac, I.; Scheuermann, M.; Becker, S. M.; Bardaji, E. G.; Adelhelm, C.; Wang, D.; Kubel, C.; Indris, S., *J. Power Sources* **2011,** *196* (22), 9689-9695.

31. Fu, Z. W.; Qin, Q. Z., *J. Phys. Chem. B* **2000,** *104* (23), 5505-5510.

32. Wagemaker, M.; Van Der Ven, A.; Morgan, D.; Ceder, G.; Mulder, F. M.; Kearley, G. J., *Chem. Phys.* **2005,** *317* (2-3), 130-136.

33. Cantao, M. P.; Cisneros, J. I.; Torresi, R. M., *J. Phys. Chem.* **1994,** *98* (18), 4865-4869.

34. Hu, Y. S.; Kienle, L.; Guo, Y. G.; Maier, J., *Adv. Mater. (Weinheim, Ger.)* **2006,** *18* (11), 1421-1426.

35. Kubiak, P.; Pfanzelt, M.; Geserick, J.; Hormann, U.; Husing, N.; Kaiser, U.; Wohlfahrt-Mehrens, M., *J. Power Sources* **2009,** *194* (2), 1099-1104.

36. Exnar, I.; Kavan, L.; Huang, S. Y.; Gratzel, M., *J. Power Sources* **1997,** *68* (2), 720-722.

37. Jiang, C. H.; Wei, M. D.; Qi, Z. M.; Kudo, T.; Honma, I.; Zhou, H. S., *J. Power Sources* **2007,** *166* (1), 239-243.

38. Borghols, W. J. H.; Wagemaker, M.; Lafont, U.; Kelder, E. M.; Mulder, F. M., *Chem. Mater.* **2008,** *20* (9), 2949-2955.

39. Chen, J. S.; Lou, X. W., *Electrochem. Commun.* **2009,** *11* (12), 2332-2335.

40. Wagemaker, M.; Borghols, W. J. H.; Mulder, F. M., *J. Am. Chem. Soc.* **2007,** *129* (14), 4323-4327.

41. Wu, M. S.; Wang, M. J.; Jow, J. J.; Yang, W. D.; Hsieh, C. Y.; Tsai, H. M., *J. Power Sources* **2008,** *185* (2), 1420-1424.

42. Koudriachova, M. V.; Harrison, N. M.; de Leeuw, S. W., *Phys. Rev. Lett.* **2001,** *86* (7), 1275-1278.

43. Koudriachova, M. V.; Harrison, N. M.; de Leeuw, S. W., *Physical Review B* **2002,** *65* (23), 235423.

44. Wagemaker, M.; Kentgens, A. P. M.; Mulder, F. M., *Nature* **2002,** *418* (6896), 397-399.

45. Wagemaker, M.; van de Krol, R.; Kentgens, A. P. M.; van Well, A. A.; Mulder, F. M., *J. Am. Chem. Soc.* **2001,** *123* (46), 11454-11461.

46. Fang, H. T.; Liu, M.; Wang, D. W.; Sun, T.; Guan, D. S.; Li, F.; Zhou, J. G.; Sham, T. K.; Cheng, H. M., *Nanotechnology* **2009,** *20* (22), 225701.

47. Uchiyama, H.; Imai, H., *Chem. Commun. (Cambridge, U. K.)* **2005,** (48), 6014-6016.

48. Naidu, H. P.; Virkar, A. V., *J. Am. Ceram. Soc.* **1998,** *81* (8), 2176-2180.

49. Guo, X. Z.; Kang, Y. F.; Wang, L. W.; Liu, X. H.; Zhang, J.; Yang, T. L.; Wu, S. H.; Wang, S. R., *Mater. Sci. Eng., C* **2011,** *31* (7), 1369-1373.

50. Li, H.; Zhang, W.; Pan, W., *J. Am. Ceram. Soc.* **2011,** *94* (10), 3184-3187.

51. Yu, J. G.; Yu, H. G.; Cheng, B.; Zhao, X. J.; Yu, J. C.; Ho, W. K., *J. Phys. Chem. B* **2003,** *107* (50), 13871-13879.

52. Barton, T. J.; Bull, L. M.; Klemperer, W. G.; Loy, D. A.; McEnaney, B.; Misono, M.; Monson, P. A.; Pez, G.; Scherer, G. W.; Vartuli, J. C.; Yaghi, O. M., *Chem. Mater.* **1999,** *11* (10), 2633-2656.

53. Pavelko, R. G.; Vasil'ev, A. A.; Sevast'yanov, V. G.; Gispert-Guirado, F.; Vilanova, X.; Kuznetsov, N. T., *Russ. J. Electrochem.* **2009,** *45* (4), 470-475.

54. Demir-Cakan, R.; Hu, Y. S.; Antonietti, M.; Maier, J.; Titirici, M. M., *Chem. Mater.* **2008,** *20* (4), 1227-1229.

55. Ho, W. H.; Liu, H. C.; Chen, H. C.; Yen, S. K., *Surf. Coat. Technol.* **2007,** *201* (16-17), 7100-7106.

56. Yim, C. H.; Baranova, E. A.; Courtel, F. M.; Abu-Lebdeh, Y.; Davidson, I. J., *J. Power Sources* **2011,** *196* (22), 9731-9736.

57. Lin, Y. M.; Abel, P. R.; Flaherty, D. W.; Wu, J.; Stevenson, K. J.; Heller, A.; Mullins, C. B., *J. Phys. Chem. C* **2011,** *115* (5), 2585-2591.

58. Mohamedi, M.; Lee, S. J.; Takahashi, D.; Nishizawa, M.; Itoh, T.; Uchida, I., *Electrochim. Acta* **2001,** *46* (8), 1161-1168.

59. Yildirim, H.; Greeley, J.; Sankaranarayanan, S., *J. Phys. Chem. C* **2011,** *115* (31), 15661-15673.

# Chapter 5: High Performance Silicon Nanoparticle Anode in Fluoroethylene Carbonate-Based Electrolyte for Li-ion Batteries

## INTRODUCTION

For utility, electrodes to be used in lithium ion batteries must simultaneously meet criteria of manufacturability, safety, high capacity, high Coulombic efficiency, high power density and long cycle life.[1, 2] One of the promising alternatives for the conventional graphite anode is silicon because of its high capacity for lithium storage: its maximum theoretical capacity of 3579 mAh $g^{-1}$, corresponding to the formation of a $Li_{15}Si_4$ alloy upon full lithiation at room temperature,[3] is nearly tenfold higher than that of graphite. However, the lithiation/de-lithiation of Si is associated with a large volume change that typically results in unacceptable rapid capacity fade within a few cycles.[4] It is well known that nanostructured electrode materials not only better accommodate large strains but also provide short diffusion distances in the small grains necessary for rapid $Li^+$ insertion/de-insertion.[5] Hence, electrode performance has been improved with nanostructured Si for a range of morphologies.[6-11] Most of this previous research has been conducted employing an ethylene carbonate (EC)-based electrolyte containing lithium salt, with the chemical structure shown in Illustration 1(a). Fluoroethylene carbonate (FEC, 4-fluoro-1,3-dioxolan-2-one), with the chemical structure shown in Illustration 1(b), was first reported as an alternative solvent for Li-ion batteries with graphite anodes by McMillan and coworkers.[12]

Thus far, only Si thin film anodes have been investigated with electrolytes containing FEC. Choi and coworkers were the first to use FEC-added electrolytes with silicon thin film electrodes. They reported that a low concentration of FEC (3%) added to an EC-based electrolyte resulted in a smoother solid electrolyte interface (SEI) layer on the silicon film.[13] Nakai and coworkers further investigated the formation of SEI on Si thin film electrodes in a FEC-based electrolyte (EC was totally replaced by FEC).[14] They concluded that the FEC-derived SEI on the Si thin film was thinner and more stable than the EC-derived SEI, thus improving the capacity retention of the Si anode. Recently, Aurbach and coworkers reported positive effects from FEC as a co-solvent for thin film Si-nanowire anodes which were prepared by a vapour-liquid-solid (VLS) method.[15]

These previous works all showed the attractive merits of using FEC for Si thin film electrodes, however, these anodes are not well suited for industrial scale-up. Electrodes for commercial lithium ion batteries are commonly manufactured by casting a slurry comprised of active material, conductive additive, and polymer binder onto a current collector, rather than the thin film electrodes described above. Herein, we report on tests of silicon nanoparticle (SiNP) anodes made by a conventional slurry casting process matched with FEC-based electrolytes. Our results using the FEC:DMC electrolyte have practical importance for the engineering of stable silicon based anodes with improved performance at high charge rates but also have scientific value when combined with consideration of the poor cycling performance we report for the nominally identical anodes tested using EC-based electrolytes: an expanded or revised model for

understanding capacity fade may be needed to explain how the same nanosized active material either sustains stable cycling performance or rapidly deteriorates during identical testing regimes. We hope the results presented here will advance the progress of research on the electrolyte in silicon based anodes for Li-ion batteries.

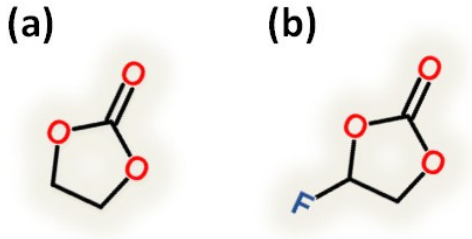


Illustration 5.1. Chemical structures of (a) ethylene carbonate (EC) and (b) fluoroethylene carbonate (FEC).

## EXPERIMENTAL METHODS

The silicon nanoparticles (average particle size ≤ 50 nm, 98%) in this study were purchased from Alfa Aesar and used without any further treatment. The SiNP electrodes were prepared by forming an aqueous slurry of the SiNP (40 wt%), conductive carbon black (Super P-Li, Timcal) (40 wt %) and 90 kDa CMC (Aldrich) (20 wt %) in a stirring tube (ST-20, IKA). The slurry was cast onto a Cu foil using an automatic applicator and a notch bar with 50 μm clearance and then dried in a vacuum oven at 120°C for 12 hrs. The final film thicknesses are around 12 μm. Typically, the mass loading of materials on Cu foil is ~500 μg/cm$^2$, which contains ~200 μg/cm$^2$ of Si. After cooling to room

temperature, the cast film was punched into disks, which constituted the working electrodes of 2032 type coin cells. The cells, assembled in an argon filled glove-box, had lithium foil counter/reference electrodes, polypropylene (Celgard 2400, Celgard) membrane separators and used for the electrolyte either: i) 1M $LiPF_6$ in EC/DMC (1:1 wt/wt) (LP30, EMD Chemicals), ii) 1M $LiPF_6$ (≥ 99.99%, Aldrich) in FEC (> 99%, Solvay Chemicals)/DMC (≥ 99%, Aldrich) (1:1 wt/wt), or iii) 1M $LiPF_6$ in FEC/EC/DMC (1:1:2 wt/wt/wt). The cells were galvanostatically cycled at room temperature using a multichannel battery test system (BT 2043, Arbin), all the specific capacities are calculated based on the weight of silicon. An electrochemical analyzer (CHI 604D, CH Instruments) was used for EIS, carried out over a wide frequency range from 100 kHz to 0.01 Hz with an ac perturbation voltage of 5 mV.

## RESULTS AND DISCUSSION

A scanning transmission electron microscopy analysis (Figure 5.1) of the commercial Si powder shows that it has a bimodal particle size distribution in which the majority of the particles are smaller than 200 nm (Figure 5.2). In order to evaluate the electrochemical performance, electrodes made of SiNPs with sodium carboxymethyl cellulose (CMC) as the binder and carbon black as the conductive additive on Cu-substrates were incorporated into coin cells. Cells were made with: (i) 1M $LiPF_6$ in EC/DMC (1:1), a commercially available EC-based electrolyte for current Li-ion

batteries, (ii) 1M $LiPF_6$ in FEC/DMC (1:1), a home made FEC-based electrolyte, or (iii) 1M $LiPF_6$ in FEC/EC/DMC (1:1:2). The cells were cycled between 10 mV and 1 V *versus* $Li/Li^+$ at a 0.2 C rate (716 $mA/g_{Si}$), corresponding to a rate of fully charging or discharging the cell within 5 hours.

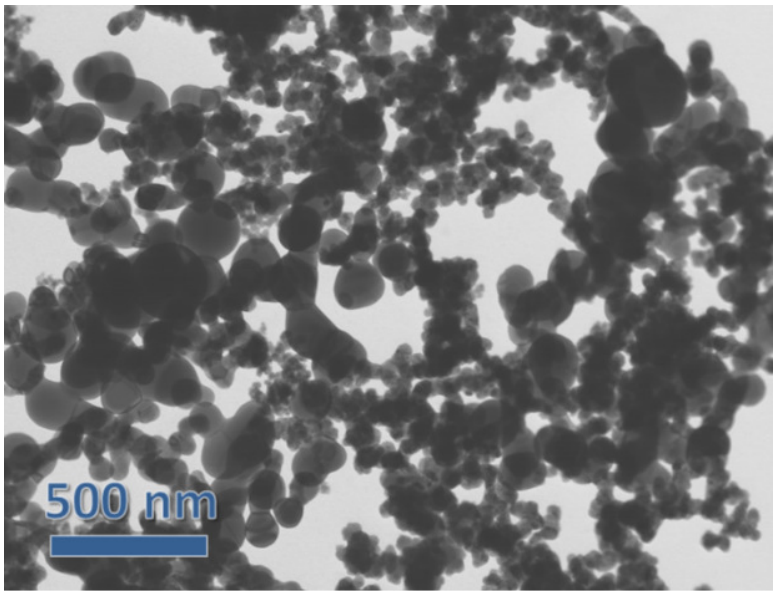


Figure 5.1. STEM image of Si nanoparticles.

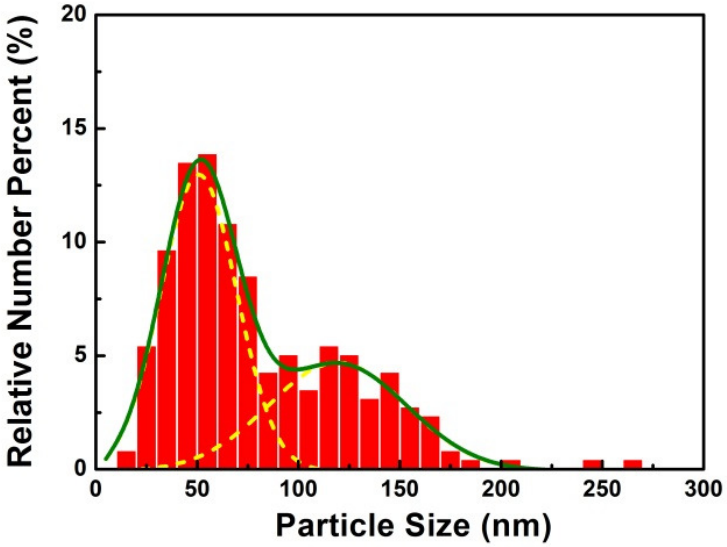


Figure 5.2. Particle size distribution of Si nanoparticles by measuring the sizes of the 250 particles in the STEM image shown above.

Figure 5.3 shows the performance of the cells made with the EC-based (50% EC) and the FEC-based (50% FEC) electrolytes when fully charged/discharged (the detailed voltage profiles can be seen in Figure 5.4(a) and 5.4(b)). Reversible capacities for SiNP electrodes in EC and FEC-based electrolytes cycled at 0.2 C rate up to 100 cycles are shown in Figure 5.3(a). The reversible capacity of the SiNP electrode in the EC-based electrolyte is 2353 mAh $g^{-1}$ for the initial cycle, which gradually increases to a peak value of ~2800 mAh $g^{-1}$ after 10 cycles and then continuously decreases to 1157 mAh $g^{-1}$ by the 100th cycle. The SiNP electrode in the FEC-based electrolyte has an initial capacity of 2142 mAh $g^{-1}$, slightly lower than that of the same electrode in the EC-based electrolyte. Similarly to the electrode in the EC-based electrolyte, the electrode cycled in the FEC-

based electrolyte reaches a maximum capacity of ~2800 mAh $g^{-1}$ after a few cycles. However, unlike the electrode in the EC-based electrolyte, the SiNP electrode in the FEC-based electrolyte demonstrates significantly improved stability during prolonged lithium insertion/de-insertion cycling, with 95% of the reversible capacity being retained from the 10th cycle to the 100th cycle (Figure 5.3(b)). The Coulombic efficiencies in the first cycle are 80% for the electrode in the EC-based electrolyte and 72% for the electrode in the FEC-based electrolyte (Figure 5.3(c)). However, the SiNP electrode in the EC-based electrolyte shows lower efficiencies than with the FEC-based electrolyte after the second cycle. The low Coulombic efficiency (~ 95%) after ~30 cycles for the electrode in the EC-based electrolyte can be correlated to the pronounced capacity fading between the 20th and the 50th cycles. Although the first cycle efficiency of the SiNP electrode in the FEC-based electrolyte is lower, it quickly increases to 98% within 10 cycles and eventually exceeds 99%. The high Coulombic effiency of the SiNP electrode in the FEC-based electrolyte results in significantly improved electrochemical stability for lithium storage when compared to the same electrode in an EC-based electrolyte.

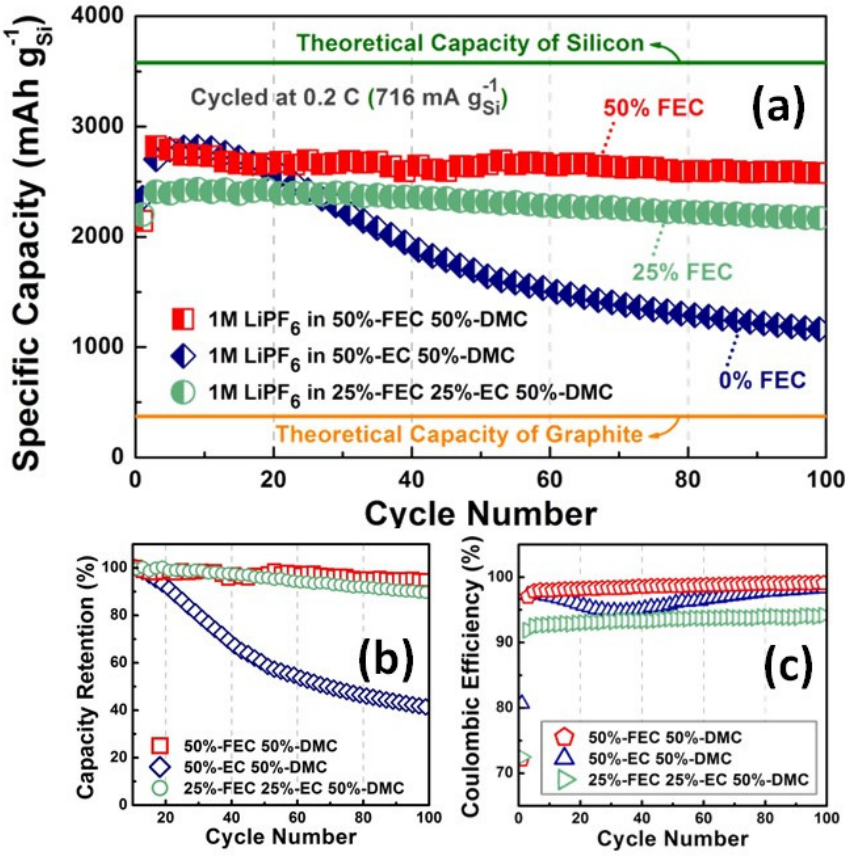


Figure 5.3. (a) Reversible capacity (b) capacity retention and (c) Coulombic efficiency of SiNP electrode cycled in various electrolytes at a 0.2 C rate (716 mA $g_{Si}^{-1}$). (The mass loading of Si is ~200 μg $cm^{-2}$)

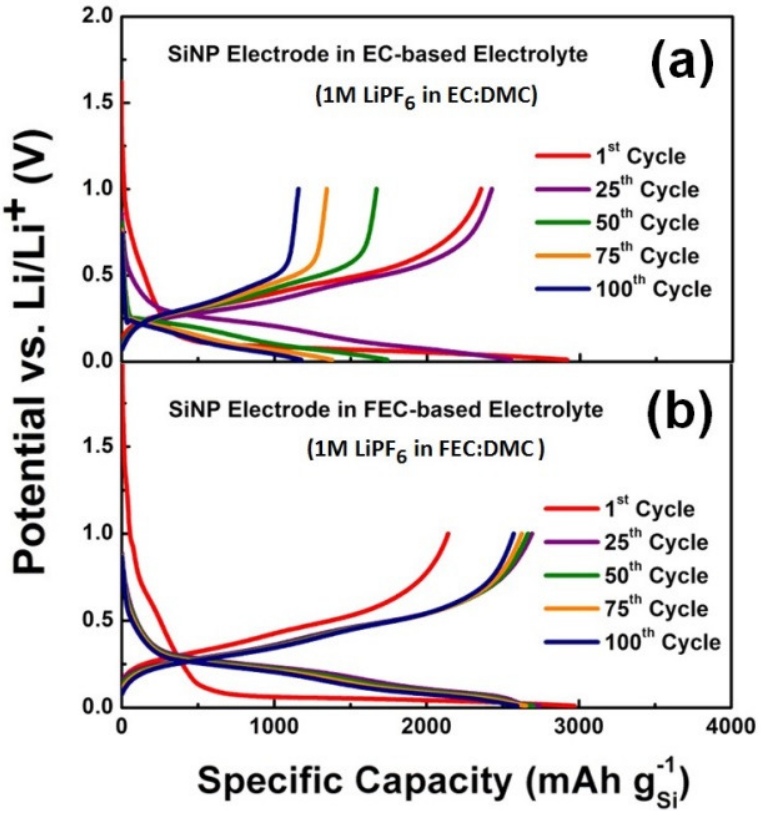


Figure 5.4. Charge and discharge curves of SiNP electrodes cycled in (a) EC-based electrolyte and (b) FEC-based electrolyte at a 0.2 C rate (716 mA $g_{Si}^{-1}$).

SiNP electrodes were tested in 1M $LiPF_6$ in FEC/EC/DMC (25%/25%/50%), as the results in Figure 5.3 show. The reversible capacities are lower in 25% FEC compared to the results in 50% FEC, but still show much better stability than in the 50% EC. Interestingly, the Coulombic efficiency of SiNP electrodes in 25% FEC was the lowest among these three electrolytes. Besides being used as a primary cosolvent, FEC was also tested as an additive in the EC-based electrolyte. Figure 5.5 shows the result of the SiNP electrode cycled in 1M $LiPF_6$ in EC/DMC with and without 3% FEC at a

charge/discharge rate of C/10. Although adding a small amount of FEC (3%) into the EC-based electrolyte can slightly improve the cycling stability, the capacities still dropped rapidly after 20 cycles. Combined with the cycling test data shown above, these results suggest that the more FEC present (up to 50%) in the electrolyte, the better the cycling performance.

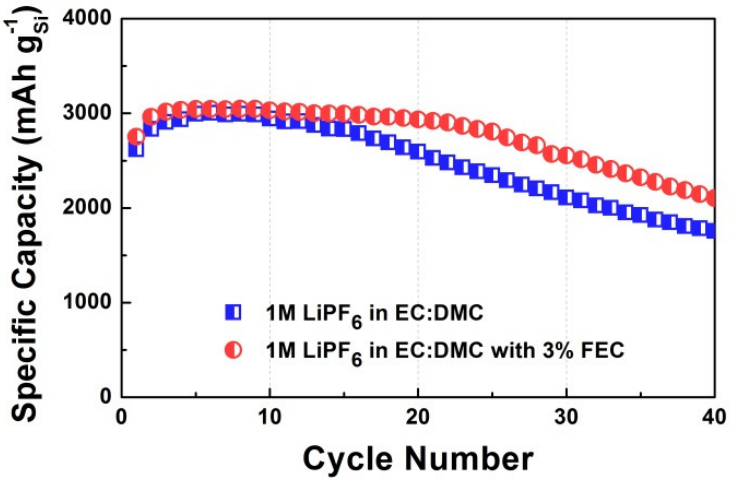


Figure 5.5. Reversible capacity vs. cycle number of SiNP electrdes cycled in 1M $LiPF_6$ in EC/DMC with and without 3wt% FEC at a rate of C/10 (357.9 mA $g_{Si}^{-1}$).

Electrochemical impedance spectroscopy (EIS) of the SiNP electrode tested in the EC-based electrolyte after 100 cycles at a 0.2 C rate are presented in a Nyquist plot (Figure 5.6(a)). The plot consists of two semicircles in the high frequency region which can be attributed to charge transfer processes, and a sloped line in the low frequency region that is related to the mass transfer of lithium ions. The first small semicircle

represents the contribution of the charge transfer between the electrolyte and the SEI (as indicated by the green arrow in the inset of Figure 5.6(a)), and the second semicircle represents the charge transfer between the SEI and the silicon. The electrochemical system can be modeled by an equivalent circuit as shown in Figure 5.6(b),[16] where $R_{\Omega}$ is the ohmic resistance, $R_{SEI}$ is the charge resistance between the SEI layer and the electrolyte, $R_{CT}$ is the charge transfer resistance between the SEI and Si, $C_{SEI}$ is the capacitance of the SEI, $C_{dl}$ is the double layer capacitance on Si, and $Z_W$ is the Warburg impedance describing the solid state diffusion of $Li^+$ in the electrode. The charge transfer resistances are determined to be 8 Ω ($R_{SEI}$) and 57 Ω ($R_{CT}$) for the electrode cycled in the EC-based electrolyte. The Nyquist plot of the SiNP electrode cycled in the FEC-based electrolyte at the same rate and cycle numbers is also shown in Figure 5.6(a). Unlike the electrode cycled in the EC-based electrolyte, only a single semicircle can be observed for the SiNP electrode cycled in the FEC-based electrolyte. The absence of the first semicircle implies that the resistance through the FEC-derived SEI is negligible, consistent with the thin SEI formation on thin film Si in a FEC-based electrolyte reported by Nakai and coworkers.[14] The SiNP electrode cycled in the FEC-based electrolyte has a charge transfer resistance ($R_{CT}$) of ~34 Ω, smaller than the electrode cycled in the EC-based electrolyte, indicative of the ease of interfacial charge transfer between Si and the FEC-derived SEI.

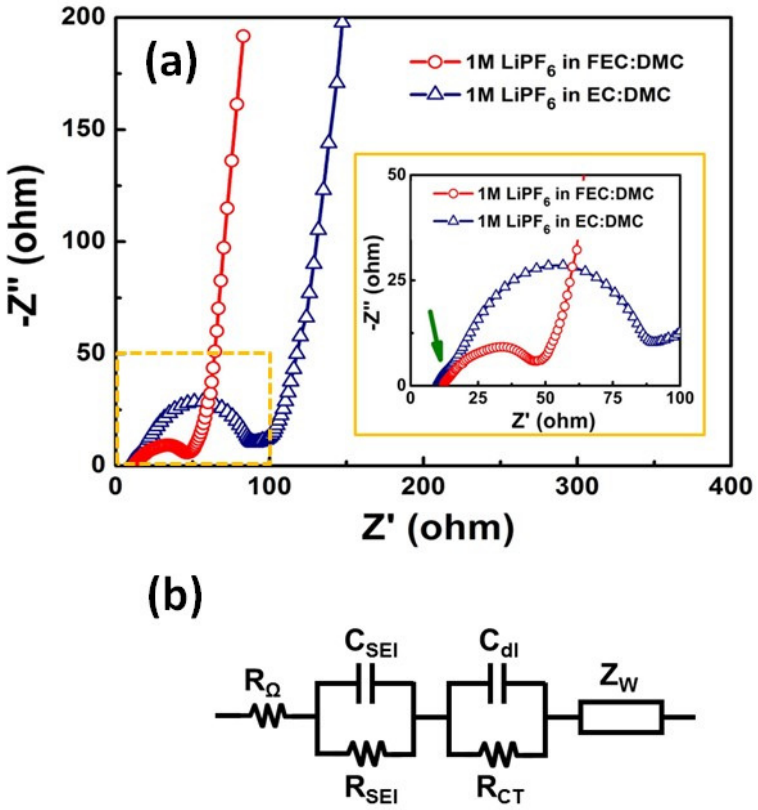


Figure 5.6. (a) Electrochemical impedance spectroscopy of SiNP electrodes cycled in EC and FEC-based electrolyte after 100 cycles with an inset that shows a zoom view of Z' between 0 and 100 ohms. (The green arrow indicates a small semicircle contributed by the SEI derived from the EC-based electrolyte) (b) Equivalent circuit.

In order to further investigate the high rate performance of the SiNP electrodes, galvanostatic tests were carried out by applying a higher current density onto electrodes within the same voltage window (10 mV to 1 V) in the EC and the FEC-based electrolyte, separately. Cells were initially tested for 10 cycles at 0.2 C (716 mA $g^{-1}$) followed by continuous charging/discharging at 1 C (3.6 A $g^{-1}$) up to 250 cycles, and their

reversible capacity for lithium storage as a function of cycle number is shown in Figure 5.7. The SiNP electrodes in both electrolytes show capacities of ~2800 mAh $g^{-1}$ at their 10th cycle tested at 0.2 C, consistent with the previous results in this chapter. After switching to a 1 C rate, the capacity of the electrode in the EC-based electrolyte monotonically decays to ~600 mAh $g^{-1}$ after 250 cycles. However, the capacity of the SiNP electrode in the FEC-based electrolyte continued increasing from the 30th cycle to the 160th cycle before attaining stable reversible capacity. A linear fit from cycle 160 to cycle 250 shows that the rate of capacity fade is only ~0.57 mAh $g^{-1}$ per cycle, or ~0.03% per cycle. The Coulombic efficiencies for these cycles are in a range from 99.4% to 99.6%. At the end of the cycling test, a reversible capacity of more than 2000 mAh $g^{-1}$ is achieved for the SiNP electrode cycled at 1 C within the FEC-based electrolyte.

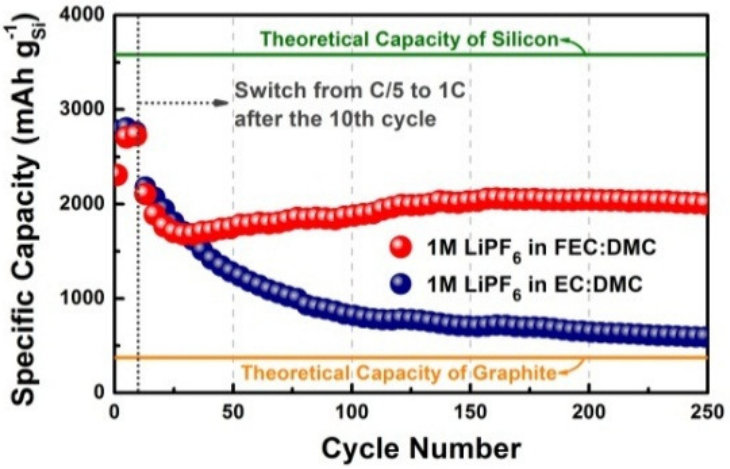


Figure 5.7. Reversible capacity ***vs.*** cycle number of SiNP electrodes cycled in EC and FEC-based electrolyte at C/5 (716 mA $g_{Si}^{-1}$) for the initial 10 cycles and switched to 1C (3.6 A $g_{Si}^{-1}$) for subsequent cycles.

## CONCLUSIONS

In conclusion, slurry cast silicon nanoparticle-based electrodes matched with an electrolyte containing fluorinated ethylene carbonate were electrochemically tested in coin cells vs. $Li/Li^+$. The SiNP electrode in the FEC-based electrolyte outperforms the electrode in the conventional EC-based electrolyte in terms of capacity retention and Coulombic efficiency. The improved performance of the SiNP electrode in the FEC-based electrolyte is attributed to the better properties of the FEC-derived solid electrolyte interface on the surface of the silicon.

## REFERENCES


1. Chalk, S. G.; Miller, J. E., *J. Power Sources* **2006,** *159*, 73-80.

2. Armand, M.; Tarascon, J. M., *Nature* **2008,** *451* (7179), 652-657.

3. Obrovac, M. N.; Christensen, L., *Electrochemical and Solid State Letters* **2004,** *7* (5), A93-A96.

4. Kasavajjula, U.; Wang, C. S.; Appleby, A. J., *J. Power Sources* **2007,** *163* (2), 1003-1039.

5. Arico, A. S.; Bruce, P.; Scrosati, B.; Tarascon, J. M.; Van Schalkwijk, W., *Nat. Mater.* **2005,** *4* (5), 366-377.

6. Chan, C. K.; Peng, H. L.; Liu, G.; McIlwrath, K.; Zhang, X. F.; Huggins, R. A.; Cui, Y., *Nat. Nanotechnol.* **2008,** *3* (1), 31-35.

7. Chan, C. K.; Patel, R. N.; O'Connell, M. J.; Korgel, B. A.; Cui, Y., *ACS Nano* **2010,** *4* (3), 1443-1450.

8. Li, H.; Huang, X. J.; Chen, L. Q.; Wu, Z. G.; Liang, Y., *Electrochemical and Solid State Letters* **1999,** *2* (11), 547-549.

9. Graetz, J.; Ahn, C. C.; Yazami, R.; Fultz, B., *Electrochemical and Solid State Letters* **2003,** *6* (9), A194-A197.

10. Fleischauer, M. D.; Li, J.; Brett, M. J., *J. Electrochem. Soc.* **2009,** *156* (1), A33-A36.

11. Abel, P. R.; Lin, Y.-M.; Celio, H.; Heller, A.; Mullins, C. B., *ACS Nano* **2012,** *6* (3), 2506-2516.

12. McMillan, R.; Slegr, H.; Shu, Z. X.; Wang, W. D., *J. Power Sources* **1999,** *81*, 20-26.

13. Choi, N. S.; Yew, K. H.; Lee, K. Y.; Sung, M.; Kim, H.; Kim, S. S., *J. Power Sources* **2006,** *161* (2), 1254-1259.

14. Nakai, H.; Kubota, T.; Kita, A.; Kawashima, A., *J. Electrochem. Soc.* **2011,** *158* (7), A798-A801.

15. Etacheri, V.; Haik, O.; Goffer, Y.; Roberts, G. A.; Stefan, I. C.; Fasching, R.; Aurbach, D., *Langmuir* **2012,** *28* (1), 965-976.

16. Yamada, Y.; Iriyama, Y.; Abe, T.; Ogumi, Z., *J. Electrochem. Soc.* **2010,** *157* (1), A26-A30.

# Chapter 6: Storage of Lithium in Hydrothermally Synthesized $GeO_2$ Nanoparticles

## INTRODUCTION

Lithium-ion batteries are used in consumer electronics, electric vehicles and aircraft.[1, 2] Most of the commercially available Li-ion batteries have graphite based anodes, with a theoretical capacity of 372 mAh $g^{-1}$ (837 mAh $cm^{-3}$). Because the intercalation potential of lithium in graphite is only ~0.1 V higher than the redox potential of $Li/Li^+$, unintentional electroplating of lithium dendrites have frequently led to internal shorting and overheating, an unacceptable hazard, especially in aircraft and electric vehicles where the batteries are large.[2, 3] More safe anode materials such as lithium-alloys,[4-7] conversion oxides,[8-11] and Li-intercalation compounds[12-14] have been investigated. Binary lithium alloys, for example, with Si, Ge or Sn, are of particular interest because of their high lithium storage capacity compared to graphite. Germanium is an especially interesting candidate not only because of its high theoretical capacity (1384 mAh $g^{-1}$), but also because of the high $Li^+$ diffusivity in Ge, which is two orders of magnitude higher than in silicon at ambient temperature.[15] However, the cost of pure germanium limits its use. Germanium dioxide ($GeO_2$), is less expensive than elemental Ge, which has been widely used as a polymerization catalyst.[16] $GeO_2$ is also a component of optical fibers and waveguides where it modulates the index of refraction.[17-19] At this time, there are only a few reports of studies of $GeO_2$ related to electrochemical energy

storage applications. Brousse and coworkers considered germania as an anode material of Li-ion batteries,[20] showing that $GeO_2$ is irreversibly reduced by Li to form Ge and $Li_2O$:

$$GeO_2 + 4Li \rightarrow Ge + 2Li_2O \quad (1)$$

And the elemental Ge further reversibly alloys Li according to the reaction:

$$Ge + 4.4Li \rightleftarrows Li_{4.4}Ge \quad (2)$$

Based on Reactions (1) and (2), $GeO_2$ has a theoretical gravimetric capacity of 1100 mAh $g^{-1}$ and a volumetric capacity of 4653 mAh $cm^{-3}$,[21] much higher than that of graphite. However, the practical capacity of $GeO_2$ is not well-retained upon cycling. The reversible capacity of the slurry based $GeO_2$ electrode of Brousse et al. dropped from 740 mAh $g^{-1}$ to 225 mAh $g^{-1}$ after only 10 cycles.[20] The fast capacity loss has been attributed to the ~230% volume change during lithium insertion/de-insertion.[15] Superplastically deforming nanostructured materials readily sustains strains associated with such large volume-changes.[22, 23] A recent study of $GeO_2$ thin film electrodes reported by Lu and coworkers suggested that the cycling stability depends strongly on the grain size of $GeO_2$.[21] In their study, a thin $GeO_2$ film with 10 nm grains showed better cycling stability, retaining 89% of its initial capacity after 100 cycles. A similar thin film but with 100 nm grains only retained 53% of its initial capacity after 100 cycles. The studies of Brousse et al. and of Lu et al. suggested that the cycling stability could be further improved by engineering the size and morphology of the $GeO_2$ nanocrystals.

Thus far the electrolyte used in studies of the $GeO_2$ anode has been ethylene carbonate (EC) containing a lithium salt, which has proven to be an effective electrolyte with graphite anodes for Li-ion batteries.[24] Fluoroethylene carbonate (FEC) as an additive or as a co-solvent in the electrolyte improves the electrochemical performance of several anode materials, including conventional graphite,[25] silicon[26-30] and germanium anodes.[31] The FEC-derived solid electrolyte interface (SEI) layer on the surface of the silicon electrode was reported to have better thermal stability[32] and electrochemical properties.[26-28]

Here we build upon these previous research efforts in improving the performance of germanium oxide anodes for lithium ion batteries. We report the synthesis of amorphous $GeO_2$ nanoparticles with tunable sizes by a surfactant-assisted hydrothermal process. We note that recently Cui et al. reported amorphous material has more favorable kinetics and fracture behavior than crystalline material when reacting with lithium.[33] The electrochemical properties of the prepared germania nanoparticles were investigated in two electrolytes: first, in the conventional EC-based electrolyte and then also in a FEC-based electrolyte. Compared to when using EC, the performance of the $GeO_2$ electrode was much improved during prolonged cycling in the electrolyte containing FEC as a co-solvent, with more than 96% of the maximum capacity being retained after 500 cycles. The electrode structures after being cycled in the different electrolytes were observed by top-view scanning electron microscopy (SEM) and cross-sectional transmission electron microscopy (TEM).

## EXPERIMENTAL METHODS

*Materials and Synthesis:* Germanium tetrachloride ($GeCl_4$, 99.99%, Gelest) was dissolved in ethanol to form a 0.5M solution. The surfactant, 1,2-diaminopropane (1,2-DP, $C_3H_{10}N_2$, 99%, Alfa Aesar) was added to 20ml of the solution at weight ratios of $GeCl_4$/1,2-DP of 1/4, 1/8, and 1/16. The $GeCl_4$/ethanol/1,2-DP solution was then added dropwise to 20 ml vigorously stirred deionized water. The mixture was continuously stirred for 45 min then transferred into a Teflon-lined stainless steel autoclave and heated to 140°C, 180°C or 220°C, for 12 hours. After the mixture cooled to room temperature the precipitate was collected by centrifugation, washed twice with ethanol and dried under vacuum at 80 °C. The synthesis was also performed without adding any 1,2-DP.

*Physical Characterization:* The synthesized $GeO_2$ powders were characterized by scanning electron microscopy (SEM) using a Hitachi S-5500 electron microscope equipped with a Bruker EDS Quantax 4010 energy dispersive X-ray spectroscopic (EDS) detector for elemental analysis. X-ray diffraction (XRD) patterns were obtained using a Bruker-Nonius D8 Advance powder diffractometer with Cu Kα radiation.

*Electrochemical Measurements:* The $GeO_2$ nanoparticles prepared from $GeCl_4$/1,2-DP of 1/8 at 180°C were tested in lithium cells. The electrodes were prepared by mixing the $GeO_2$ (60 wt %) with conductive carbon black (Super P-Li, Timcal) (20 wt %) and with 450 kDa polyacrylic acid (PAA, Aldrich) (20 wt %) using ethanol as the dispersing medium. The mixture was slurry-cast on a 10 μm thick Cu foil using an

automatic applicator and a notch bar with 100 μm clearance, then dried under vacuum at 120 C for 12 hrs. Next, the as-prepared $GeO_2$ slurry-cast film was punched into disk working electrodes. The mass loading of $GeO_2$ was ~ 500 μg $cm^{-2}$. The electrochemical measurements were carried out using stainless steel 2032 type coin cells with Li foil counter/reference electrode. The cells were assembled in an argon-atmosphere glovebox. Cells were made with either (i) 1M LiPF6 in EC/DMC (1:1) (LP30, EMD Chemicals), a commercially available EC-based electrolyte used in Li-ion batteries, or (ii) 1M LiPF6 (≥99.99%, Aldrich) in FEC (>99%, Solvay Chemicals)/DMC (≥99%, Aldrich) (1:1), a home-made FEC-based electrolyte. A polypropylene membrane (Celgard 2400, Celgard) was used as a separator. The assembled coin cells were galvanostatically cycled at room temperature using a multichannel battery test system (BT 2143, Arbin) between 10 mV and 1 V. An electrochemical analyzer (CHI 604D, CH Instruments) was used for electrode impedance spectroscopy (EIS), carried out over a wide frequency range from 100 kHz to 0.01 Hz with an ac perturbation voltage of 5 mV.

*Electrode Characterization:* The $GeO_2$ electrodes were observed by SEM before and after cycling. Coin cells were disassembled in the glovebox and the cycled electrodes were soaked in DMC for 24 hours to remove the residual electrolyte before SEM imaging. Transmission electron microscopy (TEM) images were acquired using a FEI Tecnai Spirit BioTWIN TEM operated at 80kV. To prepare the TEM specimen, part of the cycled electrode was embedded into an epoxy resin and sectioned with an ultramicrotome using a diamond knife (35° Ultra, DiATOME).

## RESULTS AND DISCUSSION

The hydrothermal syntheses were carried out using germanium tetrachloride ($GeCl_4$) as the precursor, with and without the surfactant 1,2-diaminopropane (1,2-DP). Previously, 1,2-DP has been shown to be an effective surfactant for preparing metal oxides.[34] A series of reactions were conducted to investigate the effects of reaction temperature and surfactant concentration on the morphology of $GeO_2$, which are summarized in Table 6.1. The morphology of each sample was characterized by SEM. It was found that the use of the 1,2-DP surfactant enabled us to modify the dimension and morphology of the $GeO_2$ particles. In the absence of the surfactant, denoted as Sample A, the $GeO_2$ particles synthesized at 180°C had a micrometric cubic structure of side length ~3 micrometers (Figure 6.1(a)). A significant portion of these particles agglomerated into large clusters that exceeded 10 micrometers (Figure 6.2). Their size and agglomeration made these $GeO_2$ microcubes poor candidates for lithium anodes. In contrast, the $GeO_2$ particles that were hydrothermally synthesized in the presence of the surfactant ($GeCl_4$/1,2-DP: 1/8 (wt/wt)) at the same reaction temperature of 180°C, denoted as Sample B, were much smaller in size and with an amorphous, cylinder type morphology (Figure 6.1(b)). Their diameters were typically of 50 to 200 nm. Although some agglomeration was still observed (Figure 6.1(b)), the overall particle sizes were still very small (< 300 nm) compared to the sample prepared without adding surfactant. During the hydrothermal reaction, $GeO_2$ is formed by the hydrolysis of germanium tetrachloride. In the presence of the 1,2-DP surfactant, it works as a ligand to hinder the growth of

germanium oxide, and thus resulted in the formation of nanoparticles. Energy dispersive X-ray spectroscopy (EDS) was used for elemental distribution mapping of Samples A and B (Figure 6.3 and 6.4), and showed a uniform distribution of germanium and oxygen in both samples.

Table 6.1. Synthesis conditions of $GeO_2$ by hydrothermal reaction.

| Sample | Temperature (°C) | $GeCl_4$/1,2-DP (wt/wt) |
|---|---|---|
| A | 180 | 1/0 |
| B | 180 | 1/8 |
| C | 180 | 1/4 |
| D | 180 | 1/16 |
| E | 140 | 1/8 |
| F | 220 | 1/8 |

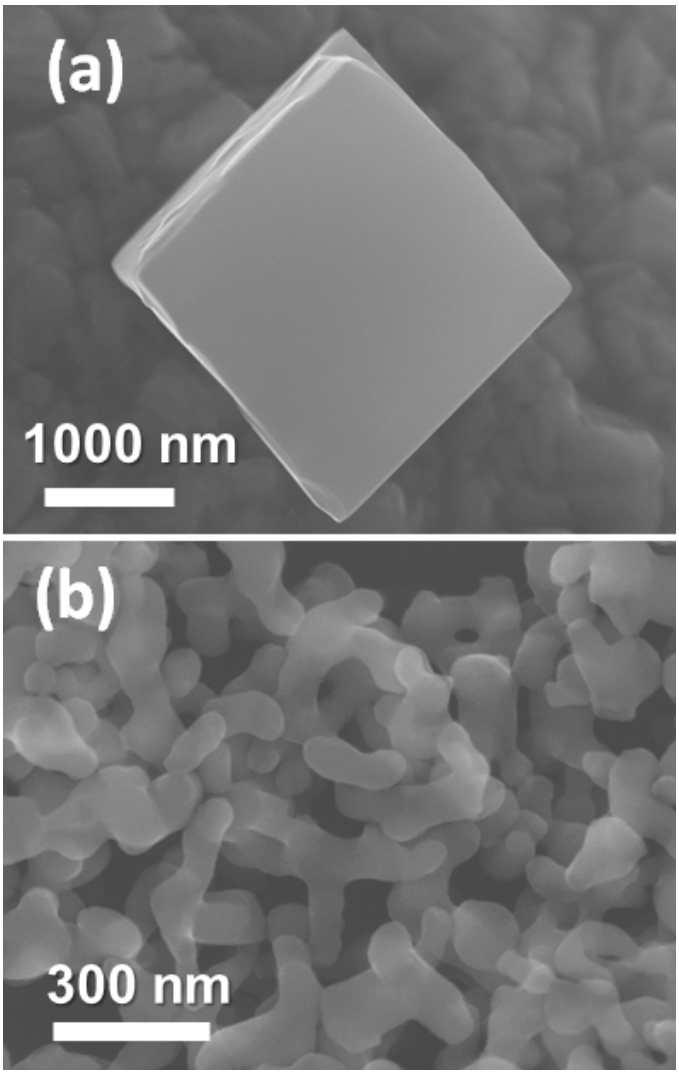


Figure 6.1. SEM of $GeO_2$ the prepared (a) without surfactant (Sample A) and (b) with 1,2-diaminopropane as the surfactant (Sample B).

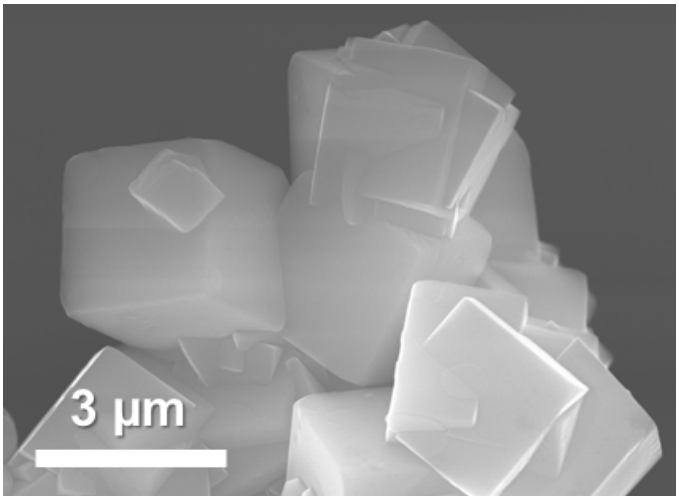


Figure 6.2. SEM image of $GeO_2$ cube clusters prepared by hydrothermal reaction without surfactant.

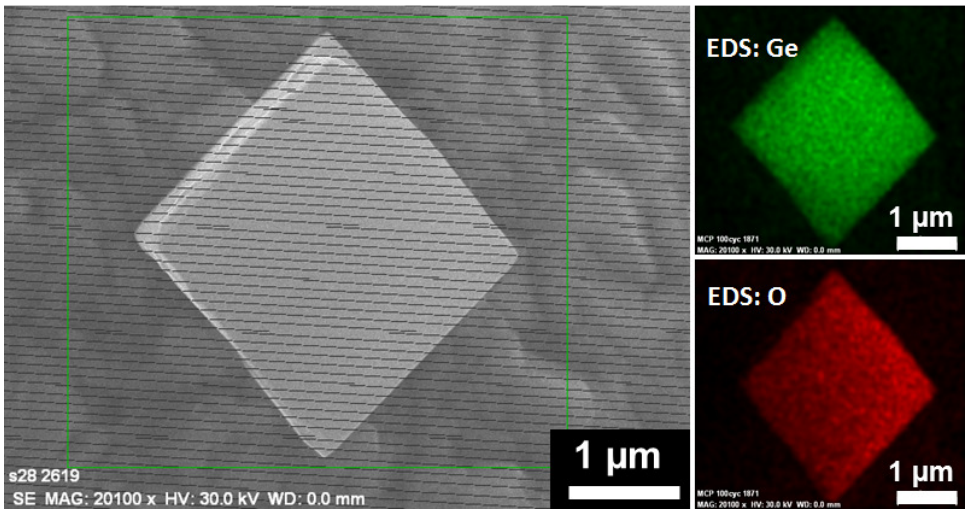


Figure 6.3. SEM image and EDS mapping of $GeO_2$ prepared by hydrothermal reaction without surfactant (Sample A).

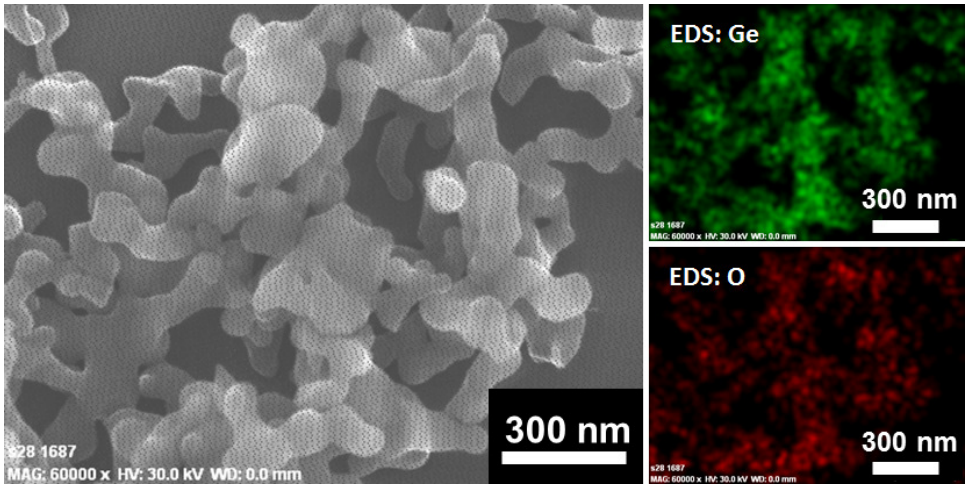


Figure 6.4. SEM image and EDS mapping of $GeO_2$ prepared by hydrothermal reaction with 1,2-diaminopropane. (Sample B)

Figure 6.5 shows the X-ray diffraction (XRD) patterns of the $GeO_2$ powder synthesized with and without surfactant (Samples A and B). It is apparent that in the absence of surfactant, the prepared microcubes (Sample A) are well crystallized, with all the peaks indexed to the hexagonal structure of $GeO_2$ (JCPDS pattern no. 00-036-1463). In contrast, the $GeO_2$ nanoparticles prepared with surfactant (Sample B) appear to be amorphous without any clear XRD peaks. The 1,2-DP surfactant plays a critical role in inhibiting the crystal growth of $GeO_2$, resulting in amorphous nanoparticles which lack long range order.

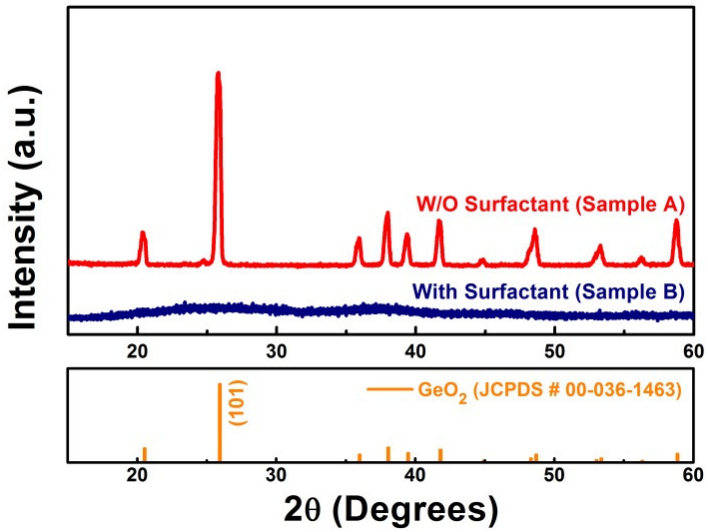


Figure 6.5. X-ray powder diffraction patterns of the $GeO_2$ prepared with and without surfactant.

Figure 6.6 shows the SEM images of $GeO_2$ powders prepared with varying ratios of precursor/surfactant ($GeCl_4$/1,2-DP (wt/wt)) from 1/4, 1/8 to 1/16 (Figure 6.6(a), (b) and (c), respectively), at a fixed reaction temperature of 180°C. When the $GeCl_4$/1,2-DP ratio was 1/4, submicron particles ranging from 200 to 600 nm in diameter were produced (Figure 6.6(a)). Their sizes decreased to 50-200 nm upon reducing the ratio of $GeCl_4$/1,2-DP to 1/8. Further reducing the ratio of $GeCl_4$/1,2-DP to 1/16 resulted in even smaller particles, ranging in size from 30 to 120 nm. There was a clear trend in the $GeO_2$ particles becoming finer when more surfactant was present during the hydrothermal reaction.

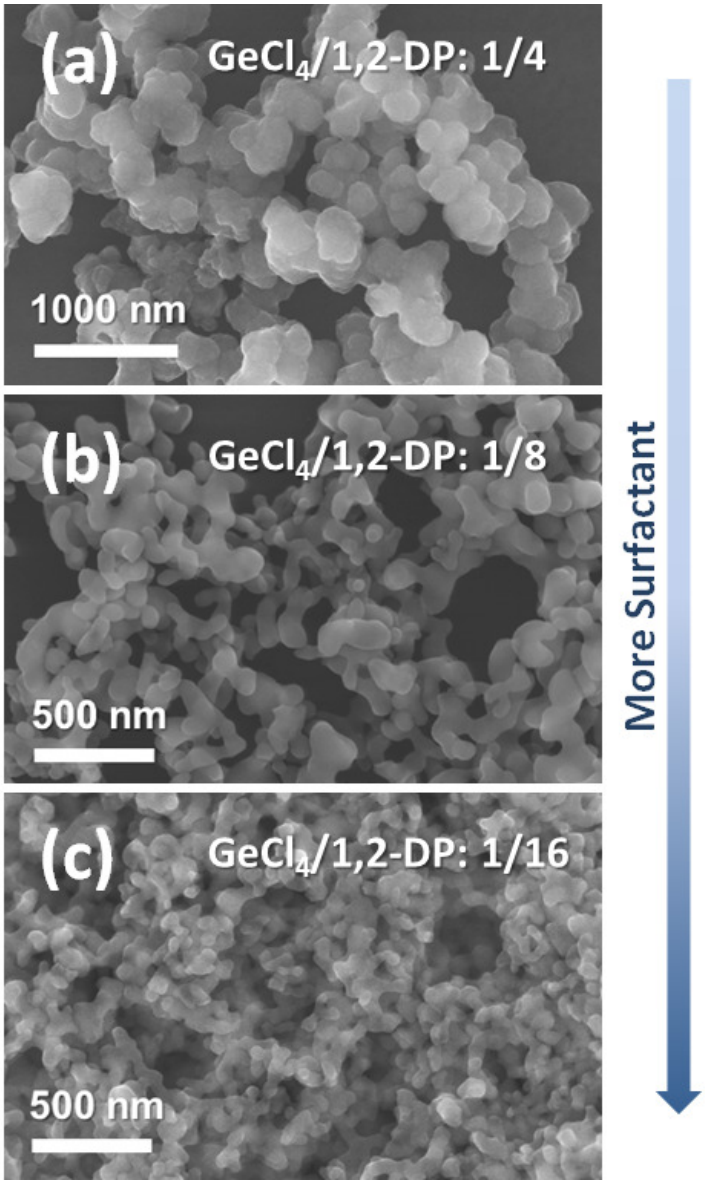


Figure 6.6. SEM images of $GeO_2$ particles prepared with different ratios of $GeCl_4$/1,2-diaminopropane: (a) 1/4 (Sample C) (b)1/8 (Sample B) and (c)1/16 (Sample D).

The influence of the reaction temperature on the synthesis of the $GeO_2$ particles was next investigated by changing the reaction tempeature (140°C, 180°C and 220°C), while keeping the ratio of $GeCl_4$/1,2-DP at 1/8. The precursor did not react fully when the reaction was carried out at 140°C (Figure 6.7), indicating that a higher temperature was required for the reaction to proceed. However, the micron size $GeO_2$ particles obtained at 220°C showed that crystal growth was excessively promoted at the higher temperatures (Figure S4c in the Supporting Information). It was found that 180°C was the optimum temperature for the preparation of $GeO_2$ nanoparticles (Figure 6.7(b)).

In order to evaluate the electrochemical performance of the prepared $GeO_2$ nanoparticles, Sample B (see Figure 6.1(b)) was tested as a candidate anode material for rechargeable lithium batteries. The electrodes were prepared by a slurry casting method; the electrochemical tests were performed using a metallic Li counter/reference electrode in 2032 type coin cells. Cells were made with either: (i) 1M $LiPF_6$ in EC/DMC, a commercially available EC-based electrolyte used in Li-ion batteries, or (ii) 1M $LiPF_6$ in FEC/DMC, a FEC-based electrolyte.

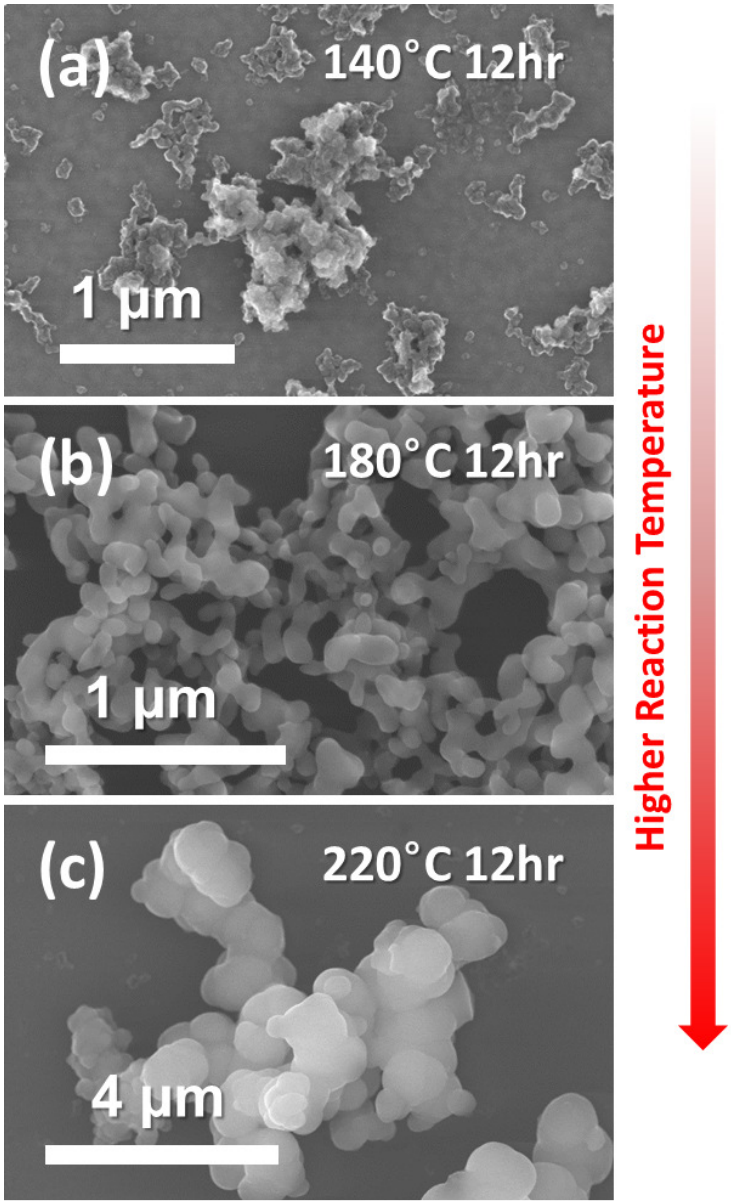


Figure 6.7. SEM images of $GeO_2$ synthesized at various temperatures: (a) 140°C (Sample E),(b) 180°C (Sample B) and (c) 220°C (Sample F) for 12 hours ($GeCl_4$/1,2-DP: 1/8 for all three samples).

The reversible capacities of the $GeO_2$ electrodes cycled in EC and FEC-based electrolytes at a 0.2 C (220 mA $g^{-1}$) rate up to 500 cycles are shown in Figure 6.8 (their voltage profiles and differential capacity plots for cycles 1, 50, 100, 200, 300 and 500 can be found in Figures 6.9 and 6.10). The broad features in the differential capacity plots of the first and subsequent cycles reflect lithium insertion/de-insertion in an amorphous material. In the initial half-cycle starting from the open circuit potential (OCV) for both cells, lithium first reduces the $GeO_2$ to Ge and then alloys Ge to form Li-Ge alloys. These reactions were accompanied by formation of $Li_2O$ and the solid electrolyte interface (SEI), which result in a large irreversible capacity.[20, 21] The low initial Coulombic efficiency (~20%) of the $GeO_2$ nanoparticles is a hurdle for practical applications where the anode is paired with a cathode with a limited amount of lithium. However, it could be overcome by adding extra sacrificial lithium to the anode to improve the initial efficiency.[35-37] Although the first cycle efficiency of the SiNP electrode is low, in both the EC- and the FEC-based electrolyte, it quickly increases to above 97% in 10 cycles. The average Coulombic efficiency of the $GeO_2$ electrode in the FEC-based electrolyte from the 10th cycle to the 500th cycle was 99.0%, 0.5% higher than that of the electrode in the EC-based electrolyte.

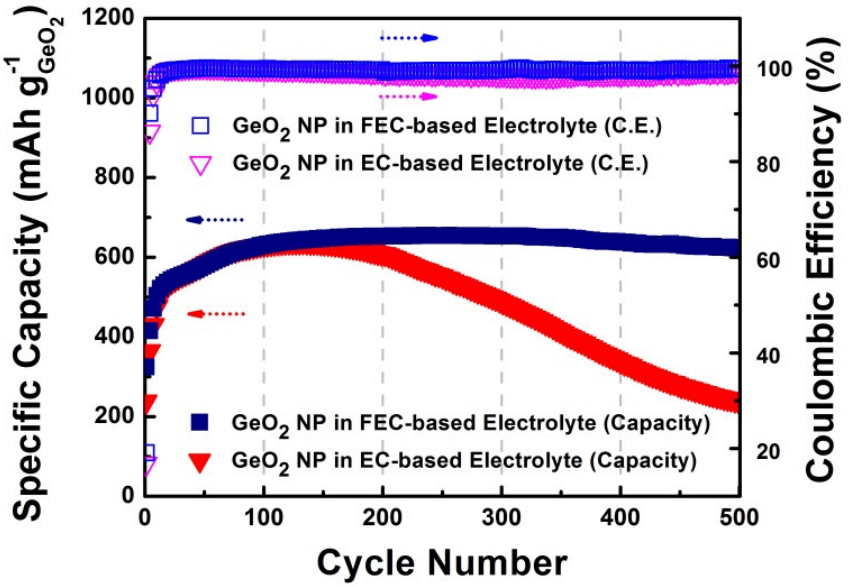


Figure 6.8. Reversible capacities and Coulombic efficiencies of $GeO_2$ nanoparticle electrodes cycled at 0.2 C rate (220 mA $g^{-1}$) in FEC and EC-based electrolytes.

The $GeO_2$ electrodes cycled in the EC-based and the FEC-based electrolytes each reached their maximum capacity of ~640 mAh $g^{-1}$ after 150 cycles. However, the capacity of the $GeO_2$ electrode in the EC-based electrolyte decreased progressively after 150 cycles, dropping to 37% of its maximum capacity after 500 cycles. Even though the $Li_2O$ matrix formed in the first cycle could stabilize the electrode in subsequent cycles, it tended to decompose in the EC-based electrolyte after prolonged cycling,[38] which may explain the delayed onset of capacity fading in the EC-based electrolyte. In contrast, the $GeO_2$ electrode in the FEC-based electrolyte was stable after extensive lithium

insertion/de-insertion cycling, with more than 96% of the reversible capacity being retained from the 150th cycle to the 500th cycle.

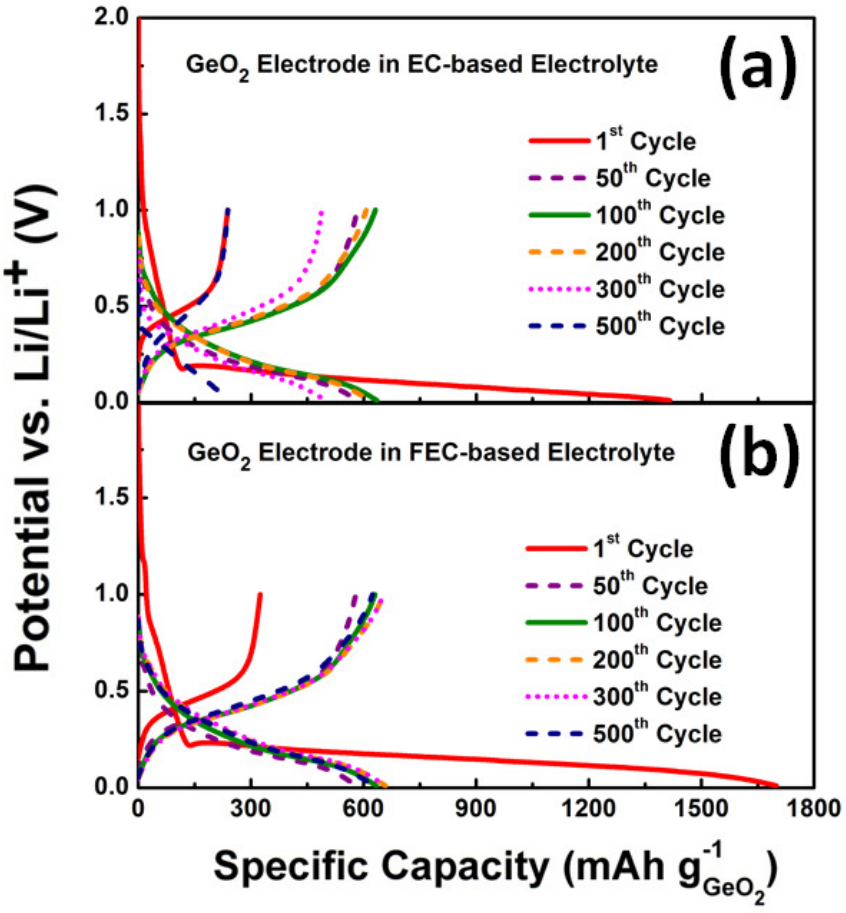


Figure 6.9. Charge and discharge curves of $GeO_2$ nanoparticle electrodes cycled in (a) EC-based electrolyte and (b) FEC-based electrolyte at a 0.2 C rate (220 mA $g^{-1}$).

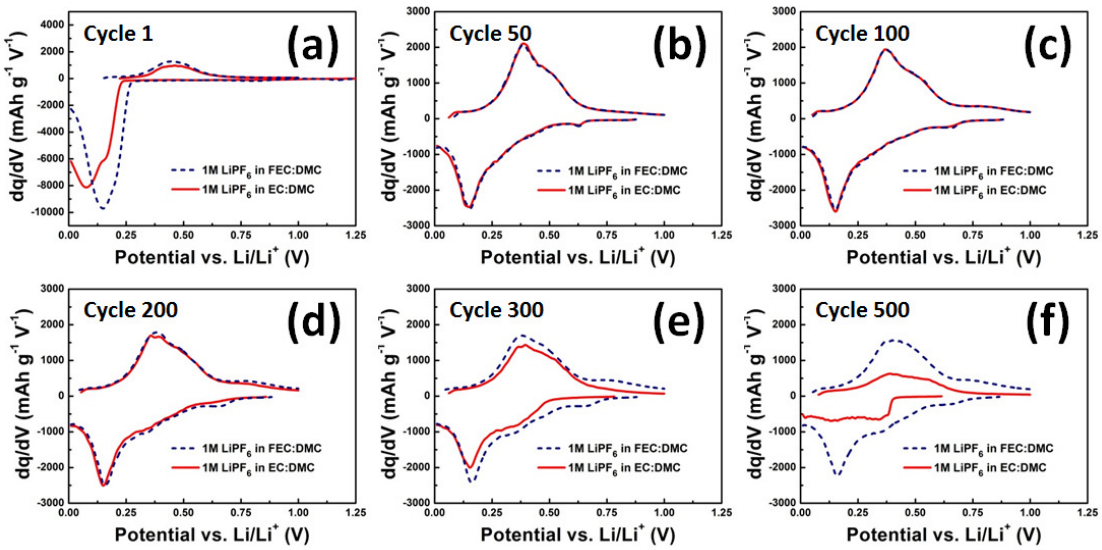


Figure 6.10. Differential capacity plots of $GeO_2$ electrodes in EC-based electrolyte and in FEC-based electrolyte for cycles (a) 1, (b) 50, (c) 100, (d) 200, (e) 300 and (f) 500.

To examine the effect of the two electrolytes on the morphology of the $GeO_2$, the electrodes were investigated by electron microscopy before and after cycling. The SEM image obtained from a pristine $GeO_2$ nanoparticle electrode is presented in Figure 6.11. The pristine electrode is uniformly and closely packed with two types of particles, namely, $GeO_2$ nanoparticles of 50-200 nm (Sample B), and conductive carbon black ~ 40 nm in size. The cycled electrodes were removed from the coin cell in the glovebox, cleaned with dimethyl carbonate (DMC), and then examined by SEM and TEM in their fully-delithiated state. The SEM images of the $GeO_2$ nanoparticle electrodes cycled 500 times at 0.2 C the in FEC-based electrolyte and in the EC-based electrolyte show very

different morphology. Compared to a pristine electrode, the electrode cycled in the FEC-based electrolyte still appears to be closely packed, with a smooth layer covering the surface (Figure 6.12(a)). This layer is most likely mainly composed of $Li_2O$ rather than SEI, because the thickness of the FEC-derived SEI has been reported to be only on the order of 30 nm,[39] which would not be enough to fill the gap between particles. However, the $Li_2O$ layer was not observed in the electrode cycled 500 times in the EC-based electrolyte (Figure 6.12(b)). Also, many cracks were found on the electrode surface and a large amount of material had detached from the electrode, possibly because of decomposition of $Li_2O$ during long cycling in the EC-based electrolyte. Based on this *ex-situ* SEM study, the $Li_2O$ and the SEI formed in the initial cycles were better-preserved in the FEC-based electrolyte but not in the EC-based electrolyte, resulting in the higher Coulombic efficiency and improved stability of the electrodes in the FEC-based electrolyte for prolonged cycles.

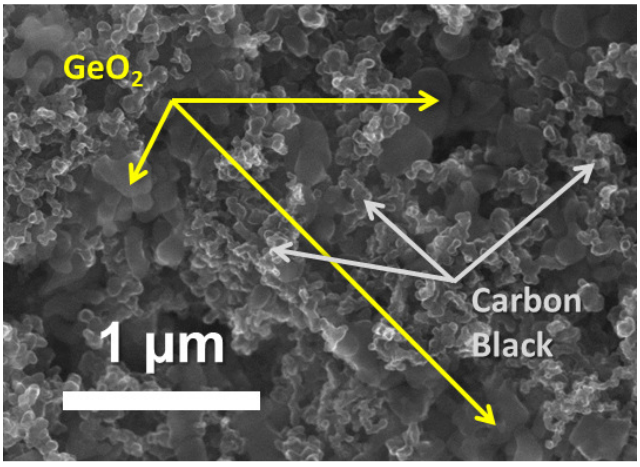


Figure 6.11. SEM image of a pristine $GeO_2$ nanoparticles electrode.

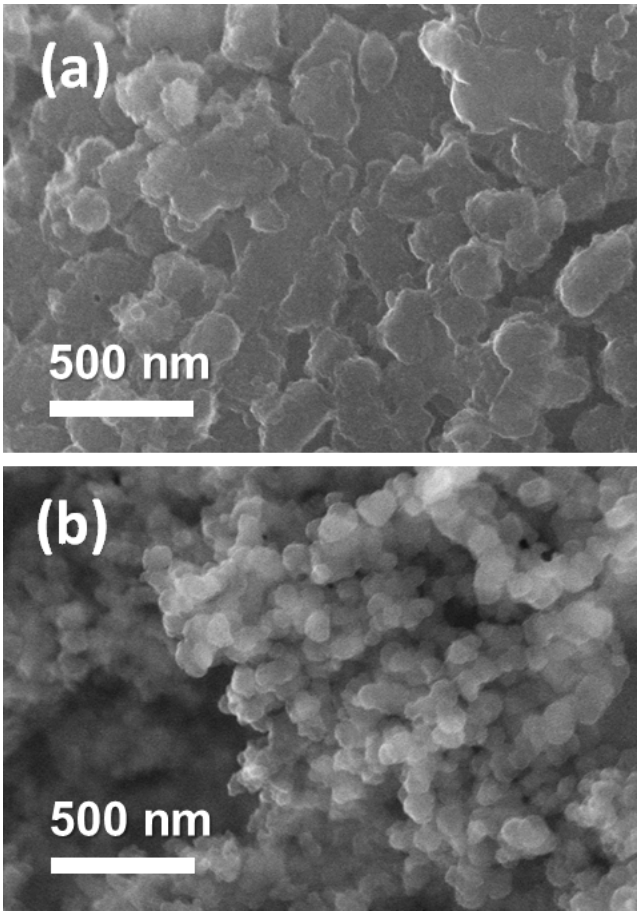


Figure 6.12. SEM images of $GeO_2$ electrodes cycled in (a) FEC-based electrolyte and (b) EC-based electrolyte after 500 cycles.

Using cross-sectional TEM, the structure beneath the surface of the electrode cycled 500 times at 0.2 C in the FEC-based electrolyte is shown in Figure 6.13. The black arrow in Figure 6.13(a) indicates the carbon black, which is lighter in color because of its relatively low density. The darker particles, indicated by the white arrow in Figure 6.13(a), are germanium nanoclusters resulting from the reaction between lithium and

$GeO_2$ during the initial cycle. After cycling in the FEC-based electrolyte, the Ge seemed to remain intact in the SEM image of Figure 6.12(a), the internal structure of the germanium was actually pulverized into small debris as shown in Figure 6.13(a). This shows that the pulverization of the active materials is also happened in the electrolyte containing FEC. Much of the Ge debris was found to be distributed within a continuous $Li_2O$ phase (Figure 6.13(b)). Although the germanium particles were broken into small pieces, they were still electrically connected to the electrode when the FEC-based electrolyte was used.

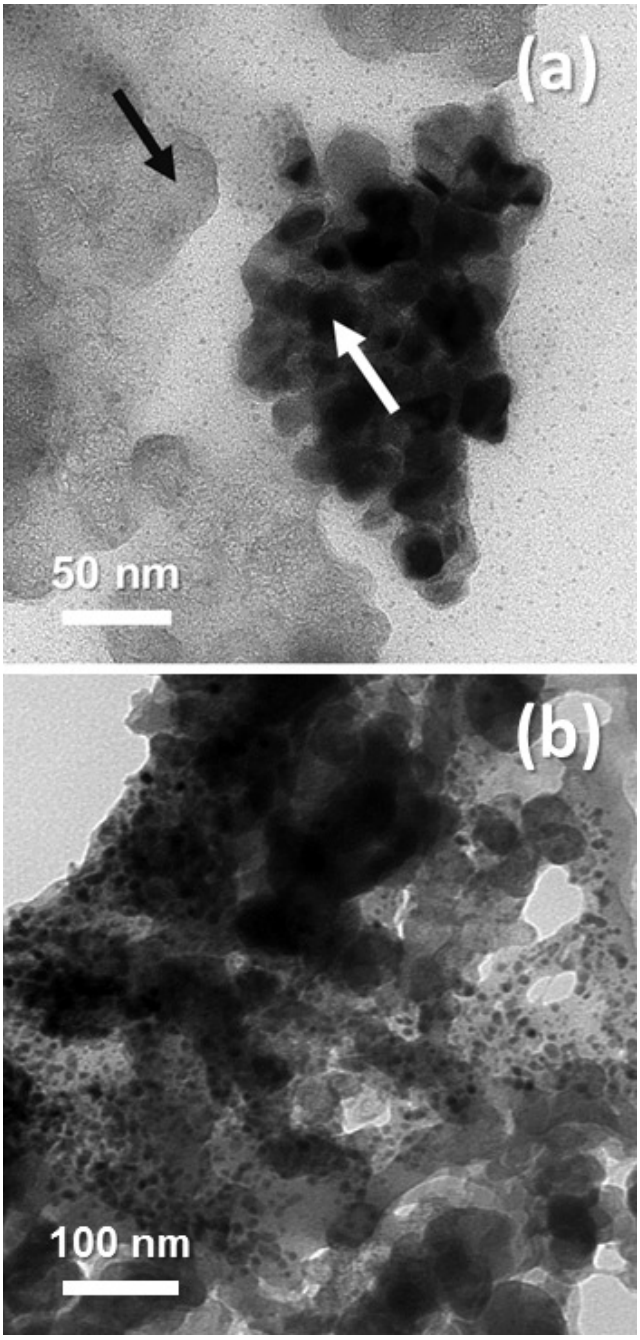


Figure 6.13. TEM images of the $GeO_2$ electrode cycled in FEC-based electrolyte after 500 cycles at 0.2 C (a) at a high magnification (b) at a low magnification. The black arrow in (a) indicates the carbon black, and the white arrow indicates the germanium.

The electrochemical impedance spectroscopic (EIS) observations of the $GeO_2$ nanoparticle electrodes tested in the EC-based electrolyte and the FEC-based electrolyte after 500 cycles at 0.2 C rate are summarized in the Nyquist plot of Figure 6.14. Typically, a Nyquist plot consists of two semicircles in the high frequency region (> 1 Hz) attributed to charge transfer processes, and a sloped line in the low frequency region (< 1 Hz) related to the mass transfer of $Li^+$. The first semicircle with a characteristic frequency at around 1 kHz represents the $Li^+$ transport in the SEI,[40] and the second semicircle represents the charge transfer between the SEI and the surface of the elemental Ge. Unlike the electrode cycled in the EC-based electrolyte, the 1 kHz semicircle was negligible (< 10 ohms in diameter) for the $GeO_2$ electrode cycled in the FEC-based electrolyte. It implies that the resistance of the FEC-derived SEI is negligible, just as it is in silicon nanoparticle anodes. The overall impedance was higher in the EC-based electrolyte than in the FEC-based electrolyte, revealing that electron transfer was more difficult for the $GeO_2$ electrode in the EC-based electrolyte after 500 cycles. This may have resulted from the electrode deterioration during the lithiation/de-lithiation process as seen by SEM (Figure 6.12(b)).

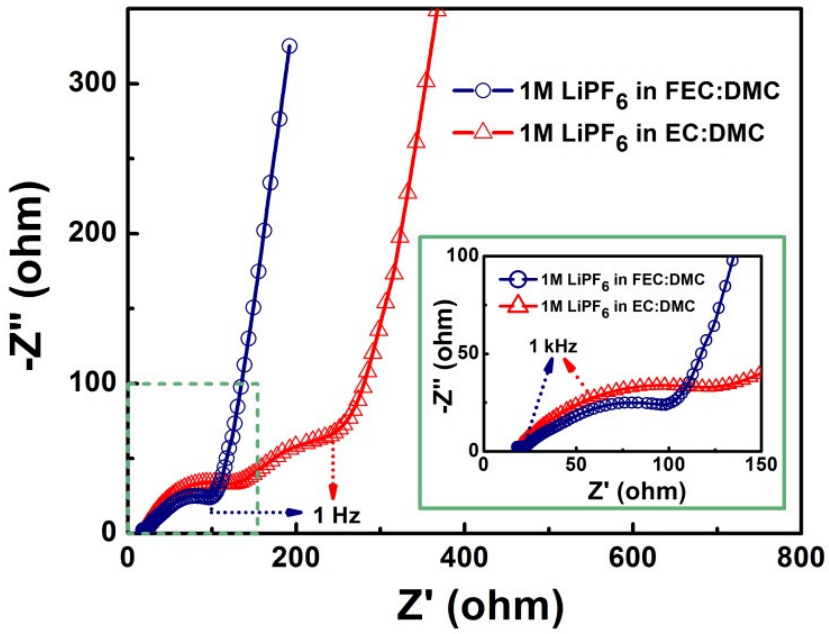


Figure 6.14. Electrochemical impedance spectroscopy of $GeO_2$ electrodes cycled in EC and FEC-based electrolyte after 500 cycles with an inset that shows a zoom view of Z' between 0 and 150 ohms.

The $GeO_2$ electrodes were next tested at higher current densities in cells cycled at 0.2 C for 150 cycles until their capacities became stable. The charge/discharge rate was increased stepwise from 0.5 C to 1C, 2C and 5C, with 10 cycles at each C rate (Figure 6.15). The $GeO_2$ electrodes performed very similarly in both EC-based and FEC-based electrolytes. Stable respective capacities of 550, 450, 320 mAh $g^{-1}$ were observed for rates of 0.5 C, 1 C and 2 C. When cycled at a C rate as high as 5 C, corresponding to a current density of 5.5 A $g^{-1}$, the $GeO_2$ electrodes still showed stable capacities of ~100

mAh $g^{-1}$ in both electrolytes. The decreased capacity at high rates is possibly attributed to the slow $Li^+$ permeation rate in $Li_2O$. Cycling at 0.5 - 5 C rates did not damage the electrodes; they recovered their full capacity (550 mAh $g^{-1}$) when returned to cycle at 0.2 C rate.

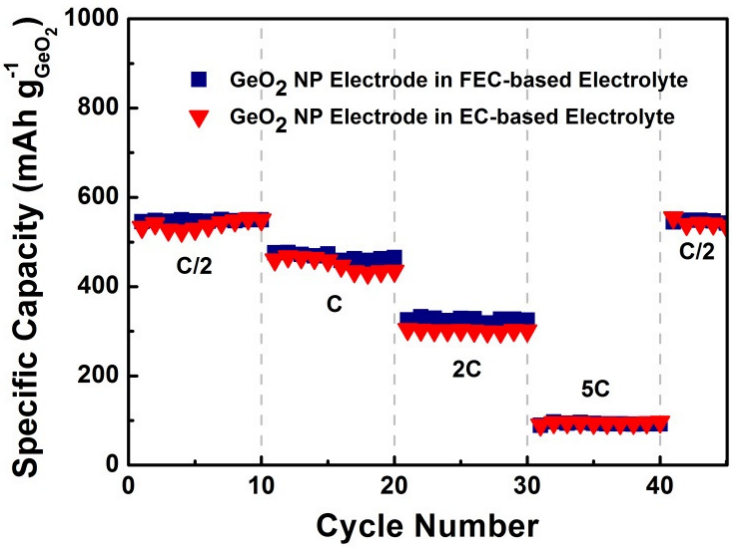


Figure 6.15. Reversible capacities of $GeO_2$ nanoparticle electrodes cycled at various C-rates in FEC and EC-based electrolytes.

## CONCLUSIONS

In conclusion, amorphous $GeO_2$ nanoparticles of decreasing diameters were prepared via a hydrothermal process with increasing amounts of 1,2-diaminopropane as the surfactant. The optimum reaction temperature was determined to be 180°C for the preparation of $GeO_2$ nanoparticles. Electrodes made with the $GeO_2$ nanoparticles exhibited a reversible capacity greater than 600 mAh $g^{-1}$ after 500 cycles at 0.2 C rate in a FEC-based electrolyte, retaining after 500 cycles more than 96% of their maximum capacity, outperforming the electrodes cycled in the conventional EC- based electrolyte under the same conditions. The improved performance of the $GeO_2$ electrode in the FEC-based electrolyte is attributed to a qualitatively different solid electrolyte interface, and the better preserved SEI and $Li_2O$ matrix which stabilized the electrode.

## REFERENCES


1. Tarascon, J. M.; Armand, M., *Nature* **2001,** *414* (6861), 359-367.

2. Goodenough, J. B.; Kim, Y., *Chem. Mater.* **2010,** *22* (3), 587-603.

3. Manthiram, A., *J. Phys. Chem. Lett.* **2011,** *2* (3), 176-184.

4. Abel, P. R.; Lin, Y.-M.; Celio, H.; Heller, A.; Mullins, C. B., *ACS Nano* **2012,** *6* (3), 2506-2516.

5. Winter, M.; Besenhard, J. O., *Electrochim. Acta* **1999,** *45* (1-2), 31-50.

6. Yang, J.; Winter, M.; Besenhard, J. O., *Solid State Ionics* **1996,** *90* (1-4), 281-287.

7. Klavetter, K. C.; Wood, S. M.; Lin, Y.-M.; Snider, J. L.; Davy, N. C.; Chockla, A. M.; Romanovicz, D. K.; Korgel, B. A.; Lee, J.-W.; Heller, A.; Mullins, C. B., *J. Power Sources* **2013**.

8. Bervas, M.; Klein, L. C.; Amatucci, G. G., *J. Electrochem. Soc.* **2006,** *153* (1), A159-A170.

9. Hariharan, S.; Saravanan, K.; Balaya, P., *Electrochemical and Solid State Letters* **2010,** *13* (9), A132-A134.

10. Lin, Y. M.; Abel, P. R.; Heller, A.; Mullins, C. B., *J. Phys. Chem. Lett.* **2011,** *2* (22), 2885-2891.

11. Cabana, J.; Monconduit, L.; Larcher, D.; Palacin, M. R., *Adv. Mater. (Weinheim, Ger.)* **2010,** *22* (35), E170-E192.

12. Alcantara, R.; Fernandez-Madrigal, F. J.; Lavela, P.; Tirado, J. L.; Jumas, J. C.; Olivier-Fourcade, J., *J. Mater. Chem.* **1999,** *9* (10), 2517-2521.

13. Prosini, P. P.; Mancini, R.; Petrucci, L.; Contini, V.; Villano, P., *Solid State Ionics* **2001,** *144* (1-2), 185-192.

14. Lin, Y. M.; Abel, P. R.; Flaherty, D. W.; Wu, J.; Stevenson, K. J.; Heller, A.; Mullins, C. B., *J. Phys. Chem. C* **2011,** *115* (5), 2585-2591.

15. Graetz, J.; Ahn, C. C.; Yazami, R.; Fultz, B., *J. Electrochem. Soc.* **2004,** *151* (5), A698-A702.

16. Holl, R.; Kling, M.; Schroll, E., *Ore Geology Reviews* **2007,** *30* (3-4), 145-180.

17. Dianov, E. A.; Mashinsky, V. A., *J. Lightwave Technol.* **2005,** *23* (11), 3500-3508.

18. Sakaguchi, S.; Todoroki, S., *Appl. Opt.* **1997,** *36* (27), 6809-6814.

19. Bose, N.; Basu, M.; Mukherjee, S., *Mater. Res. Bull.* **2012,** *47* (6), 1368-1373.

20. Pena, J. S.; Sandu, I.; Joubert, O.; Pascual, F. S.; Arean, C. O.; Brousse, T., *Electrochemical and Solid State Letters* **2004,** *7* (9), A278-A281.

21. Feng, J. K.; Lai, M. O.; Lu, L., *Electrochim. Acta* **2012,** *62*, 103-108.

22. Lu, L.; Sui, M. L.; Lu, K., *Science* **2000,** *287* (5457), 1463-1466.

23. McFadden, S. X.; Mishra, R. S.; Valiev, R. Z.; Zhilyaev, A. P.; Mukherjee, A. K., *Nature* **1999,** *398* (6729), 684-686.

24. Aurbach, D.; Markovsky, B.; Shechter, A.; EinEli, Y.; Cohen, H., *J. Electrochem. Soc.* **1996,** *143* (12), 3809-3820.

25. McMillan, R.; Slegr, H.; Shu, Z. X.; Wang, W. D., *J. Power Sources* **1999,** *81*, 20-26.

26. Nakai, H.; Kubota, T.; Kita, A.; Kawashima, A., *J. Electrochem. Soc.* **2011,** *158* (7), A798-A801.

27. Etacheri, V.; Haik, O.; Goffer, Y.; Roberts, G. A.; Stefan, I. C.; Fasching, R.; Aurbach, D., *Langmuir* **2012,** *28* (1), 965-976.

28. Lin, Y. M.; Klavetter, K. C.; Abel, P. R.; Davy, N. C.; Snider, J. L.; Heller, A.; Mullins, C. B., *Chem. Commun. (Cambridge, U. K.)* **2012,** *48* (58), 7268-7270.

29. Chockla, A. M.; Bogart, T. D.; Hessel, C. M.; Klavetter, K. C.; Mullins, C. B.; Korgel, B. A., *J. Phys. Chem. C* **2012,** *116* (34), 18079-18086.

30. Choi, N. S.; Yew, K. H.; Lee, K. Y.; Sung, M.; Kim, H.; Kim, S. S., *J. Power Sources* **2006,** *161* (2), 1254-1259.

31. Chockla, A. M.; Klavetter, K. C.; Mullins, C. B.; Korgel, B. A., *ACS Appl. Mater. Interfaces* **2012,** *4* (9), 4658-4664.

32. Profatilova, I. A.; Stock, C.; Schmitz, A.; Passerini, S.; Winter, M., *J. Power Sources* **2013,** *222*, 140-149.

33. McDowell, M. T.; Lee, S. W.; Harris, J. T.; Korgel, B. A.; Wang, C.; Nix, W. D.; Cui, Y., *Nano Lett.* **2013,** *13* (2), 758-764.

34. Li, Z. M.; Lai, X. Y.; Wang, H.; Mao, D.; Xing, C. J.; Wang, D., *Nanotechnology* **2009,** *20* (24), 245603.

35. Liu, N. A.; Hu, L. B.; McDowell, M. T.; Jackson, A.; Cui, Y., *ACS Nano* **2011,** *5* (8), 6487-6493.

36. Wang, X. L.; Han, W. Q.; Chen, H. Y.; Bai, J. M.; Tyson, T. A.; Yu, X. Q.; Wang, X. J.; Yang, X. Q., *J. Am. Chem. Soc.* **2011,** *133* (51), 20692-20695.

37. Jarvis, C. R.; Lain, M. J.; Yakovleva, M. V.; Gao, Y., *J. Power Sources* **2006,** *162* (2), 800-802.

38. Lin, Y. M.; Nagarale, R. K.; Klavetter, K. C.; Heller, A.; Mullins, C. B., *J. Mater. Chem.* **2012,** *22* (22), 11134-11139.

39. McArthur, M. A.; Trussler, S.; Dahn, J. R., *J. Electrochem. Soc.* **2012,** *159* (3), A198-A207.

40. Yamada, Y.; Iriyama, Y.; Abe, T.; Ogumi, Z., *J. Electrochem. Soc.* **2010,** *157* (1), A26-A30.

# Chapter 7: Sn-Cu Alloy Anodes for Rechargeable Sodium Ion Batteries

## INTRODUCTION

Electrical energy storage is of growing importance for both stationary and mobile applications. Among energy storage systems, rechargeable lithium-based batteries have been studied because lithium has the most negative reduction potential (-3.04 V vs. standard hydrogen electrode, SHE) and the lowest density (0.53 g $cm^{-3}$) of all metals.[1] Currently, Li-ion batteries are widely adopted to power portable electronic devices. However, their high price remains a daunting challenge in medium to large-scale energy storage required for transportation or grid energy storage.[2-4] Lithium is a relatively rare element among light metals, its concentration in the upper continental crust is estimated to be 35 ppm.[5] Sodium, unlike lithium, is much more abundant on earth, where the sodium concentration is estimated to be 10,320 ppm in seawater and 28,300 ppm in the lithosphere.[6] Consequently, in those applications where the amount of electrode material is large enough to substantially affect the cost, the use of sodium is advantageous. The low reduction potential of Na (-2.71 V vs. SHE) also makes it an attractive material for energy storage. Molten-salt batteries containing sodium, e.g. Na/S and $Na/NiCl_2$ batteries,[7, 8] have been developed as inexpensive energy storage systems for load leveling systems. However, these batteries need to operate at high temperatures (250 to 350°C) to keep the electrodes in liquid form, which makes it more difficult for designing battery

systems that meet stringent safety requirements. Therefore, it is important to develop an affordable secondary Na-ion battery that can be cycled at ambient temperature.

Current commercial Li-ion batteries are comprised of lithium metal oxide as the cathode material and graphite as the lithium host anode material. The electrical energy is stored via the difference of chemical potential of lithium between the cathode and the anode. A similar mechanism can be applied to Na-ion batteries. Recently, Prussian blue and a few other materials have been identified as promising candidates as the cathode materials.[9, 10] However, graphite cannot be readily used as the anode material for Na-ion batteries because for sodium atoms it is more thermodynamically favorable to electroplate onto the surface of graphite than to intercalate into its basal planes.[11] Thus far, few materials have been considered for Na-ion anodes. Sb has been reported as a candidate anode material for Na storage, exhibiting a high reversible capacity of ~ 600 mA $g^{-1}$.[12, 13] Additionally, Chevrier and Ceder predicted from density functional theory calculations that Na alloys of Si, Ge, Sn and Pb, could also be used as anode materials for Na-ion batteries.[14] Among these materials, tin is of great interest because of its high theoretical capacity 847 mAh $g^{-1}$ or 6164 mAh $cm^{-3}$, corresponding to the most sodium-rich phase $Na_{15}Sn_4$.[14-16] Nohira and Hagiwara et al. found an initial reversible capacity as high as 729 mAh $g^{-1}$ for sodium storage using a Sn thin film electrode.[17] However, the capacity was not well retained, decreasing to 121 mAh $g^{-1}$ as early as the 10th cycle. The rapid degradation of the Sn electrode was attributed to the volume change during sodium insertion/de-insertion. Because nanostructured materials can superplastically deform,

they can sustain very large strains, of more than 200 % elongation.[18, 19] However, Sn nanoparticles are thermodynamically unstable relative to Sn microparticles that tend to aggregate to reduce their large surface energy.[20, 21] Intermetallic alloy anodes show better electrochemical performance for Lithium-ion insertion/de-insertion because of lesser aggregation of their electroactive particles.[22] In Na-ion batteries, Sn nanocomposite anodes, such as Sn/C and SnSb/C,[23, 24] exhibited improved cycling stability, but their capacities still dropped noticeably after fewer than 50 cycles. Therefore, a core challenge to address in safer sodium alloy anodes is that of cycling stability upon the alloying/de-alloying of sodium.

## EXPERIMENTAL METHODS

*Materials and Synthesis:* $Sn_{0.9}Cu_{0.1}$ nanoparticles were prepared by adding 18 mmol tin chloride dihydrate ($SnCl_2 \cdot 2H_2O$, Alfa Aesar) and 2 mmol copper nitrate hydrate ($Cu(NO_3)_2 \cdot 2.5H_2O$, Alfa Aesar) into 200 ml deionized water (DIW) with 20 ml hydrochloric acid (HCl, Fisher Scientific) added. After stirring for 15 min, 20g of 1,2-diaminopropane ($C_3H_{10}N_2$, Alfa Aesar) was added into the solution and stirring was continued for another 15 min. Then a sodium borohydride ($NaBH_4$, Alfa Aesar) aqueous solution (0.1 mole $NaBH_4$ in 20ml DIW) was added dropwise into the above solution. The whole mixture was stirred continuously for 24 hours. The resulting dark-grey

precipitate was collected by centrifuge, washed with DIW twice and dried under vacuum at 70 °C.

*Physical Characterization:* The synthesized $Sn_{0.9}Cu_{0.1}$ powders were characterized by scanning electron microscopy (SEM) with a Hitachi S-5500 electron microscope and a 30 kV accelerating voltage. The SEM is equipped with a Bruker EDS Quantax 4010 energy dispersive X-ray spectroscopic (EDS) detector for elemental analysis. For transmission electron microscopy, a JEOL 2010F TEM was used at an accelerating voltage of 200 kV. X-ray powder diffraction was performed with a Rigaku R-Axis Spider diffractometer having an image-plate detector with graphite-monochromatized CuKα (λ=1.5418 Å) radiation operated at 40 kV and 40 mA.

*Electrochemical Measurements:* To evaluate the electrochemical performance, electrodes were prepared by mixing the Sn microparticles (#325 mesh, Alfa Aesar), Sn nanoparticles (60-80 nm, US Research Nanomaterials) or the prepared $Sn_{0.9}Cu_{0.1}$ particles (80 wt %) with conductive carbon black (Super P-Li, Timcal) (10 wt %) and with 90 kDa sodium carboxymethyl cellulose (Aldrich) (10 wt %) with DIW as the dispersing medium. The mixture was slurry-cast on a 10 μm thick Cu foil with an automatic film applicator, then dried under vacuum at 120°C for 12 hrs. Next, the as-prepared $Sn_{0.9}Cu_{0.1}$ slurry-cast film was punched into disk working electrodes. Typically, the mass loading of materials on Cu foil is ~600 μg $cm^{-2}$ containing ~480 μg $cm^{-2}$ of $Sn_{0.9}Cu_{0.1}$ or Sn particles. The electrochemical measurements were carried out with stainless steel 2032 coin cells

and a Na foil counter/reference electrode. The Na foil was rolled from a sodium dry stick (Aldrich) and was polished with sandpaper to remove the surface oxide. The cells were assembled in an argon-atmosphere glovebox with 1M $NaPF_6$ (>99%, Alfa Aesar) in FEC (>99%, Solvay Chemicals)/DEC (≥99%, Aldrich) (1:1 wt/wt) as the electrolyte. A polypropylene membrane (Celgard 2400, Celgard) was used as a separator. The assembled coin cells were galvanostatically cycled at room temperature in a multichannel battery test system (BT 2043, Arbin) between 10 mV and 0.75 V. An electrochemical analyzer (CHI 604D, CH Instruments) was used for electrochemical impedance spectroscopy (EIS), carried out over a wide frequency range from 100 kHz to 0.05 Hz with an ac perturbation voltage of 5 mV.

## RESULTS AND DISCUSSION

A scanning electron microscope (SEM) image shows that the diameter of a typical $Sn_{0.9}Cu_{0.1}$ particle is ~100 nm (Figure 7.1(a)). Energy dispersive X-ray spectroscopy (EDS) of the nanocomposite showed (Table 7.1) an average Sn/Cu molar ratio of 0.896/0.104. A SEM image of a typical Sn/Cu particle taken at a higher magnification is shown in Figure 7.2(a), with a linear EDS scan performed across the center of the The EDS line-scan shows that the composition of the particle is spatially homogeneous. EDS elemental mapping confirmed that Sn and Cu are uniformly distributed in the nanocomposite (Figure 7.2(b) and 7.2(c)). Transmission electron microscopy (TEM)

shows that the $Sn_{0.9}Cu_{0.1}$ nanocomposite particle is actually composed of multiple small monocrystals (Figure 7.2(d)), each of ~5 nm (Figure 7.2(e)). The powder X-ray diffraction (XRD) pattern of the as-prepared $Sn_{0.9}Cu_{0.1}$ nanoparticles shows a tin-rich composite made of crystalline Sn and $Sn_5Cu_6$ (Figure 7.2(f)).

The electrochemical performance of the prepared $Sn_{0.9}Cu_{0.1}$ nanoparticles was evaluated in 2032 type coin cells. Commercially available Sn nanoparticles (~100 nm) and Sn microparticles (>1 μm), with their SEM images shown in Figures 7.1(b) and 7.1(c) and their XRD patterns shown in Figure 7.3, were employed as references for comparison with the $Sn_{0.9}Cu_{0.1}$ nanoparticles. The electrodes were prepared by slurry casting of 80% of either $Sn_{0.9}Cu_{0.1}$ or the reference Sn, 10% sodium carboxymethyl cellulose (Na-CMC) binder and 10% carbon black as the conductive additive. Cells were assembled and tested against a sodium-metal foil counter/reference electrode with 1M $NaPF_6$ in fluoroethylene carbonate (FEC)/diethyl carbonate (DEC) (1/1 wt/wt) as the electrolyte. FEC as an additive or as a co-solvent in the electrolyte has been shown to improve the electrochemical performance of both Li-ion and Na-ion batteries.[12, 13, 25-29]

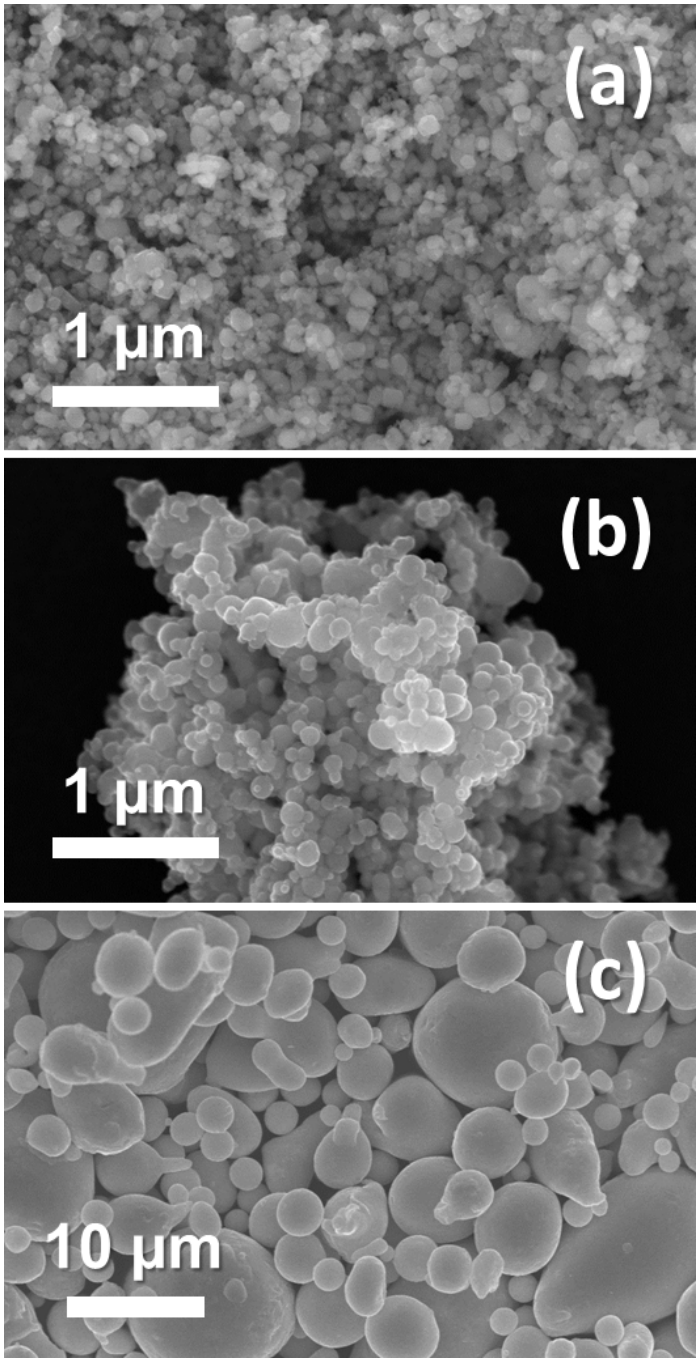


Figure 7.1. SEM images of (a) $Sn_{0.9}Cu_{0.1}$ nanoparticles (b) Sn nanoparticles (c) Sn microparticles.

Table 7.1. Results of elemental analysis on Sn/Cu nanocomposite by EDS.

| Element | Series | Weight Ratio (%) | Atomic Ratio (%) | Error (%) |
|---|---|---|---|---|
| Tin | L-series | 94.16 | 89.62 | 2.2 |
| Copper | K-series | 5.84 | 10.38 | 0.17 |

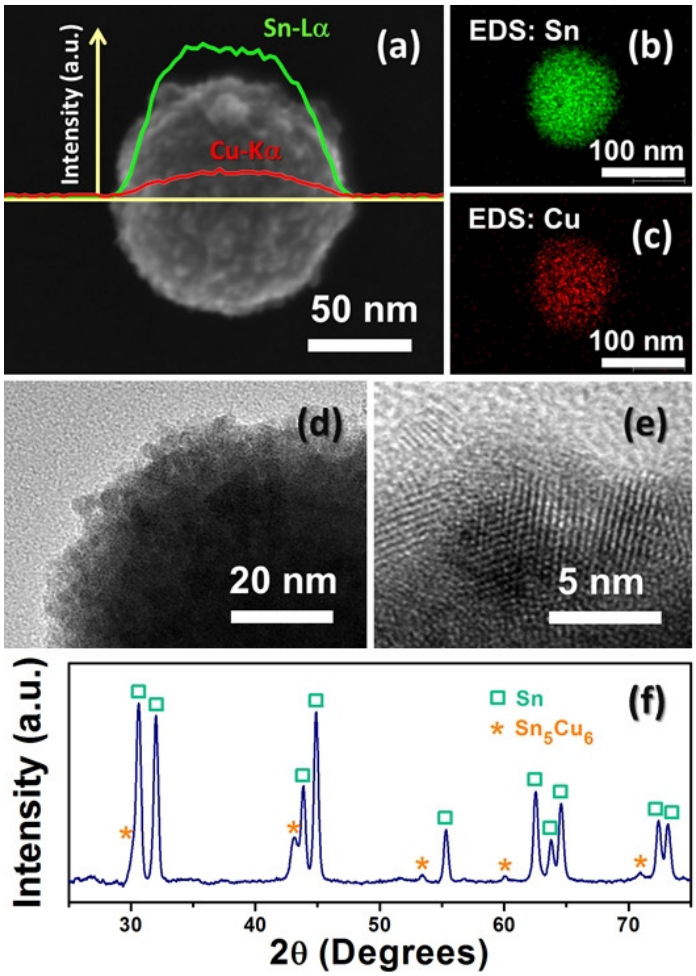


Figure 7.2. (a) SEM image of a single $Sn_{0.9}Cu_{0.1}$ particle with EDS line scan across the particle; EDS mapping for element (b) Sn and (c) Cu; TEM images of a single $Sn_{0.9}Cu_{0.1}$ particle examined under (d) low magnification and (e) high magnification; (f) X-ray diffraction pattern of the $Sn_{0.9}Cu_{0.1}$ powder.

The assembled cells were cycled between 10 mV and 750 mV vs. $Na/Na^+$ at a 0.2 C rate (169 mA per gram of Sn), corresponding to a rate of fully charging or discharging the cell within 5 hours. Reversible capacities for one hundred cycles for electrodes made with the $Sn_{0.9}Cu_{0.1}$ nanocomposite, Sn nanoparticles and Sn microparticles are shown in Figure 7.4. The changes in the capacities of the electrodes made with Sn nanoparticles and Sn microparticles were similar in the first few cycles, both reaching their maximum capacity of ~510 mAh $g^{-1}$ after 3 cycles, implying a rapid diffusion of sodium in Sn. However, the capacity of the electrode made of larger Sn particles (>1 μm) dropped much more rapidly than that made of smaller particles (~100 nm), showing that the large volume change upon cycling is better accommodated by small particles. After 100 cycles, the capacities of the electrodes made of Sn nanoparticles and Sn microparticles decreased respectively to 250 mAh $g^{-1}$ and 66 mAh $g^{-1}$, i.e. only 49% and 13% of their maximum capacity was retained, suggestive of volume-change associated electrochemical agglomeration of the Sn nanoparticles, similar to that observed in Li/Sn alloys.[20-22]

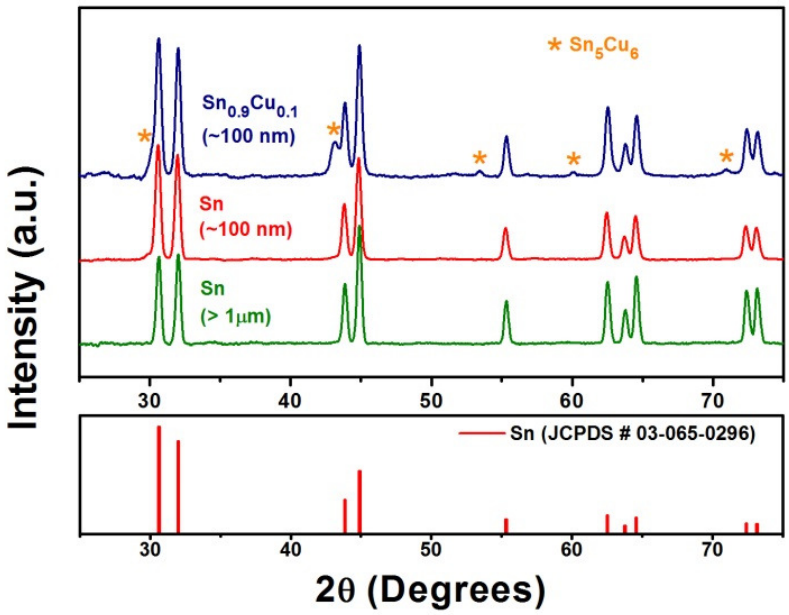


Figure 7.3. X-ray powder diffraction patterns of the $Sn_{0.9}Cu_{0.1}$ nanoparticles, Sn nanoparticles and Sn microparticles.

The reversible capacity of the $Sn_{0.9}Cu_{0.1}$ electrode was 250 mAh $g^{-1}$ in the initial cycle, gradually increasing to ~440 mAh $g^{-1}$ after 20 cycles (Figure 7.4). The added mass of copper accounts for the lesser specific maximum capacity of $Sn_{0.9}Cu_{0.1}$ versus that of Sn, because Cu does not form an alloy with sodium. However, compared to the Sn-based electrodes, the $Sn_{0.9}Cu_{0.1}$ nanoparticle electrode shows significantly improved stability during prolonged sodium insertion/de-insertion cycling, with 97% of the reversible capacity being retained between the 20$^{th}$ cycle and the 100$^{th}$ cycle.

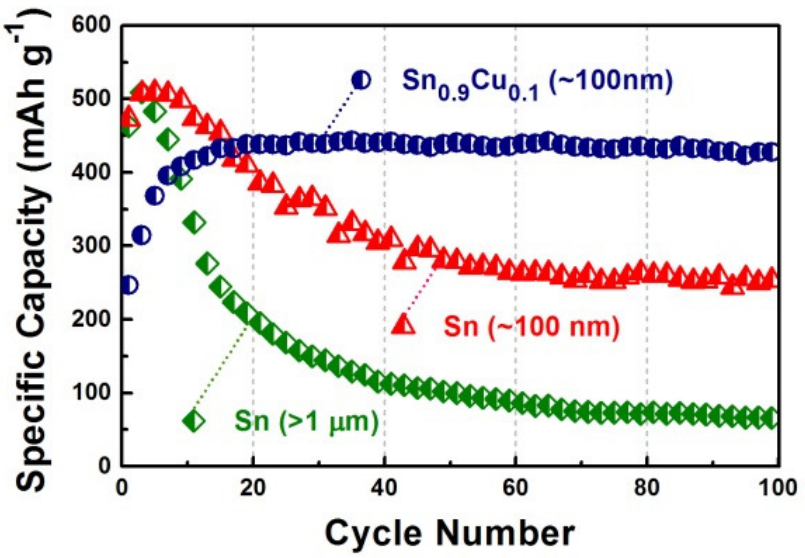


Figure 7.4. Reversible capacities of electrodes made of $Sn_{0.9}Cu_{0.1}$ nanoparticles, Sn nanoparticles, and Sn microparticles. All electrodes cycled at 0.2 C rate (169 mA $g^{-1}$).

Figure 7.5 shows the voltage profiles of electrodes made of $Sn_{0.9}Cu_{0.1}$ nanoparticles, Sn nanoparticles and Sn microparticles for cycles 1, 20 and 100 at 0.2 C rate. In the initial half cycle starting from the open circuit voltage for each cell, sodium reacts with tin to form a series of Na-Sn alloys. The reactions involve forming the solid electrolyte interface (SEI), resulting in an irreversible capacity loss during the first cycle. The Coulombic efficiencies of the first cycle are 35%, 72% and 73% for $Sn_{0.9}Cu_{0.1}$, Sn nanoparticle and Sn microparticle electrodes, respectively. The low initial Coulombic efficiency of the $Sn_{0.9}Cu_{0.1}$ electrode may be attributed to the small primary crystallites seen by TEM, providing extra surface area for SEI formation. This is supported by the

appearance of a shoulder above 0.5 V in the case of the $Sn_{0.9}Cu_{0.1}$ electrode (indicated by a red arrow in Figure 7.5(a)) in the initial sodium insertion process, a feature which is absent in the following cycles. The low initial Coulombic efficiency of $Sn_{0.9}Cu_{0.1}$ could be a problem in those applications where the anode is paired with a cathode containing a limited amount of sodium. To overcome the problem, extra sacrificial Na could be added to the anode, as is done in some lithium batteries.[30, 31] Although the first cycle efficiency of the $Sn_{0.9}Cu_{0.1}$ electrode is low, it increased to more than 95% from cycle 2 and eventually reached 99% at the end of 100 cycles (Figure 7.6). The voltage profiles of the $Sn_{0.9}Cu_{0.1}$ electrode are almost identical between cycle 20 and cycle 100, indicating that the incorporation of Cu into Sn improves the stability upon Na insertion/de-insertion. The better stability is attributed to the higher melting point and much better mechanical strength of the $Sn_{0.9}Cu_{0.1}$ alloy which suppresses electrochemical aggregation, resulting in better cyclability.

The electrochemical impedance spectroscopy (EIS) measurements of the electrodes made of $Sn_{0.9}Cu_{0.1}$ nanoparticles, Sn nanoparticles and Sn microparticles after 100 cycles at 0.2 C rate are shown in Nyquist plots (Figure 7.7). The measurements were carried out over a frequency range from 100 kHz to 0.05 Hz at 0.75 V with an AC perturbation voltage of 5 mV. Each plot consists of a semicircle in the high frequency region (> 1 Hz) attributed to the charge transfer process, and a sloped line in the low frequency region (< 1 Hz) related to the mass transfer of $Na^+$. The charge-transfer resistance can be determined by measuring the diameter of the semicircle in the Nyquist

plot. The electrode made of Sn microparticles has a large charge-transfer resistance, ~900 Ω, higher than that of the electrode made of Sn nanoparticles (~700 Ω). This suggests that after cycling, the transfer of electrons becomes more difficult in the electrode made of larger particles. This may be a result of the structural instability of Sn microparticles during the sodium insertion/de-insertion process. Compared to the electrodes made of Sn nanoparticles and Sn microparticles, the $Sn_{0.9}Cu_{0.1}$ nanoparticle electrode has a much smaller charge transfer resistance ~300 Ω, indicating that incorporating copper into tin reduces the interfacial charge transfer resistance.

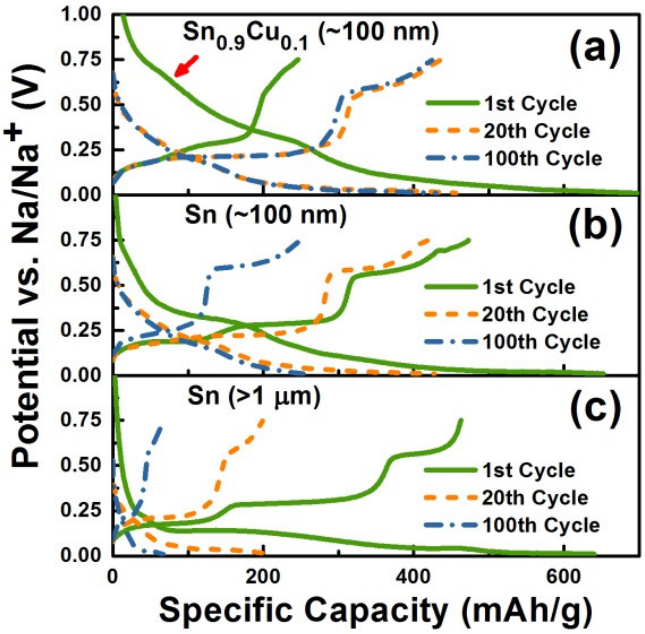


Figure 7.5. Voltage profiles of electrodes made of (a) $Sn_{0.9}Cu_{0.1}$ nanoparticles (b) Sn nanoparticles and (c) Sn microparticles. All electrodes cycled at 0.2 C rate (169 mA $g^{-1}$). The red arrow indicates an additional feature for the $Sn_{0.9}Cu_{0.1}$ electrode in the initial Na insertion process.

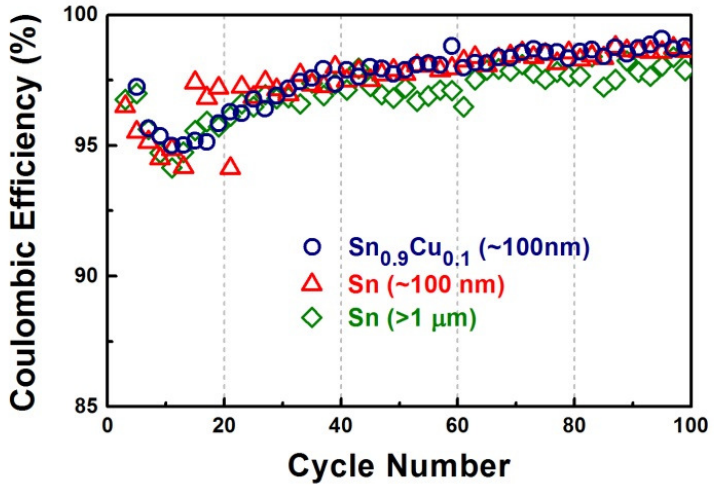


Figure 7.6. Coulombic efficiencies of electrodes made of $Sn_{0.9}Cu_{0.1}$ nanoparticles, Sn nanoparticles, Sn microparticles. All electrodes cycled at 0.2 C rate (169 mA $g^{-1}$).

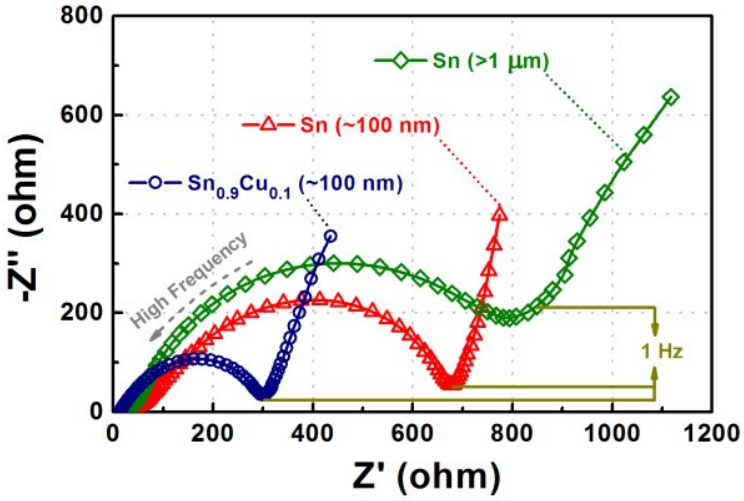


Figure 7.7. Electrochemical impedance spectroscopy of electrodes made of $Sn_{0.9}Cu_{0.1}$ nanoparticles, Sn nanoparticles and Sn microparticles. All measured after 100 cycles at 0.2 C rate.

Electrodes made of $Sn_{0.9}Cu_{0.1}$ nanoparticles and Sn nanoparticles were also tested at higher current densities. The charge/discharge rate was increased stepwise from 0.2 C (169 mA $g^{-1}$) to 0.5 C, 1C and 2C (1694 mA $g^{-1}$), with each C rate for 20 cycles, as shown in Figure 7.8. The average reversible capacities of each electrode as a function of current density are shown in Figure 7.9. The reversible capacities decrease with increasing current densities for all electrodes because the reactions are kinetically constrained at high rates. Nevertheless, the high-rate performance of the $Sn_{0.9}Cu_{0.1}$ electrode was much better than the Sn nanoparticle electrode. At current densities of 424, 847, 1694 mA $g^{-1}$, the $Sn_{0.9}Cu_{0.1}$ electrode retained capacities of 265, 182, 126 mAh $g^{-1}$ while the Sn electrode retained only 222, 120, 50 mAh $g^{-1}$, respectively. Typical voltage profiles at various rates are shown in Figure 7.10. Compared to the Sn electrode, less potential polarization is observed between charge and discharge half-cycles for the $Sn_{0.9}Cu_{0.1}$ electrode at high rates, consistent with the lesser charge transfer resistance seen in the Nyquist plots of Figure 7.7. Furthermore, cycling at 0.2 – 2 C rates doesn't damage the $Sn_{0.9}Cu_{0.1}$ electrode, for which its capacity is fully recovered upon returning to cycling at the 0.2 C rate, as shown in Figure 7.8.

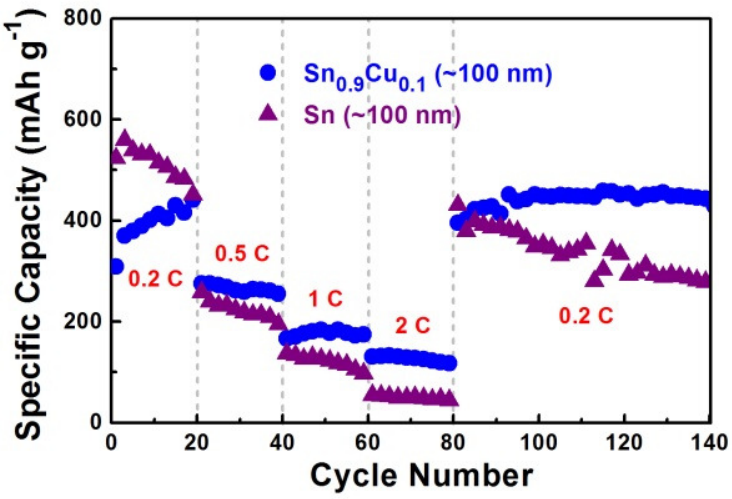


Figure 7.8. Reversible capacities of electrodes made of $Sn_{0.9}Cu_{0.1}$ nanoparticles and Sn nanoparticles cycled at various C rates from 0.2 to 2 C.

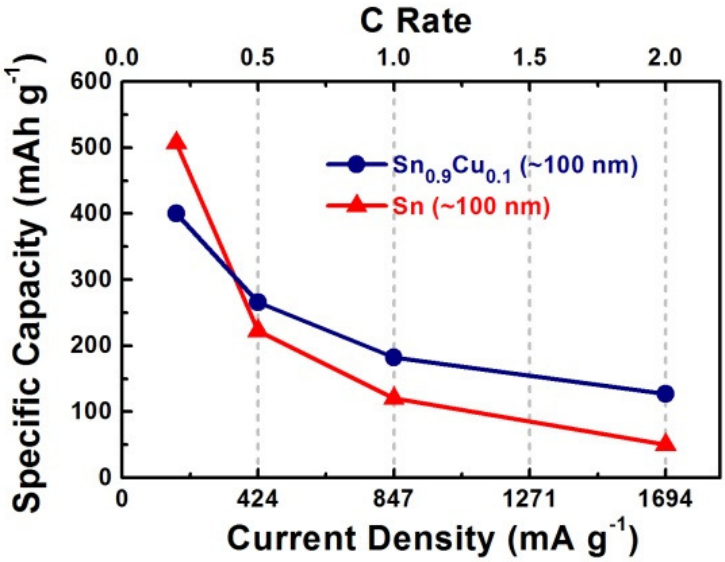


Figure 7.9. Reversible capacities of electrodes made of $Sn_{0.9}Cu_{0.1}$ nanoparticles and Sn nanoparticles as a function of current density from 169 to 1694 mA $g^{-1}$ (0.2 C to 2 C rates).

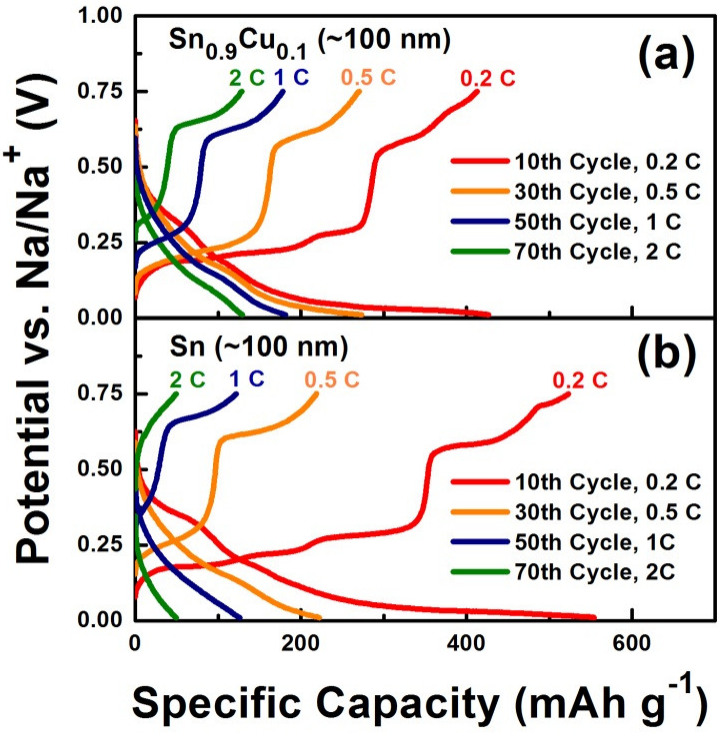


Figure 7.10. Voltage profiles of electrodes made of (a) $Sn_{0.9}Cu_{0.1}$ nanoparticles (b) Sn nanoparticles that cycled at various C-rates.

## CONCLUSIONS

In conclusion, inexpensively made $Sn_{0.9}Cu_{0.1}$ nanoparticles constitute a promising Na-ion battery anode material. Electrodes made with the $Sn_{0.9}Cu_{0.1}$ nanoparticles exhibit a stable capacity of greater than 420 mAh $g^{-1}$ at 0.2 C rate, retaining 97% of their capacity after 100 cycles of sodium insertion/de-insertion. In contrast, electrodes made with Sn microparticles and Sn nanoparticles retained, respectively, only 13% and 49% of their capacities after 100 cycles at 0.2 C rate. The $Sn_{0.9}Cu_{0.1}$ electrode also showed better rate capability relative to a Sn nanoparticle electrode. Incorporation of copper in the tin reduced the interfacial charge transfer resistance and suppressed the aggregation of the nanoparticles, thereby improving the cyclability and high-rate capability of the anodes.

## REFERENCES


1. Tarascon, J. M.; Armand, M., *Nature* **2001,** *414* (6861), 359-367.

2. Chalk, S. G.; Miller, J. E., *J. Power Sources* **2006,** *159*, 73-80.

3. Kim, S. W.; Seo, D. H.; Ma, X. H.; Ceder, G.; Kang, K., *Adv. Energy Mater.* **2012,** *2* (7), 710-721.

4. Dunn, B.; Kamath, H.; Tarascon, J. M., *Science* **2011,** *334* (6058), 928-935.

5. Teng, F. Z.; McDonough, W. F.; Rudnick, R. L.; Dalpe, C.; Tomascak, P. B.; Chappell, B. W.; Gao, S., *Geochim. Cosmochim. Acta* **2004,** *68* (20), 4167-4178.

6. Seyfried, W. E.; Janecky, D. R.; Mottl, M. J., *Geochim. Cosmochim. Acta* **1984,** *48* (3), 557-569.

7. Lu, X. C.; Xia, G. G.; Lemmon, J. P.; Yang, Z. G., *J. Power Sources* **2010,** *195* (9), 2431-2442.

8. Sudworth, J. L., *J. Power Sources* **2001,** *100* (1-2), 149-163.

9. Lu, Y. H.; Wang, L.; Cheng, J. G.; Goodenough, J. B., *Chem. Commun. (Cambridge, U. K.)* **2012,** *48* (52), 6544-6546.

10. Wang, L.; Lu, Y. H.; Liu, J.; Xu, M. W.; Cheng, J. G.; Zhang, D. W.; Goodenough, J. B., *Angew. Chem. Int. Edit.* **2013,** *52* (7), 1964-1967.

11. Stevens, D. A.; Dahn, J. R., *J. Electrochem. Soc.* **2001,** *148* (8), A803-A811.

12. Qian, J. F.; Chen, Y.; Wu, L.; Cao, Y. L.; Ai, X. P.; Yang, H. X., *Chem. Commun. (Cambridge, U. K.)* **2012,** *48* (56), 7070-7072.

13. Darwiche, A.; Marino, C.; Sougrati, M. T.; Fraisse, B.; Stievano, L.; Monconduit, L., *J. Am. Chem. Soc.* **2012,** *134* (51), 20805-20811.

14. Chevrier, V. L.; Ceder, G., *J. Electrochem. Soc.* **2011,** *158* (9), A1011-A1014.

15. Slater, M. D.; Kim, D.; Lee, E.; Johnson, C. S., *Adv. Funct. Mater.* **2013,** *23* (8), 947-958.

16. Ellis, L. D.; Hatchard, T. D.; Obrovac, M. N., *J. Electrochem. Soc.* **2012,** *159* (11), A1801-A1805.

17. Yamamoto, T.; Nohira, T.; Hagiwara, R.; Fukunaga, A.; Sakai, S.; Nitta, K.; Inazawa, S., *J. Power Sources* **2012,** *217*, 479-484.

18. Lu, L.; Sui, M. L.; Lu, K., *Science* **2000,** *287* (5457), 1463-1466.

19. McFadden, S. X.; Mishra, R. S.; Valiev, R. Z.; Zhilyaev, A. P.; Mukherjee, A. K., *Nature* **1999,** *398* (6729), 684-686.

20. Kim, C.; Noh, M.; Choi, M.; Cho, J.; Park, B., *Chem. Mater.* **2005,** *17* (12), 3297-3301.

21. Li, H.; Shi, L. H.; Lu, W.; Huang, X. J.; Chen, L. Q., *J. Electrochem. Soc.* **2001,** *148* (8), A915-A922.

22. Zhang, W. J., *J. Power Sources* **2011,** *196* (1), 13-24.

23. Xu, Y. H.; Zhu, Y. J.; Liu, Y. H.; Wang, C. S., *Adv. Energy Mater.* **2013,** *3* (1), 128-133.

24. Xiao, L. F.; Cao, Y. L.; Xiao, J.; Wang, W.; Kovarik, L.; Nie, Z. M.; Liu, J., *Chem. Commun. (Cambridge, U. K.)* **2012,** *48* (27), 3321-3323.

25. Qian, J.; Wu, X.; Cao, Y.; Ai, X.; Yang, H., *Angew. Chem.* **2013,** *125* (17), 4731-4734.

26. Nakai, H.; Kubota, T.; Kita, A.; Kawashima, A., *J. Electrochem. Soc.* **2011,** *158* (7), A798-A801.

27. Lin, Y. M.; Klavetter, K. C.; Abel, P. R.; Davy, N. C.; Snider, J. L.; Heller, A.; Mullins, C. B., *Chem. Commun. (Cambridge, U. K.)* **2012,** *48* (58), 7268-7270.

28. Komaba, S.; Ishikawa, T.; Yabuuchi, N.; Murata, W.; Ito, A.; Ohsawa, Y., *ACS Appl. Mater. Interfaces* **2011,** *3* (11), 4165-4168.

29. Kravchyk, K.; Protesescu, L.; Bodnarchuk, M. I.; Krumeich, F.; Yarema, M.; Walter, M.; Guntlin, C.; Kovalenko, M. V., *J. Am. Chem. Soc.* **2013,** *135* (11), 4199-4202.

30. Liu, N. A.; Hu, L. B.; McDowell, M. T.; Jackson, A.; Cui, Y., *ACS Nano* **2011,** *5* (8), 6487-6493.

31. Jarvis, C. R.; Lain, M. J.; Yakovleva, M. V.; Gao, Y., *J. Power Sources* **2006,** *162* (2), 800-802.

# Chapter 8: Concluding Remarks and Future Research

## OVERVIEW OF COMPLETED WORK

In this dissertation, several as lithium-ionand sodium-ion battery anode material were investigated. Their electrochemical properties were shown to be significantly altered by modifying either their structure or composition. Additionally, modifications of the solid electrolyte interface by altering the electrolyte were shown to massively impact on their cycling stability. Their syntheses and characterization allowed correlation of the materials' structure and their electrochemical properties.

In Chapter 2, reactive ballistic deposition (RBD) was employed to grow highly structured films of $TiO_2$ on copper foil. By simply varying the incident angle of the deposition flux, $TiO_2$ films can be made with dense structure, continuous reticulated structure or separated nano-columnar structure. The films deposited at an incidence angle of 80º by reactive ballistic deposition were the most porous and nanostructured and vastly outperformed dense ($0^o$) bulk films in their charge/discharge rates and reversible capacities for films of equal masses of $TiO_2$. Films deposited at $80^o$ also exhibit a high reversible capacity (285 $mAhg^{-1}$ at 0.2 C), an excellent rate capability (near 200 $mAhg^{-1}$ at 5 C), as well as a good cycling stability. The enhanced electrochemical properties of the RBD electrodes are mainly attributed to their highly porous structure and large surface area.

In Chapter 3, hematite nanorods were synthesized by a hydrothermal method, which were then investigated as an anode material for lithium ion batteries. Electrodes made of α-$Fe_2O_3$ nanorods outperformed electrodes fabricated from submicron and micron sized particles in terms of reversible capacity, cyclability, and rate capability toward lithium storage. High initial reversible capacities of 908 mAh $g^{-1}$ at 0.2 C rate and 837 mAh $g^{-1}$ at 0.5 C rate were achieved for α-$Fe_2O_3$ nanorod electrode, and these capacities were fully retained after numerous cycles. The excellent performance of the hematite nanorod electrode can be attributed to the small diameter elongated nanostructure that provides a short diffusion path for lithium-ion diffusion, which also accommodates the strain generated during the lithiation/de-lithiation process.

In Chapter 4 it was demonstrats that the electrochemical performance of $SnO_2$ can be improved by incorporating $TiO_2$ to support the structure. In this chapter, commercial $SnO_2$ nanoparticles and a $TiO_2$-supported $SnO_2$ nanocomposite formed of equimolar amounts of the Sn and Ti oxides were synthesized by the co-precipitation method and then were investigated as anode materials for Li-ion batteries. The electrodes made of the $SnO_2$ nanoparticles show improved cycling stability by limiting the voltage window of the charge/discharge cycles to the range 50 mV - 1.0 V. When cycling within this potential domain, the $SnO_2$ NP electrode can maintain a capacity of ~500 mAh $g^{-1}$ up to 50 cycles at a 0.2 C rate. Although adding $TiO_2$ decreases the overall capacity at low C rates, the $SnO_2$/$TiO_2$ nanocomposite electrodes exhibit better capacity retention and higher Coulombic efficiency. The $Li_xTiO_2$ formed in the $SnO_2$/$TiO_2$ composite during the

first half-cycle structurally/mechanically supports the electrode and is believed to be the reason for prolonged cyclability. Both the $SnO_2$ NP electrodes and the $TiO_2$-supported-$SnO_2$ electrodes show good cycling stability at various C rates up to 5C. The reversible capacities of the $SnO_2$ NP electrode are higher than that of the $SnO_2/TiO_2$ electrode at C rates from 0.2 C to 2 C when taking into account the additional mass of $TiO_2$. However, the $SnO_2/TiO_2$ electrode shows a higher overall capacity when cycled at 5 C, which is attributed to the small particle size and the $Li^+$ conducting $Li_xTiO_2$ formed in the nanocomposite.

In Chapters 5 and 6, electrolytes containing fluoroethylene carbonate (FEC) were used to modify the solid electrolyte interface, i.e. passive film, formed on the surface of the anode materials. The effects of the FEC-based electrolyte on the performance of Si-based and $GeO_2$-based anode were investigated. The capacity retention of these two anodes after cycling was significantly improved compared to electrodes cycled in a traditional ethylene carbonate (EC)-based electrolyte. The improved performance of the Si electrodes/$GeO_2$ electrodes in the FEC-based electrolyte is attributed to the better properties of the FEC-derived solid electrolyte interface on the surface of the active materials.

In Chapter 7 it was shown that $Sn_{0.9}Cu_{0.1}$ nanoparticles can be prepared via a surfactant-assisted wet chemical route at room temperature. The material proved to be of interest as an anode material for Na-ion batteries. Electrodes made with the $Sn_{0.9}Cu_{0.1}$

nanoparticles exhibited a stable capacity greater than 420 mAh $g^{-1}$ at 0.2 C rate, retaining 97% of their capacity after 100 cycles of sodium insertion/de-insertion. The cyclability of the $Sn_{0.9}Cu_{0.1}$ nanoparticle electrode outperformed electrodes fabricated from Sn microparticles and Sn nanoparticles, which only retained 13% and 49% of their capacities after 100 cycles, respectively. The $Sn_{0.9}Cu_{0.1}$ electrode also showed better rate capability when compared to the Sn nanoparticle electrode and Sn microparticle electrode. The incorporation of copper into tin was effective in reducing the interfacial charge transfer resistance and also possibly suppressing the aggregation of tin, and thus resulted in better cyclability and high rate capability.

## ONGOING AND FUTURE RESEARCH

The body of this dissertation focuses on improving the anode materials and the electrolyte of Li-ion and Na-ion batteries. In an electrochemical system, the binder also plays the important role of binding the materials (including the active materials and the conductive additives) onto the current collector and maintaining the integrity of the electrode during charge/discharge cycling. Polyvinylidene fluoride (PVDF) has been successfully used as the binder for both carbonaceous anodes and lithium metal oxide cathodes for Li-ion batteries.[1-6] However, PVDF is not a good choice of binder for those anode materials that undergo significant volume change upon cycling.[7] Alternative binders were investigated to improve the electrochemical performance. Sodium

carboxymethyl cellulose (Na-CMC) has been shown to outperform the conventional PVDF as the binder for Si-based anodes, which suffer from a huge volume change during lithium alloying/de-alloying.[8-12] Na-CMC can also be used to improve the cycling stability of other alloying materials, such as Ge, Sn and Sn,[12] and conversion oxides.[13, 14] Moreover, the water-soluble Na-CMC is relatively of low cost and is environmentally friendly compared to PVDF, which requires the use of volatile organic solvents (e.g. N-methyl pyrrolidone) during the process of slurry casting.[15] For these reasons, Na-CMC has been selected as the binder for assessing the electrochemical performance of anode materials in this dissertation (except for Chapter 2 and Chapter 6). Besides PVDF and Na-CMC, various polymeric binders have been considered as the binder for the preparation of battery electrodes, such as polyacrylic acid (PAA),[16-18] lithium polyacrylate (Li-PAA),[19] sodium alginate,[20-22] and conducting polymers.[23, 24] The electrochemical performance of the anode materials presented in this dissertation could be further improved by introducing new binders. Furthermore, a systematic study on the relationship between the performance of the electrode and the physical properties of the polymer binder would help to design or select more effective binders.

Also, most of the electrochemical properties of the anode materials of this dissertation were measured against either metallic lithium or metallic sodium as the counter electrodes. The Li (or Na) counter electrode provides a sufficient supply of Li (or Na), which also serves as the pseudo-reference electrode, allowing the potential of the working electrode to be determined. However, for practical applications, the anode is

typically paired with a cathode containing lithium cobalt oxide ($LiCoO_2$), lithium iron phosphate (LFP, $LiFePO_4$), lithium manganese oxide (LMO, $LiMn_2O_4$) or lithium nickel manganese cobalt oxide (NMC). Therefore, further tests need to be done to determine the actual performance of the alternative anode materials in full batteries. For example, one could perform cycle tests on cells composed of a LFP-cathode/$Fe_2O_3$-nanorod-anode cell. Furthermore, although the electrolyte containing fluoroethylene carbonate (FEC) has been shown to be helpful in improving the cylcing performance of the anode, rare efforts have been made to study the effect of the FEC on cathode materials. Preliminary results in our lab suggest that the FEC-based electrolyte can work as well as the conventional EC-based electrolyte for $LiFePO_4$ cathodes. The $LiFePO_4$ electrodes were prepared by mixing the $LiFePO_4$ (~2 μm, Hirose Tech)(80 wt %) with conductive carbon black (Super P-Li, Timcal) (10 wt %) and with 90 kDa sodium carboxymethyl cellulose (Aldrich) (10 wt %) with DIW as the dispersing medium. The assembled coin cells were galvanostatically cycled at room temperature in a multichannel battery test system (BT 2043, Arbin) between 2.0 V and 4.3 V. Figure 8.1 shows the voltage profiles of $LiFePO_4$ electrodes tested against $Li/Li^+$ in the EC-based and the FEC-based electrolytes for the first cycle at C/20 rate (8.5 mA $g^{-1}$). There is no significant difference betweeen the $LiFePO_2$ electrode in the EC-based electrolyte and in the FEC-based electrolyte. Reversible capacities of 143 mAh $g^{-1}$ and 141 mAh $g^{-1}$ were observed for the initial cycle cycle of the electrodes in the EC-based electrolyte and in the FEC-based electrolyte, respectively.

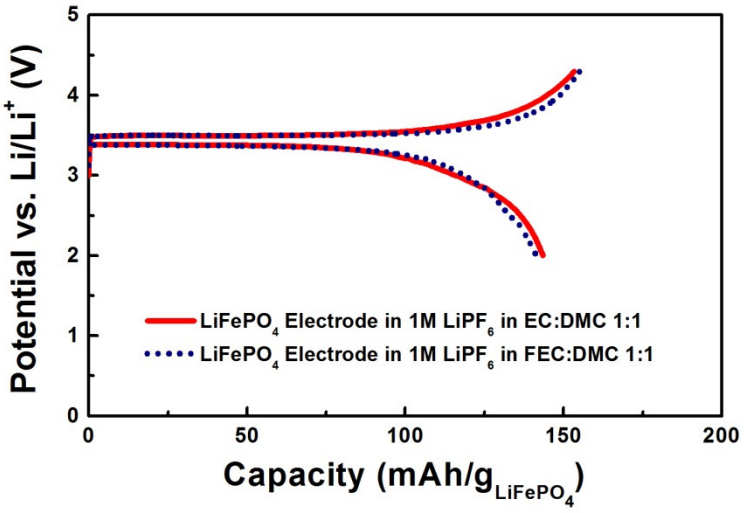


Figure 8.1. Charge/discharge voltage profiles of $LiFePO_4$ electrodes cycled in EC- and FEC-based electrolytes for the first cycle at C/20 rate (8.5 mA $g^{-1}$).

Figure 8.2 shows the reversible capacities of the $LiFePO_4$ electrodes in the EC- and in the FEC-based electrolyte, respectively, at C/20 (8.5 mA $g^{-1}$) for the initial cycle and then switched to 1 C (170 mA $g^{-1}$) for the subsequent cycles. The cycling stability of the $LiFePO_4$ electrodes performed similarly in both electrolytes, retaining a capacity of ~118 mAh $g^{-1}$ in the FEC based electrolyte and a capacity of ~125 mAh $g^{-1}$ in the EC-based electrolyte after 400 cycles at 1 C. Therefore, we believe the FEC-based electrolyte can be utilized in full batteries comprising a $LiFePO_4$ cathode. Further experiments in the form of full batteries are needed to verify this.

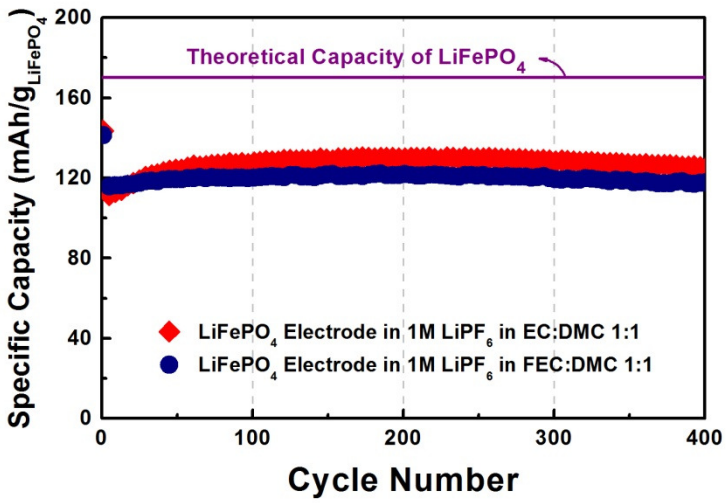


Figure 8.2. Reversible capacities of $LiFePO_4$ electrodes cycled in EC- and FEC-based electrolytes at C/20 rate (8.5 mA $g^{-1}$) for the initial cycle and switched to 1 C (170 mA $g^{-1}$) for the subsequent cycles.

Lastly, although it is beneficial to have FEC in the electrolyte for certain anode materials like silicon, the exact mechanism is still not clear. It would be of interest to *in-situ* characterize the growth and properties of the FEC-derived solid electrolyte interface by electron microscopy, X-ray microscopy, Raman spectroscopy and X-ray photoelectron spectroscopy etc. These further examinations could shed light on how to better design the electrolyte system and the anode materials for the next generation Li-ion and Na-ion batteries.

## REFERENCES


1. Tran, T. D.; Feikert, J. H.; Song, X.; Kinoshita, K., *J. Electrochem. Soc.* **1995,** *142* (10), 3297-3302.

2. Maleki, H.; Deng, G. P.; Kerzhner-Haller, I.; Anani, A.; Howard, J. N., *J. Electrochem. Soc.* **2000,** *147* (12), 4470-4475.

3. Fransson, L.; Eriksson, T.; Edstrom, K.; Gustafsson, T.; Thomas, J. O., *J. Power Sources* **2001,** *101* (1), 1-9.

4. Yoo, M.; Frank, C. W.; Mori, S., *Chem. Mater.* **2003,** *15* (4), 850-861.

5. Markevich, E.; Salitra, G.; Aurbach, D., *Electrochem. Commun.* **2005,** *7* (12), 1298-1304.

6. Choi, N. S.; Lee, Y. G.; Park, J. K., *J. Power Sources* **2002,** *112* (1), 61-66.

7. Chen, L. B.; Xie, X. H.; Xie, J. Y.; Wang, K.; Yang, J., *J. Appl. Electrochem.* **2006,** *36* (10), 1099-1104.

8. Hochgatterer, N. S.; Schweiger, M. R.; Koller, S.; Raimann, P. R.; Wohrle, T.; Wurm, C.; Winter, M., *Electrochemical and Solid State Letters* **2008,** *11* (5), A76-A80.

9. Buqa, H.; Holzapfel, M.; Krumeich, F.; Veit, C.; Novak, P., *J. Power Sources* **2006,** *161* (1), 617-622.

10. Lestrie, B.; Bahri, S.; Sandu, I.; Roue, L.; Guyomard, D., *Electrochem. Commun.* **2007,** *9* (12), 2801-2806.

11. Li, J.; Lewis, R. B.; Dahn, J. R., *Electrochemical and Solid State Letters* **2007,** *10* (2), A17-A20.

12. Bridel, J. S.; Azais, T.; Morcrette, M.; Tarascon, J. M.; Larcher, D., *Chem. Mater.* **2010,** *22* (3), 1229-1241.

13. Li, J.; Dahn, H. M.; Krause, L. J.; Le, D. B.; Dahn, J. R., *J. Electrochem. Soc.* **2008,** *155* (11), A812-A816.

14. Wang, Z. Y.; Madhavi, S.; Lou, X. W., *J. Phys. Chem. C* **2012,** *116* (23), 12508-12513.

15. Lux, S. F.; Schappacher, F.; Balducci, A.; Passerini, S.; Winter, M., *J. Electrochem. Soc.* **2010,** *157* (3), A320-A325.

16. Lee, J. H.; Paik, U.; Hackley, V. A.; Choi, Y. M., *J. Power Sources* **2006,** *161* (1), 612-616.

17. Chong, J.; Xun, S. D.; Zheng, H. H.; Song, X. Y.; Liu, G.; Ridgway, P.; Wang, J. Q.; Battaglia, V. S., *J. Power Sources* **2011,** *196* (18), 7707-7714.

18. Komaba, S.; Shimomura, K.; Yabuuchi, N.; Ozeki, T.; Yui, H.; Konno, K., *J. Phys. Chem. C* **2011,** *115* (27), 13487-13495.

19. Li, J.; Le, D. B.; Ferguson, P. P.; Dahn, J. R., *Electrochim. Acta* **2010,** *55* (8), 2991-2995.

20. Kovalenko, I.; Zdyrko, B.; Magasinski, A.; Hertzberg, B.; Milicev, Z.; Burtovyy, R.; Luzinov, I.; Yushin, G., *Science* **2011,** *334* (6052), 75-79.

21. Chockla, A. M.; Bogart, T. D.; Hessel, C. M.; Klavetter, K. C.; Mullins, C. B.; Korgel, B. A., *J. Phys. Chem. C* **2012,** *116* (34), 18079-18086.

22. Chockla, A. M.; Klavetter, K. C.; Mullins, C. B.; Korgel, B. A., *Chem. Mater.* **2012,** *24* (19), 3738-3745.

23. Liu, G.; Xun, S. D.; Vukmirovic, N.; Song, X. Y.; Olalde-Velasco, P.; Zheng, H. H.; Battaglia, V. S.; Wang, L. W.; Yang, W. L., *Adv. Mater. (Weinheim, Ger.)* **2011,** *23* (40), 4679-+.

24. Xun, S.; Song, X.; Battaglia, V.; Liu, G., *J. Electrochem. Soc.* **2013,** *160* (6), A849-A855.

# Bibliography


Abel, P. R.; Lin, Y.-M.; Celio, H.; Heller, A.; Mullins, C. B., *ACS Nano* **2012,** *6* (3), 2506-2516.

Abelmann, L.; Lodder, C., *Thin Solid Films* **1997,** *305*, 1-21.

Abraham, K. M.; Pasquariello, D. M.; Willstaedt, E. B., *J. Electrochem. Soc.* **1990,** *137* (3), 743-749.

Alcantara, R.; Fernandez-Madrigal, F. J.; Lavela, P.; Tirado, J. L.; Jumas, J. C.; Olivier-Fourcade, J., *J. Mater. Chem.* **1999,** *9* (10), 2517-2521.

Ardizzone, S.; Fregonara, G.; Trasatti, S., *Electrochim. Acta* **1990,** *35* (1), 263-267.

Arico, A. S.; Bruce, P.; Scrosati, B.; Tarascon, J. M.; Van Schalkwijk, W., *Nat. Mater.* **2005,** *4* (5), 366-377.

Armand, M.; Tarascon, J. M., *Nature* **2008,** *451* (7179), 652-657.

Auborn, J. J.; French, K. W.; Lieberma.Si; Shah, V. K.; Heller, A., *J. Electrochem. Soc.* **1973,** *120* (12), 1613-1619.

Aurbach, D., *J. Power Sources* **2005,** *146* (1-2), 71-78.

Aurbach, D.; Markovsky, B.; Shechter, A.; EinEli, Y.; Cohen, H., *J. Electrochem. Soc.* **1996,** *143* (12), 3809-3820.

Balaya, P.; Bhattacharyya, A. J.; Jamnik, J.; Zhukovskii, Y. F.; Kotomin, E. A.; Maier, J., *J. Power Sources* **2006,** *159* (1), 171-178.

Barabási, A.-L.; Stanley, H. E., *Fractal Concepts in Surface Growth*. Cambridge University Press: Cambridge, 1995.

Bard, A. J.; Faulkner, L. R., *Electrochemical Methods: Fundamentals and Applications*. 2nd ed.; Wiley: New York, 2001.

Barton, T. J.; Bull, L. M.; Klemperer, W. G.; Loy, D. A.; McEnaney, B.; Misono, M.; Monson, P. A.; Pez, G.; Scherer, G. W.; Vartuli, J. C.; Yaghi, O. M., *Chem. Mater.* **1999,** *11* (10), 2633-2656.

Beattie, S. D.; Larcher, D.; Morcrette, M.; Simon, B.; Tarascon, J. M., *J. Electrochem. Soc.* **2008,** *155* (2), A158-A163.

Bendavid, A.; Martin, P. J.; Takikawa, H., *Thin Solid Films* **2000,** *360* (1-2), 241-249.

Bervas, M.; Klein, L. C.; Amatucci, G. G., *J. Electrochem. Soc.* **2006,** *153* (1), A159-A170.

Besenhard, J. O.; Winter, M., *ChemPhysChem* **2002,** *3* (2), 155-159.

Besenhard, J. O.; Yang, J.; Winter, M., *J. Power Sources* **1997,** *68* (1), 87-90.

Borghols, W. J. H.; Lutzenkirchen-Hecht, D.; Haake, U.; Chan, W.; Lafont, U.; Kelder, E. M.; van Eck, E. R. H.; Kentgens, A. P. M.; Mulder, F. M.; Wagemaker, M., *J. Electrochem. Soc.* **2010,** *157* (5), A582-A588.

Borghols, W. J. H.; Wagemaker, M.; Lafont, U.; Kelder, E. M.; Mulder, F. M., *Chem. Mater.* **2008,** *20* (9), 2949-2955.

Bose, N.; Basu, M.; Mukherjee, S., *Mater. Res. Bull.* **2012,** *47* (6), 1368-1373.

Bridel, J. S.; Azais, T.; Morcrette, M.; Tarascon, J. M.; Larcher, D., *Chem. Mater.* **2010,** *22* (3), 1229-1241.

Bruce, P. G.; Scrosati, B.; Tarascon, J. M., *Angew. Chem. Int. Edit.* **2008,** *47* (16), 2930-2946.

Buqa, H.; Holzapfel, M.; Krumeich, F.; Veit, C.; Novak, P., *J. Power Sources* **2006,** *161* (1), 617-622.

Cabana, J.; Monconduit, L.; Larcher, D.; Palacin, M. R., *Adv. Mater. (Weinheim, Ger.)* **2010,** *22* (35), E170-E192.

Cantao, M. P.; Cisneros, J. I.; Torresi, R. M., *J. Phys. Chem.* **1994,** *98* (18), 4865-4869.

Chalk, S. G.; Miller, J. E., *J. Power Sources* **2006,** *159*, 73-80.

Chan, C. K.; Patel, R. N.; O'Connell, M. J.; Korgel, B. A.; Cui, Y., *ACS Nano* **2010,** *4* (3), 1443-1450.

Chan, C. K.; Peng, H. L.; Liu, G.; McIlwrath, K.; Zhang, X. F.; Huggins, R. A.; Cui, Y., *Nat. Nanotechnol.* **2008,** *3* (1), 31-35.

Chao, S. C.; Yen, Y. C.; Song, Y. F.; Chen, Y. M.; Wu, H. C.; Wu, N. L., *Electrochem. Commun.* **2010,** *12* (2), 234-237.

Chen, F. L.; Shi, Z.; Liu, M. L., *Chem. Commun. (Cambridge, U. K.)* **2000,** (21), 2095-2096.

Chen, J.; Xu, L. N.; Li, W. Y.; Gou, X. L., *Adv. Mater. (Weinheim, Ger.)* **2005,** *17*, 582-586.

Chen, J. S.; Lou, X. W., *Electrochem. Commun.* **2009,** *11* (12), 2332-2335.

Chen, J. S.; Zhu, T.; Yang, X. H.; Yang, H. G.; Lou, X. W., *J. Am. Chem. Soc.* **2010,** *132* (38), 13162-13164.

Chen, L. B.; Xie, X. H.; Xie, J. Y.; Wang, K.; Yang, J., *J. Appl. Electrochem.* **2006,** *36* (10), 1099-1104.

Cheng, F. Y.; Chen, J., *J. Mater. Res.* **2006,** *21* (11), 2744-2757.

Chevrier, V. L.; Ceder, G., *J. Electrochem. Soc.* **2011,** *158* (9), A1011-A1014.

Chockla, A. M.; Bogart, T. D.; Hessel, C. M.; Klavetter, K. C.; Mullins, C. B.; Korgel, B. A., *J. Phys. Chem. C* **2012,** *116* (34), 18079-18086.

Chockla, A. M.; Klavetter, K. C.; Mullins, C. B.; Korgel, B. A., *ACS Appl. Mater. Interfaces* **2012,** *4* (9), 4658-4664.

Chockla, A. M.; Klavetter, K. C.; Mullins, C. B.; Korgel, B. A., *Chem. Mater.* **2012,** *24* (19), 3738-3745.

Choi, N. S.; Lee, Y. G.; Park, J. K., *J. Power Sources* **2002,** *112* (1), 61-66.

Choi, N. S.; Yew, K. H.; Lee, K. Y.; Sung, M.; Kim, H.; Kim, S. S., *J. Power Sources* **2006,** *161* (2), 1254-1259.

Chong, J.; Xun, S. D.; Zheng, H. H.; Song, X. Y.; Liu, G.; Ridgway, P.; Wang, J. Q.; Battaglia, V. S., *J. Power Sources* **2011,** *196* (18), 7707-7714.

Chun, L.; Wu, X. Z.; Lou, X. M.; Zhang, Y. X., *Electrochim. Acta* **2010,** *55* (9), 3089-3092.

Colgan, M. J.; Djurfors, B.; Ivey, D. G.; Brett, M. J., *Thin Solid Films* **2004,** *466* (1-2), 92-96.

Conway, B. E.; Birss, V.; Wojtowicz, J., *J. Power Sources* **1997,** *66* (1-2), 1-14.

Courtney, I. A.; Dahn, J. R., *J. Electrochem. Soc.* **1997,** *144* (9), 2943-2948.

Darwiche, A.; Marino, C.; Sougrati, M. T.; Fraisse, B.; Stievano, L.; Monconduit, L., *J. Am. Chem. Soc.* **2012,** *134* (51), 20805-20811.

Demir-Cakan, R.; Hu, Y. S.; Antonietti, M.; Maier, J.; Titirici, M. M., *Chem. Mater.* **2008,** *20* (4), 1227-1229.

Dianov, E. A.; Mashinsky, V. A., *J. Lightwave Technol.* **2005,** *23* (11), 3500-3508.

Disma, F.; Aymard, L.; Dupont, L.; Tarascon, J. M., *J. Electrochem. Soc.* **1996,** *143* (12), 3959-3972.

Dohnalek, Z.; Kimmel, G. A.; Ayotte, P.; Smith, R. S.; Kay, B. D., *J. Chem. Phys.* **2003,** *118* (1), 364-372.

Dohnalek, Z.; Kimmel, G. A.; McCready, D. E.; Young, J. S.; Dohnalkova, A.; Smith, R. S.; Kay, B. D., *J. Phys. Chem. B* **2002,** *106* (14), 3526-3529.

Dunn, B.; Kamath, H.; Tarascon, J. M., *Science* **2011,** *334* (6058), 928-935.

Dziewonski, P. M.; Grzeszczuk, M., *J. Power Sources* **2009,** *190* (2), 545-552.

Eggleston, C. M.; Hochella, M. F., *Am. Mineral.* **1992,** *77* (9-10), 911-922.

Ellis, L. D.; Hatchard, T. D.; Obrovac, M. N., *J. Electrochem. Soc.* **2012,** *159* (11), A1801-A1805.

Etacheri, V.; Haik, O.; Goffer, Y.; Roberts, G. A.; Stefan, I. C.; Fasching, R.; Aurbach, D., *Langmuir* **2012,** *28* (1), 965-976.

Exnar, I.; Kavan, L.; Huang, S. Y.; Gratzel, M., *J. Power Sources* **1997,** *68* (2), 720-722.

Fang, H. T.; Liu, M.; Wang, D. W.; Sun, T.; Guan, D. S.; Li, F.; Zhou, J. G.; Sham, T. K.; Cheng, H. M., *Nanotechnology* **2009,** *20* (22), 225701.

Fattakhova, D.; Kavan, L.; Krtil, P., *J. Solid State Electrochem.* **2001,** *5* (3), 196-204.

Feng, J. K.; Lai, M. O.; Lu, L., *Electrochim. Acta* **2012,** *62*, 103-108.

Flaherty, D. W.; Dohnalek, Z.; Dohnalkova, A.; Arey, B. W.; McCready, D. E.; Ponnusamy, N.; Mullins, C. B.; Kay, B. D., *J. Phys. Chem. C* **2007,** *111* (12), 4765-4773.

Flaherty, D. W.; Hahn, N. T.; Ferrer, D.; Engstrom, T. R.; Tanaka, P. L.; Mullins, C. B., *J. Phys. Chem. C* **2009,** *113* (29), 12742-12752.

Flaherty, D. W.; May, R. A.; Berglund, S. P.; Stevenson, K. J.; Mullins, C. B., *Chem. Mater.* **2010,** *22* (2), 319-329.

Fleischauer, M. D.; Li, J.; Brett, M. J., *J. Electrochem. Soc.* **2009,** *156* (1), A33-A36.

Fransson, L.; Eriksson, T.; Edstrom, K.; Gustafsson, T.; Thomas, J. O., *J. Power Sources* **2001,** *101* (1), 1-9.

Fu, Z. W.; Qin, Q. Z., *J. Phys. Chem. B* **2000,** *104* (23), 5505-5510.

Furukawa, H.; Hibino, M.; Honma, I., *J. Electrochem. Soc.* **2004,** *151* (4), A527-A531.

Goodenough, J. B.; Kim, Y., *Chem. Mater.* **2010,** *22* (3), 587-603.

Graetz, J.; Ahn, C. C.; Yazami, R.; Fultz, B., *Electrochemical and Solid State Letters* **2003,** *6* (9), A194-A197.

Graetz, J.; Ahn, C. C.; Yazami, R.; Fultz, B., *J. Electrochem. Soc.* **2004,** *151* (5), A698-A702.

Grugeon, S.; Laruelle, S.; Herrera-Urbina, R.; Dupont, L.; Poizot, P.; Tarascon, J. M., *J. Electrochem. Soc.* **2001,** *148* (4), A285-A292.

Guo, X. Z.; Kang, Y. F.; Wang, L. W.; Liu, X. H.; Zhang, J.; Yang, T. L.; Wu, S. H.; Wang, S. R., *Mater. Sci. Eng., C* **2011,** *31* (7), 1369-1373.

Hahn, N. T.; Mullins, C. B., *Chem. Mater.* **2010,** *22* (23), 6474-6482.

Hahn, N. T.; Ye, H. C.; Flaherty, D. W.; Bard, A. J.; Mullins, C. B., *ACS Nano* **2010,** *4* (4), 1977-1986.

Hariharan, S.; Saravanan, K.; Balaya, P., *Electrochemical and Solid State Letters* **2010,** *13* (9), A132-A134.

Hassoun, J.; Croce, F.; Hong, I.; Scrosati, B., *Electrochem. Commun.* **2011,** *13* (3), 228-231.

Hawkeye, M. M.; Brett, M. J., *Journal of Vacuum Science & Technology A* **2007,** *25* (5), 1317-1335.

Ho, W. H.; Liu, H. C.; Chen, H. C.; Yen, S. K., *Surf. Coat. Technol.* **2007,** *201* (16-17), 7100-7106.

Hochgatterer, N. S.; Schweiger, M. R.; Koller, S.; Raimann, P. R.; Wohrle, T.; Wurm, C.; Winter, M., *Electrochemical and Solid State Letters* **2008,** *11* (5), A76-A80.

Holl, R.; Kling, M.; Schroll, E., *Ore Geology Reviews* **2007,** *30* (3-4), 145-180.

Hu, Y. S.; Kienle, L.; Guo, Y. G.; Maier, J., *Adv. Mater. (Weinheim, Ger.)* **2006,** *18* (11), 1421-1426.

Issac, I.; Scheuermann, M.; Becker, S. M.; Bardaji, E. G.; Adelhelm, C.; Wang, D.; Kubel, C.; Indris, S., *J. Power Sources* **2011,** *196* (22), 9689-9695.

Jarvis, C. R.; Lain, M. J.; Yakovleva, M. V.; Gao, Y., *J. Power Sources* **2006,** *162* (2), 800-802.

Jiang, C. H.; Wei, M. D.; Qi, Z. M.; Kudo, T.; Honma, I.; Zhou, H. S., *J. Power Sources* **2007,** *166* (1), 239-243.

Kasavajjula, U.; Wang, C. S.; Appleby, A. J., *J. Power Sources* **2007,** *163* (2), 1003-1039.

Kay, A.; Cesar, I.; Gratzel, M., *J. Am. Chem. Soc.* **2006,** *128* (49), 15714-15721.

Kim, C.; Noh, M.; Choi, M.; Cho, J.; Park, B., *Chem. Mater.* **2005,** *17* (12), 3297-3301.

Kim, D. W.; Hwang, I. S.; Kwon, S. J.; Kang, H. Y.; Park, K. S.; Choi, Y. J.; Choi, K. J.; Park, J. G., *Nano Lett.* **2007,** *7* (10), 3041-3045.

Kim, H. S.; Piao, Y.; Kang, S. H.; Hyeon, T.; Sung, Y. E., *Electrochem. Commun.* **2010,** *12* (3), 382-385.

Kim, J.; Dohnalek, Z.; Kay, B. D., *Surf. Sci.* **2005,** *586* (1-3), 137-145.

Kim, S. W.; Han, T. H.; Kim, J.; Gwon, H.; Moon, H. S.; Kang, S. W.; Kim, S. O.; Kang, K., *ACS Nano* **2009,** *3* (5), 1085-1090.

Kim, S. W.; Seo, D. H.; Ma, X. H.; Ceder, G.; Kang, K., *Adv. Energy Mater.* **2012,** *2* (7), 710-721.

Kimmel, G. A.; Stevenson, K. P.; Dohnalek, Z.; Smith, R. S.; Kay, B. D., *J. Chem. Phys.* **2001,** *114* (12), 5284-5294.

Kitaura, H.; Takahashi, K.; Mizuno, F.; Hayashi, A.; Tadanaga, K.; Tatsumisago, M., *J. Electrochem. Soc.* **2007,** *154* (7), A725-A729.

Klavetter, K. C.; Wood, S. M.; Lin, Y.-M.; Snider, J. L.; Davy, N. C.; Chockla, A. M.; Romanovicz, D. K.; Korgel, B. A.; Lee, J.-W.; Heller, A.; Mullins, C. B., *J. Power Sources* **2013**.

Komaba, S.; Ishikawa, T.; Yabuuchi, N.; Murata, W.; Ito, A.; Ohsawa, Y., *ACS Appl. Mater. Interfaces* **2011,** *3* (11), 4165-4168.

Komaba, S.; Shimomura, K.; Yabuuchi, N.; Ozeki, T.; Yui, H.; Konno, K., *J. Phys. Chem. C* **2011,** *115* (27), 13487-13495.

Koudriachova, M. V.; Harrison, N. M.; de Leeuw, S. W., *Physical Review B* **2002,** *65* (23), 235423.

Koudriachova, M. V.; Harrison, N. M.; de Leeuw, S. W., *Phys. Rev. Lett.* **2001,** *86* (7), 1275-1278.

Kovalenko, I.; Zdyrko, B.; Magasinski, A.; Hertzberg, B.; Milicev, Z.; Burtovyy, R.; Luzinov, I.; Yushin, G., *Science* **2011,** *334* (6052), 75-79.

Krause, K. M.; Taschuk, M. T.; Harris, K. D.; Rider, D. A.; Wakefield, N. G.; Sit, J. C.; Buriak, J. M.; Thommes, M.; Brett, M. J., *Langmuir* **2010,** *26* (6), 4368-4376.

Kravchyk, K.; Protesescu, L.; Bodnarchuk, M. I.; Krumeich, F.; Yarema, M.; Walter, M.; Guntlin, C.; Kovalenko, M. V., *J. Am. Chem. Soc.* **2013,** *135* (11), 4199-4202.

Kubiak, P.; Pfanzelt, M.; Geserick, J.; Hormann, U.; Husing, N.; Kaiser, U.; Wohlfahrt-Mehrens, M., *J. Power Sources* **2009,** *194* (2), 1099-1104.

Kulova, T. L.; Skundin, A. M.; Roginskaya, Y. E.; Chibirova, F. K., *Russ. J. Electrochem.* **2004,** *40* (4), 432-439.

Larcher, D.; Bonnin, D.; Cortes, R.; Rivals, I.; Personnaz, L.; Tarascon, J. M., *J. Electrochem. Soc.* **2003,** *150* (12), A1643-A1650.

Larcher, D.; Masquelier, C.; Bonnin, D.; Chabre, Y.; Masson, V.; Leriche, J. B.; Tarascon, J. M., *J. Electrochem. Soc.* **2003,** *150* (1), A133-A139.

Lee, J. H.; Paik, U.; Hackley, V. A.; Choi, Y. M., *J. Power Sources* **2006,** *161* (1), 612-616.

Lestrie, B.; Bahri, S.; Sandu, I.; Roue, L.; Guyomard, D., *Electrochem. Commun.* **2007,** *9* (12), 2801-2806.

Li, C.; Wei, W.; Fang, S. M.; Wang, H. X.; Zhang, Y.; Gui, Y. H.; Chen, R. F., *J. Power Sources* **2010,** *195* (9), 2939-2944.

Li, H.; Balaya, P.; Maier, J., *J. Electrochem. Soc.* **2004,** *151* (11), A1878-A1885.

Li, H.; Huang, X. J.; Chen, L. Q.; Wu, Z. G.; Liang, Y., *Electrochemical and Solid State Letters* **1999,** *2* (11), 547-549.

Li, H.; Shi, L. H.; Lu, W.; Huang, X. J.; Chen, L. Q., *J. Electrochem. Soc.* **2001,** *148* (8), A915-A922.

Li, H.; Zhang, W.; Pan, W., *J. Am. Ceram. Soc.* **2011,** *94* (10), 3184-3187.

Li, J.; Dahn, H. M.; Krause, L. J.; Le, D. B.; Dahn, J. R., *J. Electrochem. Soc.* **2008,** *155* (11), A812-A816.

Li, J.; Le, D. B.; Ferguson, P. P.; Dahn, J. R., *Electrochim. Acta* **2010,** *55* (8), 2991-2995.

Li, J.; Lewis, R. B.; Dahn, J. R., *Electrochemical and Solid State Letters* **2007,** *10* (2), A17-A20.

Li, N. C.; Martin, C. R.; Scrosati, B., *Electrochem. Solid-State Lett.* **2000,** *3* (7), 316-318.

Li, Z. M.; Lai, X. Y.; Wang, H.; Mao, D.; Xing, C. J.; Wang, D., *Nanotechnology* **2009,** *20* (24), 245603.

Lin, Y. M.; Abel, P. R.; Flaherty, D. W.; Wu, J.; Stevenson, K. J.; Heller, A.; Mullins, C. B., *J. Phys. Chem. C* **2011,** *115* (5), 2585-2591.

Lin, Y. M.; Abel, P. R.; Heller, A.; Mullins, C. B., *J. Phys. Chem. Lett.* **2011,** *2* (22), 2885-2891.

Lin, Y. M.; Klavetter, K. C.; Abel, P. R.; Davy, N. C.; Snider, J. L.; Heller, A.; Mullins, C. B., *Chem. Commun. (Cambridge, U. K.)* **2012,** *48* (58), 7268-7270.

Lin, Y. M.; Klavetter, K. C.; Heller, A.; Mullins, C. B., *J. Phys. Chem. Lett.* **2013,** *4* (6), 999-1004.

Lin, Y. M.; Nagarale, R. K.; Klavetter, K. C.; Heller, A.; Mullins, C. B., *J. Mater. Chem.* **2012,** *22* (22), 11134-11139.

Lindsay, M. J.; Blackford, M. G.; Attard, D. J.; Luca, V.; Skyllas-Kazacos, M.; Griffith, C. S., *Electrochim. Acta* **2007,** *52* (23), 6401-6411.

Lindstrom, H.; Sodergren, S.; Solbrand, A.; Rensmo, H.; Hjelm, J.; Hagfeldt, A.; Lindquist, S. E., *J. Phys. Chem. B* **1997,** *101* (39), 7717-7722.

Liu, F.; Umlor, M. T.; Shen, L.; Weston, J.; Eads, W.; Barnard, J. A.; Mankey, G. J., *J. Appl. Phys.* **1999,** *85* (8), 5486-5488.

Liu, G.; Xun, S. D.; Vukmirovic, N.; Song, X. Y.; Olalde-Velasco, P.; Zheng, H. H.; Battaglia, V. S.; Wang, L. W.; Yang, W. L., *Adv. Mater. (Weinheim, Ger.)* **2011,** *23* (40), 4679-+.

Liu, H.; Wang, G. X.; Park, J.; Wang, J.; Zhang, C., *Electrochim. Acta* **2009,** *54* (6), 1733-1736.

Liu, J.; Li, W.; Manthiram, A., *Chem. Commun. (Cambridge, U. K.)* **2010,** *46* (9), 1437-1439.

Liu, J. P.; Li, Y. Y.; Fan, H. J.; Zhu, Z. H.; Jiang, J.; Ding, R. M.; Hu, Y. Y.; Huang, X. T., *Chem. Mater.* **2010,** *22* (1), 212-217.

Liu, J. P.; Li, Y. Y.; Huang, X. T.; Ding, R. M.; Hu, Y. Y.; Jiang, J.; Liao, L., *J. Mater. Chem.* **2009,** *19* (13), 1859-1864.

Liu, N. A.; Hu, L. B.; McDowell, M. T.; Jackson, A.; Cui, Y., *ACS Nano* **2011,** *5* (8), 6487-6493.

Liu, W. R.; Wu, N. L.; Shieh, D. T.; Wu, H. C.; Yang, M. H.; Korepp, C.; Besenhard, J. O.; Winter, M., *J. Electrochem. Soc.* **2007,** *154* (2), A97-A102.

Liu, Z. L.; Hong, L.; Guo, B., *J. Power Sources* **2005,** *143* (1-2), 231-235.

Lou, X. W.; Li, C. M.; Archer, L. A., *Adv. Mater. (Weinheim, Ger.)* **2009,** *21* (24), 2536-+.

Lu, L.; Sui, M. L.; Lu, K., *Science* **2000,** *287* (5457), 1463-1466.

Lu, X. C.; Xia, G. G.; Lemmon, J. P.; Yang, Z. G., *J. Power Sources* **2010,** *195* (9), 2431-2442.

Lu, Y. H.; Wang, L.; Cheng, J. G.; Goodenough, J. B., *Chem. Commun. (Cambridge, U. K.)* **2012,** *48* (52), 6544-6546.

Lux, S. F.; Schappacher, F.; Balducci, A.; Passerini, S.; Winter, M., *J. Electrochem. Soc.* **2010,** *157* (3), A320-A325.

Lytle, J. C.; Rhodes, C. P.; Long, J. W.; Pettigrew, K. A.; Stroud, R. M.; Rolison, D. R., *J. Mater. Chem.* **2007,** *17* (13), 1292-1299.

Ma, J. M.; Lian, J. B.; Duan, X. C.; Liu, X. D.; Zheng, W. J., *J. Phys. Chem. C* **2010,** *114* (24), 10671-10676.

Maier, J., *Nat. Mater.* **2005,** *4* (11), 805-815.

Maleki, H.; Deng, G. P.; Kerzhner-Haller, I.; Anani, A.; Howard, J. N., *J. Electrochem. Soc.* **2000,** *147* (12), 4470-4475.

Manthiram, A., *J. Phys. Chem. Lett.* **2011,** *2* (3), 176-184.

Markevich, E.; Salitra, G.; Aurbach, D., *Electrochem. Commun.* **2005,** *7* (12), 1298-1304.

Matsumura, T.; Sonoyama, N.; Kanno, R.; Takano, M., *Solid State Ionics* **2003,** *158* (3-4), 253-260.

May, R. A.; Flaherty, D. W.; Mullins, C. B.; Stevenson, K. J., *The Journal of Physical Chemistry Letters* **2010,** *1* (8), 1264-1268.

McArthur, M. A.; Trussler, S.; Dahn, J. R., *J. Electrochem. Soc.* **2012,** *159* (3), A198-A207.

McDowell, M. T.; Lee, S. W.; Harris, J. T.; Korgel, B. A.; Wang, C.; Nix, W. D.; Cui, Y., *Nano Lett.* **2013,** *13* (2), 758-764.

McFadden, S. X.; Mishra, R. S.; Valiev, R. Z.; Zhilyaev, A. P.; Mukherjee, A. K., *Nature* **1999,** *398* (6729), 684-686.

McMillan, R.; Slegr, H.; Shu, Z. X.; Wang, W. D., *J. Power Sources* **1999,** *81*, 20-26.

Messier, R.; Venugopal, V. C.; Sunal, P. D., *Journal of Vacuum Science & Technology A* **2000,** *18* (4), 1538-1545.

Mizushima, K.; Jones, P. C.; Wiseman, P. J.; Goodenough, J. B., *Mater. Res. Bull.* **1980,** *15* (6), 783-789.

Mohamedi, M.; Lee, S. J.; Takahashi, D.; Nishizawa, M.; Itoh, T.; Uchida, I., *Electrochim. Acta* **2001,** *46* (8), 1161-1168.

Motohiro, T.; Taga, Y., *Appl. Opt.* **1989,** *28* (13), 2466-2482.

Naidu, H. P.; Virkar, A. V., *J. Am. Ceram. Soc.* **1998,** *81* (8), 2176-2180.

Nakai, H.; Kubota, T.; Kita, A.; Kawashima, A., *J. Electrochem. Soc.* **2011,** *158* (7), A798-A801.

Ning, G.; Haran, B.; Popov, B. N., *J. Power Sources* **2003,** *117* (1-2), 160-169.

Nishijima, M.; Kagohashi, T.; Imanishi, M.; Takeda, Y.; Yamamoto, O.; Kondo, S., *Solid State Ionics* **1996,** *83* (1-2), 107-111.

Nishijima, M.; Kagohashi, T.; Takeda, Y.; Imanishi, M.; Yamamoto, O., *J. Power Sources* **1997,** *68* (2), 510-514.

Nuli, Y. N.; Zhang, P.; Guo, Z. P.; Liu, H. K., *J. Electrochem. Soc.* **2008,** *155* (3), A196-A200.

Obrovac, M. N.; Christensen, L., *Electrochemical and Solid State Letters* **2004,** *7* (5), A93-A96.

Obrovac, M. N.; Krause, L. J., *J. Electrochem. Soc.* **2007,** *154* (2), A103-A108.

Ortiz, G. F.; Hanzu, I.; Djenizian, T.; Lavela, P.; Tirado, J. L.; Knauth, P., *Chem. Mater.* **2009,** *21* (1), 63-67.

Padhi, A. K.; Nanjundaswamy, K. S.; Goodenough, J. B., *J. Electrochem. Soc.* **1997,** *144* (4), 1188-1194.

Palomares, V.; Serras, P.; Villaluenga, I.; Hueso, K. B.; Carretero-Gonzalez, J.; Rojo, T., *Energy & Environmental Science* **2012,** *5* (3), 5884-5901.

Parida, K. M.; Kanungo, S. B.; Sant, B. R., *Electrochim. Acta* **1981,** *26* (3), 435-443.

Pavelko, R. G.; Vasil'ev, A. A.; Sevast'yanov, V. G.; Gispert-Guirado, F.; Vilanova, X.; Kuznetsov, N. T., *Russ. J. Electrochem.* **2009,** *45* (4), 470-475.

Pena, J. S.; Sandu, I.; Joubert, O.; Pascual, F. S.; Arean, C. O.; Brousse, T., *Electrochemical and Solid State Letters* **2004,** *7* (9), A278-A281.

Pereira, N.; Klein, L. C.; Amatucci, G. G., *J. Electrochem. Soc.* **2002,** *149* (3), A262-A271.

Poizot, P.; Laruelle, S.; Grugeon, S.; Dupont, L.; Tarascon, J. M., *Nature* **2000,** *407* (6803), 496-499.

Profatilova, I. A.; Stock, C.; Schmitz, A.; Passerini, S.; Winter, M., *J. Power Sources* **2013,** *222*, 140-149.

Prosini, P. P.; Mancini, R.; Petrucci, L.; Contini, V.; Villano, P., *Solid State Ionics* **2001,** *144* (1-2), 185-192.

Qian, J.; Wu, X.; Cao, Y.; Ai, X.; Yang, H., *Angew. Chem.* **2013,** *125* (17), 4731-4734.

Qian, J. F.; Chen, Y.; Wu, L.; Cao, Y. L.; Ai, X. P.; Yang, H. X., *Chem. Commun. (Cambridge, U. K.)* **2012,** *48* (56), 7070-7072.

Reddy, M. V.; Yu, T.; Sow, C. H.; Shen, Z. X.; Lim, C. T.; Rao, G. V. S.; Chowdari, B. V. R., *Adv. Funct. Mater.* **2007,** *17*, 2792-2799.

Robbie, K.; Brett, M. J.; Lakhtakia, A., *Nature* **1996,** *384* (6610), 616-616.

Robbie, K.; Friedrich, L. J.; Dew, S. K.; Smy, T.; Brett, M. J., *Journal of Vacuum Science & Technology a-Vacuum Surfaces and Films* **1995,** *13* (3), 1032-1035.

Robbie, K.; Sit, J. C.; Brett, M. J., *J. Vac. Sci. Technol., B* **1998,** *16* (3), 1115-1122.

Roginskaya, Y. E.; Chibirova, F. K.; Kulova, T. L.; Skundin, A. M., *Russ. J. Electrochem.* **2006,** *42* (4), 355-362.

Ruffo, R.; Hong, S. S.; Chan, C. K.; Huggins, R. A.; Cui, Y., *J. Phys. Chem. C* **2009,** *113* (26), 11390-11398.

Sakaguchi, S.; Todoroki, S., *Appl. Opt.* **1997,** *36* (27), 6809-6814.

Sayle, T. X. T.; Ngoepe, P. E.; Sayle, D. C., *ACS Nano* **2009,** *3* (10), 3308-3314.

Scrosati, B., *J. Electrochem. Soc.* **1992,** *139* (10), 2776-2781.

Scrosati, B.; Garche, J., *J. Power Sources* **2010,** *195* (9), 2419-2430.

Seto, M. W.; Robbie, K.; Vick, D.; Brett, M. J.; Kuhn, L., *Journal of Vacuum Science & Technology B* **1999,** *17* (5), 2172-2177.

Seyfried, W. E.; Janecky, D. R.; Mottl, M. J., *Geochim. Cosmochim. Acta* **1984,** *48* (3), 557-569.

Sides, C. R.; Li, N. C.; Patrissi, C. J.; Scrosati, B.; Martin, C. R., *Mrs Bulletin* **2002,** *27* (8), 604-607.

Sit, J. C.; Vick, D.; Robbie, K.; Brett, M. J., *J. Mater. Res.* **1999,** *14* (4), 1197-1199.

Slater, M. D.; Kim, D.; Lee, E.; Johnson, C. S., *Adv. Funct. Mater.* **2013,** *23* (8), 947-958.

Song, Y. Q.; Qin, S. S.; Zhang, Y. W.; Gao, W. Q.; Liu, J. P., *J. Phys. Chem. C* **2010,** *114* (49), 21158-21164.

Stevens, D. A.; Dahn, J. R., *J. Electrochem. Soc.* **2001,** *148* (8), A803-A811.

Stevenson, K. P.; Kimmel, G. A.; Dohnalek, Z.; Smith, R. S.; Kay, B. D., *Science* **1999,** *283* (5407), 1505-1507.

Sudworth, J. L., *J. Power Sources* **2001,** *100* (1-2), 149-163.

Takeda, Y.; Nishijima, M.; Yamahata, M.; Takeda, K.; Imanishi, N.; Yamamoto, O., *Solid State Ionics* **2000,** *130* (1-2), 61-69.

Tarascon, J. M.; Armand, M., *Nature* **2001,** *414* (6861), 359-367.

Tartaj, P.; Amarilla, J. M., *J. Power Sources* **2011,** *196* (4), 2164-2170.

Teng, F. Z.; McDonough, W. F.; Rudnick, R. L.; Dalpe, C.; Tomascak, P. B.; Chappell, B. W.; Gao, S., *Geochim. Cosmochim. Acta* **2004,** *68* (20), 4167-4178.

Tirado, J. L., *Materials Science & Engineering R-Reports* **2003,** *40* (3), 103-136.

Tran, T. D.; Feikert, J. H.; Song, X.; Kinoshita, K., *J. Electrochem. Soc.* **1995,** *142* (10), 3297-3302.

Uchiyama, H.; Imai, H., *Chem. Commun. (Cambridge, U. K.)* **2005,** (48), 6014-6016.

van Schalkwijk, W.; Scrosati, B., *Advances in Lithium-Ion Batteries*. Springer: 2002.

Vassiliev, S. Y.; Yusipovich, A. I.; Rogynskaya, Y. E.; Chibirova, F. K.; Skundin, A. M.; Kulova, T. L., *J. Solid State Electrochem.* **2005,** *9* (10), 698-705.

Wachtler, M.; Besenhard, J. O.; Winter, M., *J. Power Sources* **2001,** *94* (2), 189-193.

Wagemaker, M.; Borghols, W. J. H.; Mulder, F. M., *J. Am. Chem. Soc.* **2007,** *129* (14), 4323-4327.

Wagemaker, M.; Kentgens, A. P. M.; Mulder, F. M., *Nature* **2002,** *418* (6896), 397-399.

Wagemaker, M.; van de Krol, R.; Kentgens, A. P. M.; van Well, A. A.; Mulder, F. M., *J. Am. Chem. Soc.* **2001,** *123* (46), 11454-11461.

Wagemaker, M.; Van Der Ven, A.; Morgan, D.; Ceder, G.; Mulder, F. M.; Kearley, G. J., *Chem. Phys.* **2005,** *317* (2-3), 130-136.

Wang, J.; Polleux, J.; Lim, J.; Dunn, B., *J. Phys. Chem. C* **2007,** *111*, 14925-14931.

Wang, L.; Lu, Y. H.; Liu, J.; Xu, M. W.; Cheng, J. G.; Zhang, D. W.; Goodenough, J. B., *Angew. Chem. Int. Edit.* **2013,** *52* (7), 1964-1967.

Wang, X. L.; Han, W. Q.; Chen, H. Y.; Bai, J. M.; Tyson, T. A.; Yu, X. Q.; Wang, X. J.; Yang, X. Q., *J. Am. Chem. Soc.* **2011,** *133* (51), 20692-20695.

Wang, Y.; Cao, G. Z., *Adv. Mater. (Weinheim, Ger.)* **2008,** *20* (12), 2251-2269.

Wang, Y.; Lee, J. Y.; Zeng, H. C., *Chem. Mater.* **2005,** *17* (15), 3899-3903.

Wang, Y. Y.; Hao, Y. J.; Lai, Q. Y.; Lu, J. Z.; Chen, Y. D.; Ji, X. Y., *Ionics* **2008,** *14* (1), 85-88.

Wang, Z. Y.; Madhavi, S.; Lou, X. W., *J. Phys. Chem. C* **2012,** *116* (23), 12508-12513.

Whittingham, M. S., *Science* **1976,** *192* (4244), 1126-1127.

Whittingham, M. S.; Dines, M. B., *J. Electrochem. Soc.* **1977,** *124* (9), 1387-1388.

Winter, M.; Besenhard, J. O., *Electrochim. Acta* **1999,** *45* (1-2), 31-50.

Wu, C. Z.; Yin, P.; Zhu, X.; OuYang, C. Z.; Xie, Y., *J. Phys. Chem. B* **2006,** *110* (36), 17806-17812.

Wu, M. S.; Ou, Y. H.; Lin, P., *J. Electrochem. Soc.* **2011,** *158* (3), A231-A236.

Wu, M. S.; Wang, M. J.; Jow, J. J.; Yang, W. D.; Hsieh, C. Y.; Tsai, H. M., *J. Power Sources* **2008,** *185* (2), 1420-1424.

Wu, X. L.; Guo, Y. G.; Wan, L. J.; Hu, C. W., *J. Phys. Chem. C* **2008,** *112* (43), 16824-16829.

Xiao, L. F.; Cao, Y. L.; Xiao, J.; Wang, W.; Kovarik, L.; Nie, Z. M.; Liu, J., *Chem. Commun. (Cambridge, U. K.)* **2012,** *48* (27), 3321-3323.

Xu, Y. H.; Zhu, Y. J.; Liu, Y. H.; Wang, C. S., *Adv. Energy Mater.* **2013,** *3* (1), 128-133.

Xun, S.; Song, X.; Battaglia, V.; Liu, G., *J. Electrochem. Soc.* **2013,** *160* (6), A849-A855.

Yamada, Y.; Iriyama, Y.; Abe, T.; Ogumi, Z., *J. Electrochem. Soc.* **2010,** *157* (1), A26-A30.

Yamamoto, T.; Nohira, T.; Hagiwara, R.; Fukunaga, A.; Sakai, S.; Nitta, K.; Inazawa, S., *J. Power Sources* **2012,** *217*, 479-484.

Yang, J.; Winter, M.; Besenhard, J. O., *Solid State Ionics* **1996,** *90* (1-4), 281-287.

Yildirim, H.; Greeley, J.; Sankaranarayanan, S., *J. Phys. Chem. C* **2011,** *115* (31), 15661-15673.

Yim, C. H.; Baranova, E. A.; Courtel, F. M.; Abu-Lebdeh, Y.; Davidson, I. J., *J. Power Sources* **2011,** *196* (22), 9731-9736.

Ying, Z.; Wan, Q.; Cao, H.; Song, Z. T.; Feng, S. L., *Appl. Phys. Lett.* **2005,** *87* (11), 113108.

Yoo, M.; Frank, C. W.; Mori, S., *Chem. Mater.* **2003,** *15* (4), 850-861.

Yu, J. G.; Yu, H. G.; Cheng, B.; Zhao, X. J.; Yu, J. C.; Ho, W. K., *J. Phys. Chem. B* **2003,** *107* (50), 13871-13879.

Yu, P.; Ritter, J. A.; White, R. E.; Popov, B. N., *J. Electrochem. Soc.* **2000,** *147* (6), 2081-2085.

Yuan, L.; Guo, Z. P.; Konstantinov, K.; Liu, H. K.; Dou, S. X., *J. Power Sources* **2006,** *159* (1), 345-348.

Zaghib, K.; Brochu, F.; Guerfi, A.; Kinoshita, K., *J. Power Sources* **2001,** *103* (1), 140-146.

Zeng, S. Y.; Tang, K. B.; Li, T. W.; Liang, Z. H.; Wang, D.; Wang, Y. K.; Qi, Y. X.; Zhou, W. W., *J. Phys. Chem. C* **2008,** *112* (13), 4836-4843.

Zhang, J.; Chen, L. B.; Li, C. C.; Wang, T. H., *Appl. Phys. Lett.* **2008,** *93* (26), 264102.

Zhang, W. J., *J. Power Sources* **2011,** *196* (1), 13-24.

Zhao, Y.; Li, J.; Ding, Y.; Guan, L., *RSC Advances* **2011,** *1* (5), 852-856.

Zhou, W.; Lin, L. J.; Wang, W. J.; Zhang, L. L.; Wu, Q. O.; Li, J. H.; Guo, L., *J. Phys. Chem. C* **2011,** *115* (14), 7126-7133.

Zhu, J. J.; Lu, Z. H.; Aruna, S. T.; Aurbach, D.; Gedanken, A., *Chem. Mater.* **2000,** *12* (9), 2557-2566.

Zou, L.; Kang, F. Y.; Li, X. H.; Zheng, Y. P.; Shen, W. C.; Zhang, J., *J. Phys. Chem. Solids* **2008,** *69*, 1265-1271.

# Vita

Yong-Mao Lin was born in Taichung City, Taiwan on July 21, 1980, the son of Rih-Ching Lin and Jin-Duan Chen. After graduating from Taichung Second Senior High School in Taichung, Taiwan in 1998, he enrolled at the National Taiwan University (NTU) in Chemical Engineering. While attending NTU, Yong-Mao conducted both undergraduate and graduate research under the guidance of Prof. Nae-Lih Wu studying the cathode materials for Li-ion batteries. Yong-Mao earned his Bachelor of Science and Master of Science degrees in Chemical Engineering from NTU. He worked a total of four years at AU Optronics Corp. as a process engineer and as a process development engineer in 2004-2008. On June 22 2008, he was married to Ying-Chieh Weng in Taicung, Taiwan, who subsequently gave birth to their daughter, Alicia Elim Lin at Austin, Texas on Nov 12 2010.

In August of 2008, Yong-Mao entered the Cockrell School of Engineering at the University of Texas at Austin. He was awarded the William C. Powers Graduate Fellowship by the University of Texas at Austin Graduate School for the 2012-2013 academic year. Yong-Mao is completing his Ph.D. in Chemical Engineering under the guidance of Prof. C. Buddie Mullins and Prof. Adam Heller.

Email address: yongmaolin@gmail.com

This dissertation was typed by the author.